Bubble Migration in Pore Networks of Uniform Geometry

by

Saloumeh Ghasemian

A thesis
presented to the University of Waterloo
in fulfillment of the
thesis requirement for the degree of
Master of Applied Science
in
Chemical Engineering

Waterloo, Ontario, Canada, 2012

Author’s Declaration

I hereby declare that I am the sole author of this thesis. This is a true copy of the thesis, including any required final revisions, as accepted by my examiners.

I understand that my thesis may be made electronically available to the public.

Abstract

The behavior of bubbles migrating in porous media is a critical factor in several soil remediation operations such as in situ air sparging, supersaturated water injection, bioslurping, trench aeration and up-flow operation of moving bed sand filters as well as in the oil and gas industry. Groundwater aquifers are constantly polluted by human activity and a common threat to fresh water is the contamination by non-aqueous phase liquids (NAPL). In many NAPL removal technologies, gas bubbles carrying NAPL residuals move upwards through the water-saturated porous media and thus play an essential role in contaminant recovery. The mobilization of the residual oil blobs in oil reservoirs is another important application for rising bubbles in porous media. After an oil field is waterflooded, a significant fraction of oil, referred to as waterflood residual oil, remains trapped. A potential mechanism to recover this residual oil is the mobilization of oil by gas bubbles moving upwards in water-wet systems.

The main focus of this work was to measure the velocity of bubbles of various lengths during their migration through a water-wet porous medium. Experiments were conducted in a saturated glass micromodel with different test liquids, air bubbles of varying lengths and different micromodel elevation angles. More than a hundred experimental runs were performed to measure the migration velocity of bubbles as a function of wetting fluid properties, bubble length, and micromodel inclination angle. The results showed a linear dependency of the average bubble velocity as a function of bubble length and the sine of inclination angle of the model. Comparisons were made using experimental data for air bubbles rising in kerosene, Soltrol 170 and dyed White Oil. The calculated permeability of the micromodel was obtained for different systems assuming the effective length for viscous dissipation is equal to the initial bubble length. It was found that the calculated permeability had an increasing trend with increasing bubble length.

Laboratory visualization experiments were conducted for air bubbles in White Oil (viscosity of 12 cP) to visualize the periodic nature of the flow of rising bubbles in a pore network. The motion of the air bubbles in saturated micromodel was video-recorded by a digital camera, reviewed and analyzed using PowerDVD ™11 software. An image of a bubble migrating in the porous medium was obtained by capturing a still frame at a specific time and was analyzed to determine the bubble shape, the exact positions of the bubble front and bubble tail during motion and, thus, the dynamic length of the bubble. A deformation in the shape of the bubble tail end was observed for long bubbles. The dynamic bubble lengths were larger than the static bubble lengths and showed an increasing trend when increasing the angle of inclination. The dynamic bubble lengths were used to recalculate the bubble velocity and

permeability. A linear correlation was found for the average bubble velocity as a function of dynamic bubble length.

Numerical simulation was performed by modifying an existing MATLAB® simulation for the rise velocity of a gas bubble and the induced pressure field while it migrates though porous media. The results showed that the rise velocity of a gas bubble is affected by the grid size of the pore network in the direction perpendicular to the bubble migration. In reality, this effect is demonstrated by the presence of other bubbles near the rising bubble in porous media. The simulation results showed good agreement with experimental data for long bubbles with high velocities. More work is required to improve the accuracy of simulation results for relatively large bubbles.

Acknowledgements

First, I wish to express my sincerest gratitude to my supervisor, Dr. John Chatzis, who has unquestionably had the most impact on me during my Master's study. No words can express my thanks to him for the great favor he did to me by accepting my supervision and for that, I will always be grateful. I thank him for his extensive support, his constant encouragement, his guidance, and his valuable advices.

I would like to acknowledge the technical staff of the Chemical Engineering Department: Ralph Dickhout and Ravindra Singh for their technical assistance. Thanks also to Fred Bakker at University Engineering Machine Shop for his help in preparing my experimental set-up.

I wish to thank my friends and my colleagues in the Porous Media Research group: Rafat Parsaei, Nima Rezaei, and Omidreza Mohammadzadeh for their help and support.

I extend a great deal of gratitude to my family. To my parents, Hossein and Zahra, for who have endured waiting for my return all this time. To my brother, Hesam, my sister-in-law, Sara, and my niece, Parmis, for their support and encouragement.

Last but certainly not least, a special thanks to my husband, Amir Ahmadzadegan, for always being there for me. Without a doubt, his endless support and help made the completion of this work possible for me.

Dedication

This thesis is dedicated to my beloved grandmother, Mirzadeh Mousavi Aghdam, whom I love more than anything in my life.

Table of Contents

List of Figures

List of Tables

Nomenclature

A	-	Cross-sectional Area [L^2]
Ca	-	Capillary Number [-]
C_0	-	Distribution Slip Parameter [-]
C_s	-	Spreading Coefficient [M/t^2]
D_h	-	Hydraulic Diameter [L]
D_P	-	Depth of Pore [L]
D_T	-	Depth of Throat [L]
W_P	-	Pore Width [L]
W_T	-	Throat Width [L]
D	-	Tube Diameter [L], Darcy [L^2]
d_p	-	Mean Particle Diameter [L]
Eo	-	Eötvös Number ($\rho g D^2/\sigma$) [-]
F	-	Formation Resistivity Factor [-]
F_b	-	Buoyancy Force [ML/t^2]
F_d	-	Drag Force [ML/t^2]
F_{st}	-	Surface Tension Force [ML/t^2]
Fr	-	Froude Number $(U/(gD)^{1/2})$ [-]
g	-	Gravity Acceleration [L/t^2]
$h_{c,dr}$	-	Drainage Capillary Height [L]
$h_{c,imb}$	-	Imbibition Capillary Height [L]
H_i	-	Henry's Constant for Substance *i* [M/Lt^2]
K	-	Permeability [L^2]
K_{cal}	-	Calculated Permeability [L^2]

L	-	Length of the Sample [L]
L_b	-	Dynamic Bubble Length [L]
L_{bo}	-	Static Bubble Length before Bubble Starts to Move [L]
L_{eff}	-	Effective Length [L]
L_t	-	Tube Length [L]
N_p	-	Nondimensional Liquid Property Number
P_b	-	Buoyancy Pressure [M/Lt^2]
P_c	-	Capillary Pressure [M/Lt^2]
$P_{c,dr}$	-	Drainage Capillary Pressure [M/Lt^2]
$P_{c,imb}$	-	Imbibition Capillary Pressure [M/Lt^2]
P_i	-	Partial Pressure of Component *i* [M/Lt^2]
P_n	-	Pressure in the Non-wetting Phase [M/Lt^2]
P_w	-	Pressure in the Wetting Phase [M/Lt^2]
P_{wet}	-	Wetted Perimeter of the Tube [L]
Q	-	Volumetric Flow Rate [L^3/t]
R_b	-	Bubble Radius [L]
R_o	-	Resistivity of a Porous Sample Saturated with an Electrolyte [ohm-L]
R_w	-	Resistivity of Electrolyte [ohm-L]
R'	-	Equivalent Pore Throat Radius [L]
R^*	-	Critical Nucleation Radius [L]
Re	-	Reynolds Number ($\rho UD/\mu$) [-]
r	-	Tube Radius [L]
r_{eff}	-	Effective Tube Radius [L]
S	-	Saturation [-]
S_{nwr}	-	Non-wetting Phase Residual Saturation [-]

u	-	Velocity [L/t]
u_b	-	Bubble Velocity [L/t]
u_l	-	Liquid Viscosity [L/t]
u_0	-	Bubble Rise Velocity in Stagnant Fluid [L/t]
u_0*	-	Dimensionless Bubble Propagation Rate $(u_0/gD)^{1/2}$ [-]
V	-	Velocity [L/t]
V_o	-	Volume of Oil [L^3]
V_p	-	Pore Volume [L^3]
V_b	-	Bulk Volume [L^3]
V_g	-	Volume of Gas [L^3]
V_i	-	Volume of Fluid *i* [L^3]
V_w	-	Volume of Water [L^3]
W_P	-	Pore Width [L]
W_T	-	Throat Width [L]
x_i	-	Mole Fraction of Component *i* in the Liquid Phase [-]
X_F	-	Bubble Front Position [L]
X_T	-	Bubble Tail Position [L]
z	-	Hydrostatic Height [L]
Z	-	Coordination Number [-]

Greek Symbols

α	-	Supersaturation Ratio [-]
α_{dip}	-	Dip/Inclination Angle [degrees]

δ	-	Wetting Film Thickness [L]
ΔP	-	Pressure Drop [M/LT^2]
Δg_v	-	Bulk Free Energy per Unit of Liquid Volume [M/LT^2]
ε	-	Dimensionless Laminar Film Thickness [-]
θ	-	Contact Angle [degrees]
θ_A	-	Advancing Contact Angle [degrees]
θ_E	-	Equilibrium Contact Angle [degrees]
θ_R	-	Receding Contact Angle [degrees]
θ_{go}	-	Oil-NAPL Contact Angle [degrees]
θ_{gw}	-	Gas-Water Contact Angle [degrees]
θ_{ow}	-	Oil-Water Contact Angle [degrees]
η	-	Liquid-Specific Parameter ($\rho g/\mu$) [1/Lt]
κ	-	Liquid-Specific Parameter in Definition of Effective Tube Radius [-]
μ	-	Dynamic Viscosity [M/Lt]
μ_b	-	Bubble Viscosity [M/Lt]
ξ	-	Supersaturation [-]
ρ	-	Density [M/L^3]
ρ_f	-	Fluid Density [M/L^3]
ρ_g	-	Gas Density [M/L^3]
ρ_l	-	Liquid Density [M/L^3]
Σ	-	Surface Tension Parameter ($4\sigma/\rho g D^2$) [-]
σ	-	Surface / Interfacial Tension [M/t^2]
σ_{nw}	-	NAPL-Water (Non-wetting-Wetting) Interfacial Tension [M/t^2]
σ_{ns}	-	NAPL-Soild Interfacial Tension [M/t^2]
σ_{ws}	-	Water-Solid Interfacial Tension [M/t^2]

σ_{gw}	-	Gas-Water Interfacial Tension [M/t^2]
σ_{gn}	-	Gas-NAPL Interfacial Tension [M/t^2]
ϕ	-	Porosity [-]

Chapter 1
Introduction

1.1 Project Introduction

The migration of gas bubbles in porous media has important implications for various applications, such as *in situ* air sparging and supersaturated water injection for groundwater remediation, the mobilization of residual oil blobs in water-wet reservoirs, and the ebullition of green house gases from deep geological storages to the atmosphere (Pankow *et al.*, 1993; Oldenburg and Lewicki, 2006; Amos and Mayer, 2006; Nelson et al., 2009). Fluidized beds and packed-bed flow reactors are also well-known chemical processes in which gas bubbles flow through porous media (Iliuta *et al.* 1999). Two patterns have been observed for gas flow in granular media: bubble flow and air channels. These flow patterns may exist simultaneously. An important parameter determining the flow pattern is the permeability of the porous medium. Bubble flow usually occurs for grain diameters larger than 1 to 2 mm (Brooks *et al.* 1999).

Groundwater, a major source of water supply for household and industrial uses, has been increasingly polluted by physical, chemical, and biological pollutants in recent years. Among the wide range of industrial chemicals, non-aqueous phase liquids (NAPLs), such as petroleum hydrocarbons and chlorinated solvents, constitute a major source of groundwater contamination. *In situ* air sparging is a common treatment option for removal of NAPLs from contaminated soil and groundwater. This technology involves injecting pressurized air into subsurface water saturated zones via one or more points. As the injected air rises through the saturated aquifer, the volatile free-phase NAPL and other volatile organic compounds (VOCs) dissolved in the water are recovered by a combination of different mechanisms such as volatilization and aerobic biodegradation. The dislodging process allows the contaminants to be carried upwards into the unsaturated zone above the water table. The vapor-phase of NAPL is then collected through vapor extraction wells and treated at ground facilities.

Supersaturated Water Injection (SWI) is a novel technology for the recovery of NAPLs from contaminated soil (Li, 2004). In this patented remediation technology (Li *et al.*, 2007; US Patent 7300227), water supersaturated with CO_2 or air is injected into an aquifer below the NAPL source zone through SWI wells. As the CO_2-supersaturated water flows away from the injection point, the fluid pressure drops and the dissolved gas begins to come out of the solution in the form of bubbles. As the bubbles flow upwards under the action of buoyancy, volatile free NAPLs are recovered by vaporization in the presence of a gaseous phase. The dissolved NAPLs are then removed through enhanced mass transfer

from the liquid phase to the vapor phase due to the high volatility of solute. Furthermore, some residual NAPLs ganglia entrapped in the contaminated porous media may be mobilized upwards and thus removed due to the disconnection and reconnection of gas flow in the presence of water flow (Li, 2009). The gas phase containing contaminants can be removed from the aquifer using this technology.

Waterflooding is an enhanced oil recovery operation in which water is injected into a reservoir to displace residual oil. After waterflooding, a significant fraction of oil remains in the oil field because of capillary trapping. The trapped oil is referred to as waterflood residual oil and its magnitude is highly affected by several parameters such as pore heterogeneities, flooding rate, and wettability. The residual oil can occupy 15% of the pore volume in homogeneous unconsolidated sands and up to 50% of the pore volume in pore networks with a high aspect ratio (Chatzis *et al*., 1983; Chatzis and Morrow, 1984). Waterflood residual oil is mobilized and recovered by chemical flooding at high capillary numbers as well as gravity assisted gas flooding for water-wet conditions using horizontal production wells (Chatzis, 1988; Oren, 1992). Trapped oil mobilization occurs when the viscous forces around an oil blob exceed the capillary forces. A gas bubble rising in porous media has a good potential to carry an oil blob attached to it upwards, since an oil blob that encounters a bubble will spread over it upon contact, resulting in a very high recovery efficiency (Li *et al.*, 2007; Chatzis, 2011). The oil attached to a rising bubble moves to the tailing end and breaks off to the smaller droplets, leaving the detached mass behind. The remaining oil blob may be carried upwards by another rising bubble, as demonstrated by Chatzis (2011).

The buoyancy-driven migration of gas bubbles from sediments makes an important contribution to the transport of gas within aquifers and from aquifers into the atmosphere. Ebullition of gas bubbles from sediments affects bio-geochemical processes and increases the emission of greenhouse gases into the atmosphere (Amos and Mayer, 2006). Microbial decomposition of the organic substances in sediments produces gases, which move through sediments into overlying water and ultimately escape to the atmosphere. Methane is an important greenhouse gas, comprising 37% of total emissions from natural wetlands (Whalen, 2005). Ebullition is a major mechanism for CH_4 transport to the atmosphere, as gas bubbles bypass the unsaturated, oxidized zone of CH_4 consumption. It can account for up to 85% of emissions (Whalen, 2005). Moreover, the groundwater flow and transport of dissolved components and gases through the aquifers are affected by the ebullition of gas bubbles (Ryan *et al*., 2000; Amos *et al*., 2005).

1.2 Project Objectives

Migration velocity of gas bubbles is a critical factor for the *in situ* air sparging, supersaturated water injection, and for many other technologies in which rising gas bubbles play an important role in achieving high process efficiency. Quantitative studies in the literature on the bubble rise velocity in porous media are very limited. Little experimental data on bubble rise velocity, which are necessary to verify the existing theoretical models are available. The data are also important for analyzing the mechanisms and parameters associated with the bubble migration. The objectives of this work were as follows:

- Investigation of the behavior of gas bubble migration in capillary networks. The focus of this work is on the motion of single air bubbles in pore networks through measurement of the bubble rise velocity. An extensive experimental study was conducted to measure the rise velocity of bubbles in porous media and to determine the effects of wetting fluid properties, bubble length and the inclination angle on the bubble rise velocity. The test liquids were kerosene, Soltrol 170, and White Oil with red dye added. Micromodels have been shown to have a great potential in characterizing real porous media and were used for this purpose. Correlations for the bubble rise velocity in terms of easily measurable parameters and dimensionless numbers were obtained.
- Visualization of the migration of air bubbles through a liquid saturated glass micromodel. The motion of air bubbles through the pore network was recorded by a digital camera and analyzed using proper software. Precise video and image analysis were performed to determine the dynamic characteristics of the bubble flow during bubble migration. The dynamic values of bubble length measured for the system were compared to the bubble length at static condition.
- Modification of an existing numerical code developed by Smith (2005) in this study and comparisons of the simulated behavior with experimental data. Simulations involved a 2D network of tubes as a representative of the pore network. The flow pathways around a rising bubble were determined based on the simulation results.

Chapter 2

Background and Literature Review

2.1 Fundamentals of Porous Media Structure and Flow

Porous materials are ubiquitous in nature and technology. Dullien (1992) defined a porous medium as a material that must have two characteristics, namely:

1. The material contains relatively small spaces, named pores or voids, imbedded in the solid or semisolid matrix. The pores are free of solids, are interconnected and may be filled with some fluids.
2. The material can enable the passage of various fluids through its body. That is, a septum made from the material should allow fluids to penetrate through one of its faces and emerge on the other. Such material is referred to as being "permeable".

A porous medium is generally a network of relatively large pore bodies connected by smaller pore throats. Some examples of porous materials are human skin and hair, lungs and bones, textiles and leathers, paper towels and tissues, soil, and many building materials such as concrete and sandstone. Hydrology and petroleum engineering are two important areas of technology that strongly depend on the properties of porous materials. Porous media can be characterized in terms of their macroscopic and microscopic properties. Macroscopic properties such as porosity, permeability, formation resistivity factor and breakthrough capillary pressure describe average behavior of a porous media. Microscopic properties are related to the pore body and pore throat size distribution in the porous sample and pore-to-pore interconnectedness.

2.1.1 Porosity

Porosity ϕ is a measure of the volume of the void spaces in a material. It is defined as the ratio of the volume of pore spaces in a porous medium V_p to the bulk volume V_b given by:

$$\emptyset = \frac{V_p}{V_b} \tag{2-1}$$

The porosity can take any value between zero and one. Two types of porosity exist: "effective" or "interconnected" and "isolated" or "non-interconnected". Effective porosity is the fraction of bulk volume occupied by interconnected pores,which contribute to fluid flow by convection (i. e. conductive

pores) or by diffusion (i. e. non-conductive or dead-end pores) through the porous medium. Dead-end void spaces are inter-connected to the continuum of pore space only from one passage and cannot contribute to convective transport of fluids.

2.1.2 Permeability Concepts and Darcy's law

Permeability is a measure of the ability of a porous material to conduct fluid. Thus, the higher the permeability, the easier is fluid flow through a porous medium with higher permeability is easier. The unit of permeability is the Darcy (D). One Darcy (1 D) is defined as the permeability that will conduct a fluid of 1 mPa.s viscosity at a flow rate of 1 cm^3/s through a cross-sectional area of 1 cm^2 when the pressure gradient is 1 atm/cm. 1 Darcy is approximately equal to 10^{-12} m^2.

The equation that defines permeability in terms of measurable parameters is called Darcy's law. When the fluid flow is sufficiently slow, unidirectional, under steady-state conditions, Darcy's law is expressed by the equation:

$$Q = \left(\frac{k\,A}{\mu}\right)\left(\frac{\Delta P}{L}\right) \qquad (2\text{-}2)$$

where Q is the volumetric flow rate, $\Delta P = P_1 - P_2$ is the pressure drop across a length L, μ is the viscosity, K is the permeability of the porous medium, A and L are the normal cross sectional area and length of the sample, respectively.

2.1.3 Wettability and Contact Angle

In a system including more than one immiscible fluid, the term "wettability" is used to define the tendency of one fluid to preferentially spread over or adhere to a solid surface in the presence of another fluid. Wettability depends on the properties of existing fluids and the solid surface such as interfacial tensions and can be characterized in terms of a contact angle. The contact angle θ is defined as indicated in Figure 2-1 and is usually measured through the liquid phase (Adamson, 1990; Cohen and Mercer, 1993; Hui and Blunt, 2000). According to Anderson (1986), when θ is between 0º and 60-75º, the system is called "water-wet", whereas when θ is between 180º and 105-120º, the system is called "oil-wet". When θ is found to be in the intermediate range, the system is more appropriately defined as "neutrally or intermediately wet".

***θ < 90*:** NAPLs are commonly considered as non-wetting phase relative to water. Water has the greater affinity for the surface than NAPL as illustrated.

***θ > 90*:** A rare case in that the NAPL has greater affinity for the solid surface (wetting) than water (non-wetting) is shown.

***θ = 90*:** A theoretically possible case which can be approached by some mixtures. In this particular condition, the NAPL phase is neutrally wetting.

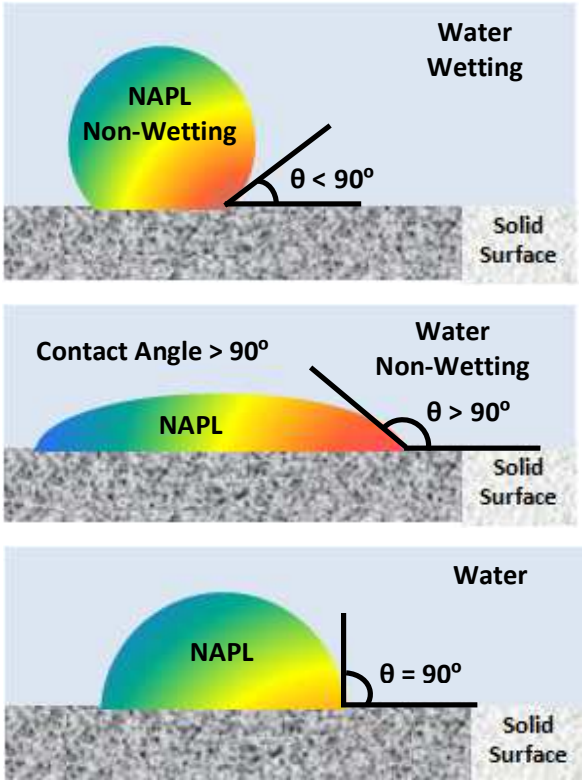

Figure 2-1: Contact Angle and Typical Wetting Fluid Relationships

At equilibrium, the mechanical force balance among the three phases in the direction parallel to the solid surface is expressed by Young's equation (Figure 2-2):

$$\sigma_{ns} - \sigma_{ws} = \sigma_{nw} \cos\theta_{nw} \qquad (2\text{-}3)$$

where σ_{ns}, σ_{ws}, and σ_{nw} are the interfacial tensions between solid and NAPL, solid and water, and NAPL and water, respectively, and θ_{nw} is the contact angle measured through water.

The difference between the maximum (advancing contact angle, θ_A) and the minimum (receding contact angle, θ_R) is called the contact angle hysteresis. Contact angle hysteresis is commonly attributed to surface roughness, surface heterogeneity, and contamination of either the liquid or the solid surface. Contact angle hysteresis can be classified as follows: static and dynamic contact angle hysteresis which refers to the movement of the three-phase contact line in the immiscible displacement. Equilibrium or static contact angle θ_E is defined in the absence of motion of the interface. When the interface starts to move due to the action of an external force, dynamic hysteresis denotes the advancing θ_A and receding θ_R contact angles (Figure 2-3 and Equation 2-4).

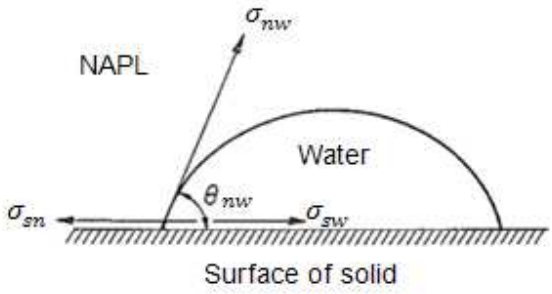

Figure 2-2: Contact Angle at Equilibrium (Craig, 1971)

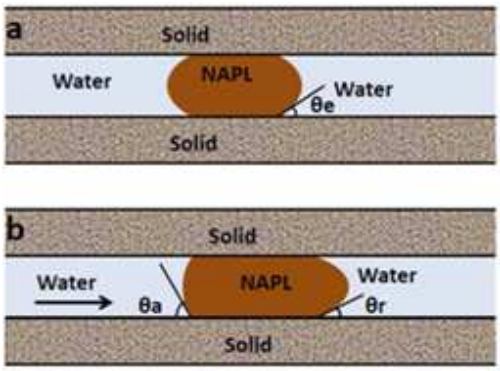

Figure 2-3: Dynamic Contact Angle Hysteresis (Li, 2009)

$$\theta_R < \theta_E < \theta_A \qquad (2\text{-}4)$$

For gas-liquid-solid systems, three different wettability systems can be defined (Chatzis *et al.*, 1988; Hui and Blunt, 2000). First, a water-wet system, in which gas is the non-wetting phase relative to both water and oil (θ_{ow} < 90º, θ_{go} < 90º, and θ_{gw} < 90º, where θ_{ow} is oil/water contact angle, θ_{go} is gas/oil contact angle and θ_{gw} is gas/water contact angle). In this system, water is the most wetting phase, gas is the non-wetting, and oil is the intermediate-wetting. Second, a strongly oil-wet medium, in which gas is wetting to water but non-wetting to oil (θ_{ow} > 90º, θ_{go} < 90º, and θ_{gw} > 90º). In such a system, oil is the most wetting phase, water is the non-wetting, and oil is the intermediate-wetting. Third, a weakly oil-wet system, in which gas is the non-wetting phase relative to both oil and water (θ_{ow} > 90º, θ_{go} < 90º, and θ_{gw} < 90º). Oil is the wetting phase, gas is the non-wetting, and water is the intermediate-wetting phase. The advancing and receding contact angle measurements through the aqueous phase for each wetteability condition were made for PCE-water-solid system and reported by O'Carrol et al. (2005). The primary influence of wettability and capillarity on the distribution of residual NAPLs in a porous medium is shown in Figure 2-4 for the cases of (a) strongly water-wet condition and (b) strongly NAPL-wet condition.

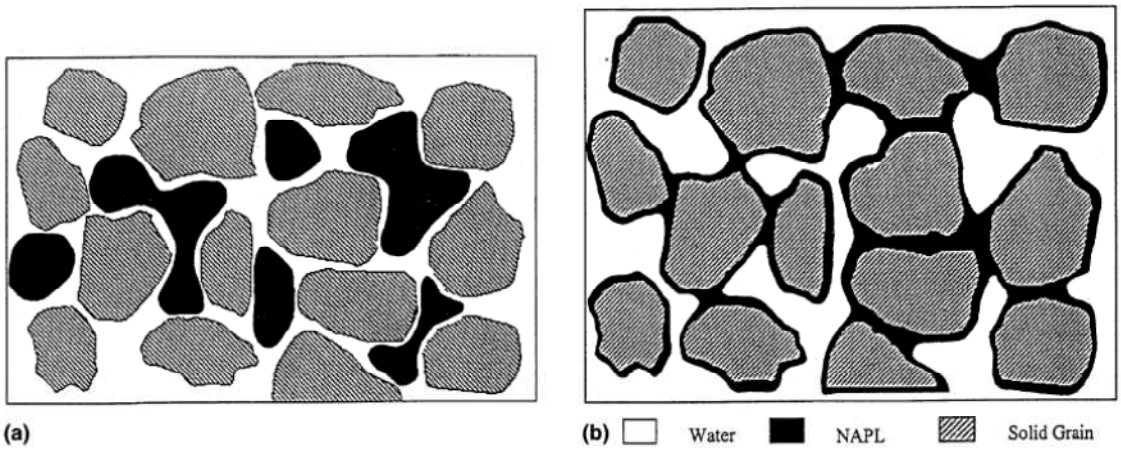

Figure 2-4: Residual NAPL Configuration in a (a) Water-Wet, and (b) NAPL-Wet Porous Media (Sahloul *et al.*, 2002)

2.1.4 Spreading Coefficient

In a three-phase system of NAPL-water-gas in porous media, the tendency of NAPL to spread over the water-gas interface is defined as the spreading coefficient, $S_{n/w}$, by the following equation (Chatzis et al., 1988; Adamson, 1960):

$$C_s = \sigma_{gw} - \sigma_{gn} - \sigma_{nw} \qquad (2\text{-}5)$$

where C_s is the spreading coefficient [N m^{-1}] of oil phase over water in the presence of gas, σ_{gw}, σ_{gn} and σ_{nw} are the water-gas, NAPL-gas and NAPL-water interfacial tensions, respectively. According to Chatzis et al. (1988) and Hirasaki (1993), two different types of contact can occur when a NAPL drop meets a water surface: (1) If $C_s < 0$, as shown in Figure 2-5 **(**a), there is a point where the three phases meet and the NAPL drop will be stagnant on the water surface in the form of lenses. (2) If $C_s > 0$, the interfacial forces are not balanced at a point and, consequently, the NAPL spreads as a film over the water-gas interface, as illustrated in Figure 2-5 (b).

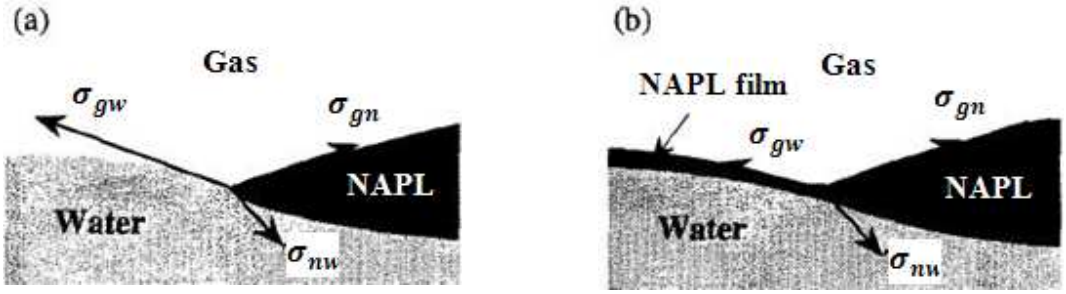

Figure 2-5: NAPL Behavior on a Water-Gas Interface when (a) $C_s < 0$, and (b) $C_s \geq 0$ (Hirasaki 1993; Zhou and Blunt, 1997)

2.1.5 Saturation

In a porous medium containing water, oil, and gas phases occupying the volumes V_w, V_o, and V_g, respectively, the total pore volume V_p is written as:

$$V_p = V_w + V_o + V_g \tag{2-6}$$

The saturation of fluid *i*, S_i, in a porous medium is defined as the fraction of the pore space occupied by fluid *i*. Thus:

$$S_i = \frac{V_i}{V_p} \tag{2-7}$$

where V_i is the volume of pore spaces occupied by fluid *i*. The sum of the saturations of all components in a porous medium is equal to unity.

2.1.6 Capillary Pressure

A basic parameter in the study of the multiphase flow in porous media is the capillary pressure. Capillary pressure is expressed as the pressure differential across an interface between the two immiscible fluids that is synonymous with the pressure difference between the non-wetting phase and the wetting phase. Thus, for an interface formed in a cylindrical capillary tube with radius *r*, the capillary pressure is given by the Young-Laplace Equation:

$$P_c = P_n - P_w = \frac{2\sigma_{nw}\cos\theta}{r} \tag{2-8}$$

where P_c is the capillary pressure, P_w and P_n are the pressures in the wetting and non-wetting phases, respectively and θ is the contact angle. The capillary pressure is a measure of the tendency of a porous

medium to attract the wetting phase and repel the non-wetting phase (Bear, 1972). In water-wet porous media, water invades the smaller pores first, where the capillary pressure is highest, while the non-wetting fluid, when it displaces water, preferentially invades the larger pores first before invading narrower pores. Equation 2-8 predicts a particular value of the capillary pressure that must be reached for a non-wetting phase to enter a pore throat of radius r and is termed as the "threshold capillary pressure".

The relationship between the capillary pressure and fluid saturation is referred to as the capillary pressure-saturation function or capillary pressure curve. When a non-wetting phase invades a water-saturated porous medium, the water saturation decreases and the capillary pressure increases (Figure 2-6). This process is termed as "drainage", as water is drained out of the porous medium. When water invades a porous medium containing a non-wetting phase, in this process the water saturation increases and capillary pressure decreases. This process is referred to as "imbibition". It is noticeable that the capillary pressure versus saturation relationship for imbibition displacement is not the same for the non-wetting phase as for the wetting phase and depends on the saturation history of the system. This behavior seen in capillary pressure-water saturation relationships is referred to as capillary pressure hysteresis. At a given P_c value, two different saturation values are obtained along the drainage curve or the imbibition curve (see Figure 2-6 points A and B).

The saturation at which the non-wetting phase becomes disconnected due to capillary forces is referred to as residual saturation, S_{nwr}. As shown in Figure 2-6, the maximum water saturation achievable during the imbibition process equals ($1-S_{nwr}$). The concept of residual saturation for wetting fluid is different from that for the non-wetting fluid. At residual saturations, the non-wetting phase is disconnected in the form of blobs or ganglia, whereas the wetting phase maintains hydraulic continuity throughout.

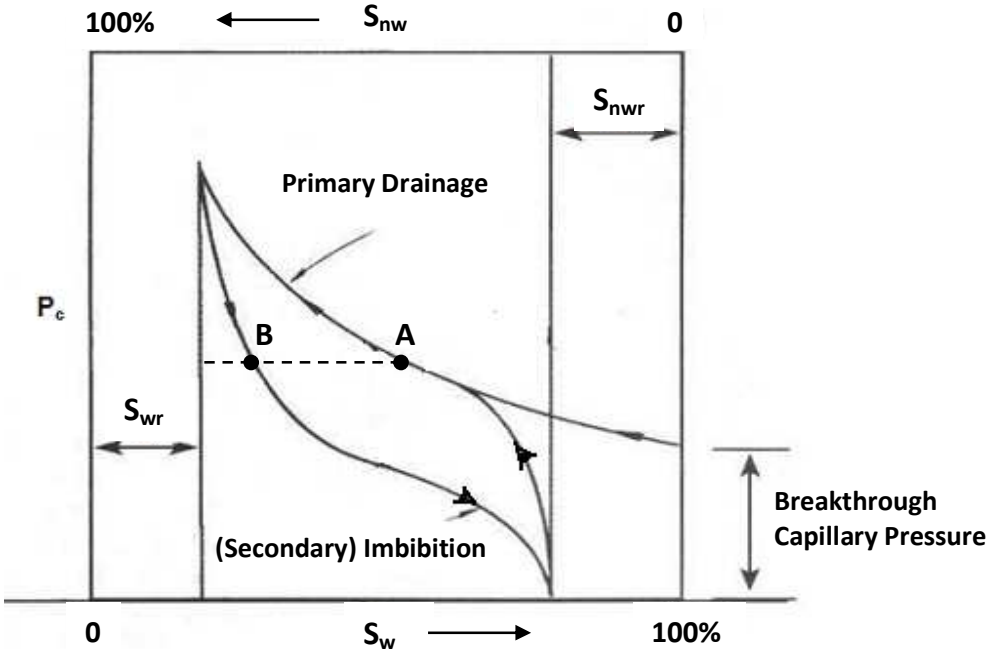

Figure 2-6: Capillary Pressure-Saturation Hysteresis (Pankow and Cherry, 1996)

2.1.7 Microscopic Pore Structure Parameters

Microscopic pore structure characterization is a challenging subject due to the irregular nature of pore geometry. Imagine the void spaces bounded by solid surfaces, the narrower constrictions interconnecting the relatively larger pore spaces are called “pore throats” or “pore necks”, while the relatively larger pore spaces are called “pore bodies” or “node pores”. The parameters describing the topology of pore networks include: (1) the dimensionality of the network, (2) the pore coordination number, and (3) the microscopic topology of the network.

A topological parameter characterizing the interconnectedness of pore structure is “connectivity” or “genus”. Connectivity is a measure of the degree to what a pore structure is connected to other pores (Dullien, 1992). Another parameter relevant to the interconnectedness of pore structure is the “coordination number”. Coordination number Z is defined as the number of pore throats connecting a pore body to the neighbors (Chatzis and Dullien, 1977). In a homogeneous, macroscopic porous medium, the connectivity is a function of the size of the sample, whereas the coordination number is independent of sample size (Dullien, 1992). The “pore size distribution” gives the portion of the pore volume having a characteristic pore size. Several methods exist for determination of the pore size distribution including mercury porosimetry, photomicrographic analysis and sorption-desorption isotherms. The distributions

obtained from each method differ from one another, because the characteristic length used is dependent on the “pore” model used in each case.

2.2 Groundwater Contamination and Remediation Technologies

Any addition of undesirable foreign substances into an ecosystem caused either by human activities or by nature, is considered as contamination. It may be assumed that contaminants left above or under the ground will stay in place. The fact is that groundwater often travels through the subsurface and extends the leaks and spills to areas far beyond the original contaminated site. Groundwater contamination occurs through two types of sources: specific or “point” sources and distributed or “non-point” sources. Examples of point sources include landfills, leaking storage tanks, septic tanks, subsurface waste injection and accidental spills. Road salt, agricultural disposals, atmospheric deposition and land farming chemicals are examples of non-point sources.

2.2.1 Non-Aqueous Phase Liquids (NAPLs)

Non-aqueous phase liquids (NAPLs) are organic chemicals that are associated with human activity and cause severe environmental and health hazards. Based on their density relative to water, NAPLs are categorized in two classes: light non-aqueous phase liquids (LNAPLs), such as petroleum hydrocarbons, and dense non-aqueous phase liquids (DNAPLs) such as chlorinated solvents. These liquids have very low solubility in water. Due to the differences in physical and chemical properties of NAPL and water, an interface forms between the liquids and acts as a barrier for mixing. Most NAPLs are soluble enough in water to reach contamination levels much greater than the permissible drinking water limits. Upon release, light non-aqueous phase liquids (LNAPLs) flow downward to the top of the water table and usually spread as free phase. At contaminated sites, DNAPLs travel rapidly downward within the subsurface and leave the trapped ganglia of DNAPL behind due to capillary forces (Figure 2-7).

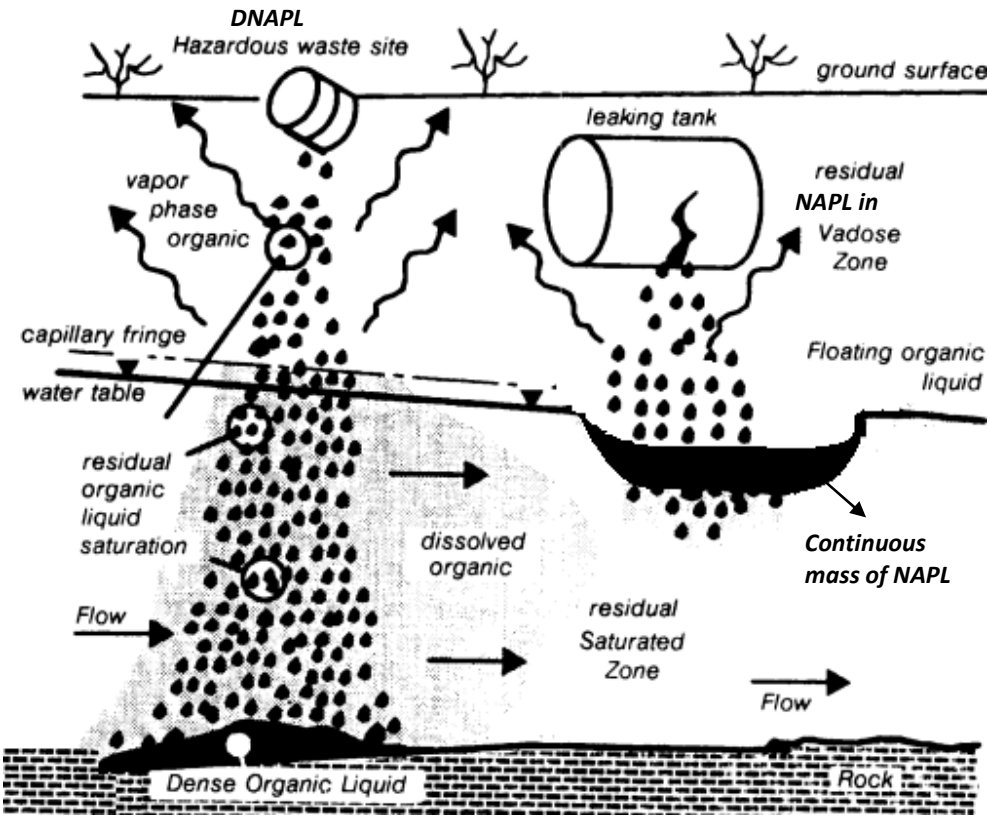

Figure 2-7: Schematic of DNAPL (Left) and LNAPL (Right) Distribution in an Aquifer (Edited after Wilson *et al.*, 1990)

2.2.2 NAPL Remediation Technologies

For NAPL release sites, contamination may be contained in a subsurface source zone and/or a groundwater plume. The source zone includes contaminant free phase, residual, and adsorbed NAPL mass. A groundwater plume denotes a body of dissolved NAPL in groundwater in an aquifer that originates from a specific source of contamination and extends further downward and outward due to groundwater flow (Figure 2-8).

Two types of technologies have been developed for source zone restoration: (1) the methods that bring contaminant to the surface for treatment or disposal above the ground, such as flushing with steam, air, surfactant, or co-solvents, and (2) those that destroy DNAPLs *in situ* such as chemical oxidation, chemical reductive de-halogenation, and bioremediation.

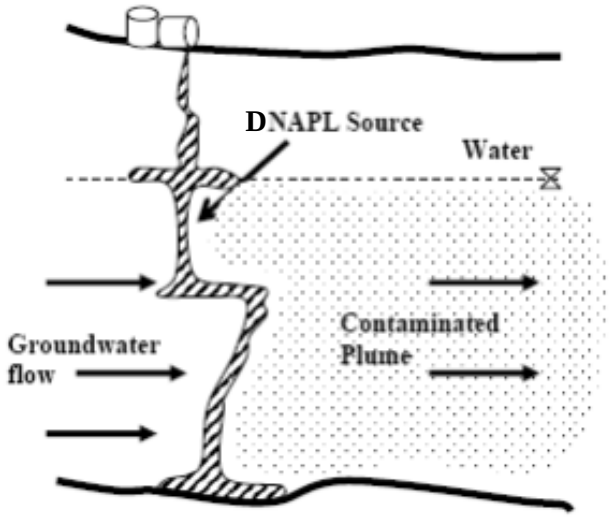

Figure 2-8: DNAPL Source and Plume in the Subsurface (Li, 2004)

For the successful implementation of remedial strategies, the NAPL-contaminated sites and source zones must be well-characterized beforehand (Cohen and Mercer, 1993; Chambers *et al.* 2004). The site characterization generally includes assessment of (1) the types of chemicals that are found as contaminant, (2) how these chemicals have been used, (3) the types of site manufacturing operations, and (4) the potential depth of DNAPL penetration through the subsurface.

2.2.2.1 Pump and Treat Technology

Pump and treat is the most conventional remediation technique, which includes pumping the contaminated groundwater to the surface and treating it above the ground for further reinjection into the subsurface or discharging to a surface water body or municipal wastewater plant. This method can be used alone as a treatment system or in conjunction with other technologies for two purposes: (1) containment, to control the contamination spreading and (2) NAPL restoration, to extract the contaminant mass. The mechanisms associated with this technology to remove the NAPLs are mobilization and dissolution. Pump and treat is not effective for recovery of NAPLs by displacing the residuals due to high hydraulic pressure gradients required to overcome the capillary forces (Mackay and Cherry, 1989; Haley *et al.*, 1991). Moreover, the removal of NAPLs by solubilization to a reduced level of contamination may take decades because of the low solubility of NAPLs in water (Johnson and Pankow, 1992).

The popularity of this method is because of its simplicity and usage in the past. In reality, pump and treat systems have shown to be extremely inefficient and limited by mass transfer and their capability is

practically limited to plume or source zone containment. Such systems have a limited advantage in most contaminated sites since the remediation cost and the length of clean up time increases exponentially with the extent of removal (Figure 2-9).

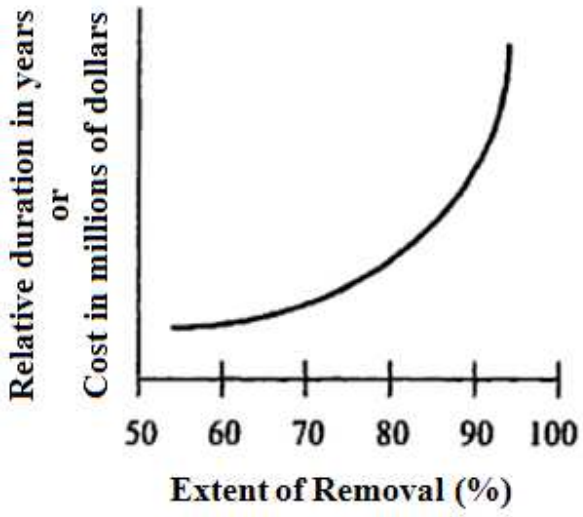

Figure 2-9: Typical Relationship between the Removal Percentage and the Relative Cost or Duration of a Conventional Pump and Treat Technology (NRC, 1994)

2.2.2.2 In-Situ Air Sparging Technology

In situ air sparging (IAS) is a technology in which compressed air is injected below the contaminated zone via one or more injection wells. As the injected air spreads through the saturated area, volatile compounds are removed by a combination of mechanisms such as volatilization, dissolution, adsorption/desorption, and aerobic biodegradation due to the introduction of oxygen (Johnson et al. 1993). This method is applicable for removing volatile organic compounds (VOCs) existing in the forms of dissolved contaminants in the groundwater, sorbed to the soils, and entrapped in soil pores of the saturated zone. Direct volatilization of the sorbed and trapped contaminants (NAPLs), however, is the most dominant process for mass removal during in situ air sparging (Semer and Reddy, 1998). IAS is used in conjuction with soil vapor extraction system (SVE) to collect the vapor phase.

The effectiveness of in situ air sparging for remediation depends on the mass transfer between the aqueous phase with the NAPL and the gas phase. The IAS performance is governed by several design parameters including air distribution (zone of influence), depth of air injection, pressure and flow rate of

air injection, injection mode (pulsing or continues), injection well construction, and contaminant type and distribution. Figure 2-10 shows a conceptual model of in situ air sparging.

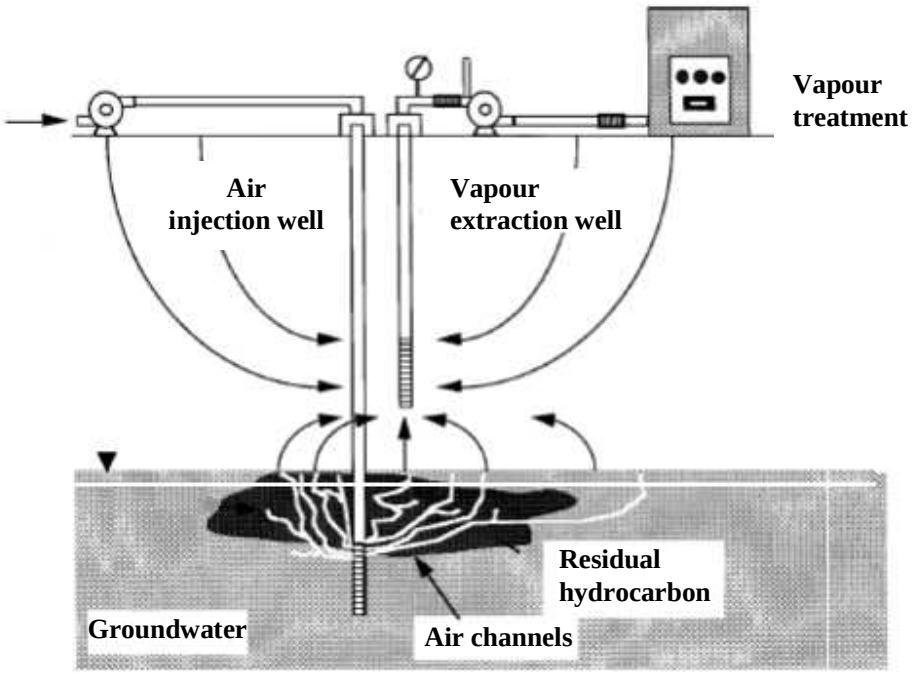

Figure 2-10: Schematic of In-Situ Air Sparging (Edited after Johnson, 1998)

2.2.2.3 Supersaturated Water Injection

A novel remediation technology for recovery of NAPLs from contaminated ground sources is supersaturated water injection (SWI). SWI is similar in many respects to *in situ* air sparging, however, SWI is based on the injection of gas-saturated water at high pressures. In this method, high concentrations of gas (e.g. CO_2 or air) are dissolved in water at elevated pressures. The water supersaturated with gas is introduced into the contaminated region below the NAPL source zone through the injection wells. As the water flows away from the injection point depending on the flow rate, injection pressure, and the hydraulic conductivity of the porous medium, gas bubble nucleation begins and NAPL is recovered by taking advantage of the high volatility of most NAPLs and their ability to spread over the water in the presence of gas. The volatility of the contaminant allows enhanced mass transfer from dissolved, adsorbed, and free phases into the vapor phase. The recovery mechanisms associated with SWI include displacing NAPL held in the pores by rising gas bubbles towards the ground surface and evaporating NAPL into the growing gas bubbles. Li (2004) conducted glass column experiments to study SWI for

NAPL recovery. His results indicated that SWI was very effective in recovery of residual volatile NAPLs. Although most of the residual contaminants were removed through volatilization, some residual NAPL was removed by mobilization during SWI.. Figure 2-11 shows a conceptual model of SWI.

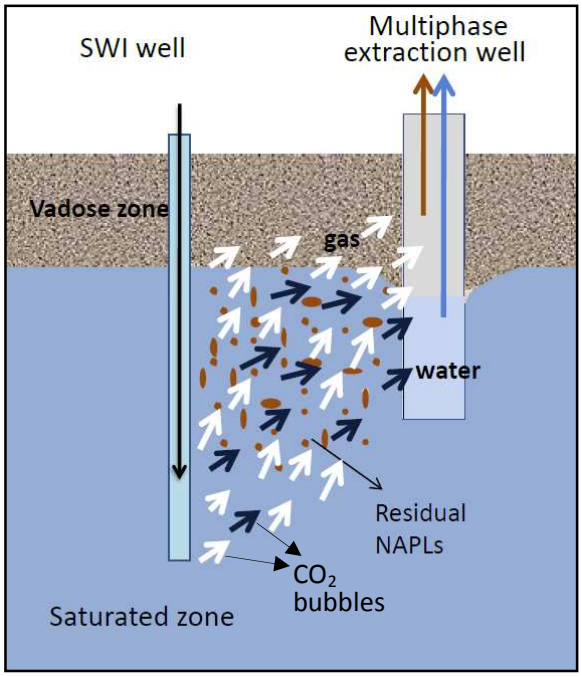

Figure 2-11: A Conceptual Model of Supersaturated Water Injection Technology (Li, 2004)

2.3 Residual Oil Mobilization

Chatzis *et al.* (1988) and Oren *et al.* (1992) studied the pore scale mechanisms associated with the mobilization of waterflood residual oil by gas injection for water-wet systems. Experiments of Oren *et al.* (1992) consisted of 2D glass micromodels with two different three phase (oil-water-gas) systems: one with a positive spreading coefficient, and the other with a negative coefficient. Double-drainage mechanism that includes joint gas-oil and oil-water displacements was responsible for displacement in both systems. The results showed a significantly higher oil recovery for the system with positive spreading coefficient. In such a system, flow through continuous, thin oil films between the gas and water resulted in the enhanced oil displacement and, consequently, higher recovery. Contact between the injected gas and residual oil is very important for the mobilization of waterflood residual oil by gas flooding, as it governs the mass transfer between the phases. It was found that the capillary pressure is a critical factor in determining the gas access to residual oil (Jones, 1985; Holm, 1986, Kantzas *et al.*,

1988). Moreover, Kantzas *et al.* (1988) and Chatzis *et al.* (1988) showed that gravity forces, flow through thin films, and interfacial tensions between gas-water and gas-oil are important parameters in the mobilization of residual oil and subsequent recovery.

Chatzis (2011) recently investigated the mobilization of residual oil in three scenarios: (1) mobilization with increased capillary number, (2) mobilization with rising gas bubbles in simple pore networks, and (3) mobilization by pressure pulsing, using water wet glass micromodels. The recovery of waterflood residual oil is possible by chemical flooding at high capillary numbers, which are much larger than the capillary number required for mobilization of the largest oil blobs in place (Chatzis, 2011). To determine the effect of increased capillary numbers on the mobilization of waterflood residual oil, the displacement experiments were performed by injection of water at a low flow rate into the glass micromodel containing initial oil saturation. The injection flow rate was then gradually increased and the corresponding residual oil saturation was measured. Capillary number for each water flow rate was calculated and, thus, the fraction of residual oil remaining in place as a function of flow rate and calculated capillary number was obtained (Figure 2-12). As seen, the fraction of residual oil remaining in the micromodel decreased by increasing the water injection flow rate and, consequently, capillary number (i. e. the mobilization of residual oil increased). The oil blob mobilization at high capillary numbers is associated with the break-up of blobs to smaller droplets. Moreover, the results of Chatzis (2011) showed that the mobilization of residual oil by rising gas bubbles is an effective mechanism for oil recovery and for clean up in contaminated aquifers. A residual oil blob that attaches to the bubble upon contact, stays at the rear of it, breaks off to a smaller blob and is carried upwards as the bubble rises (Figure 2-13). Similarly, the detached oil blob remaining is re-mobilized and recovered by subsequent rising of gas bubbles.

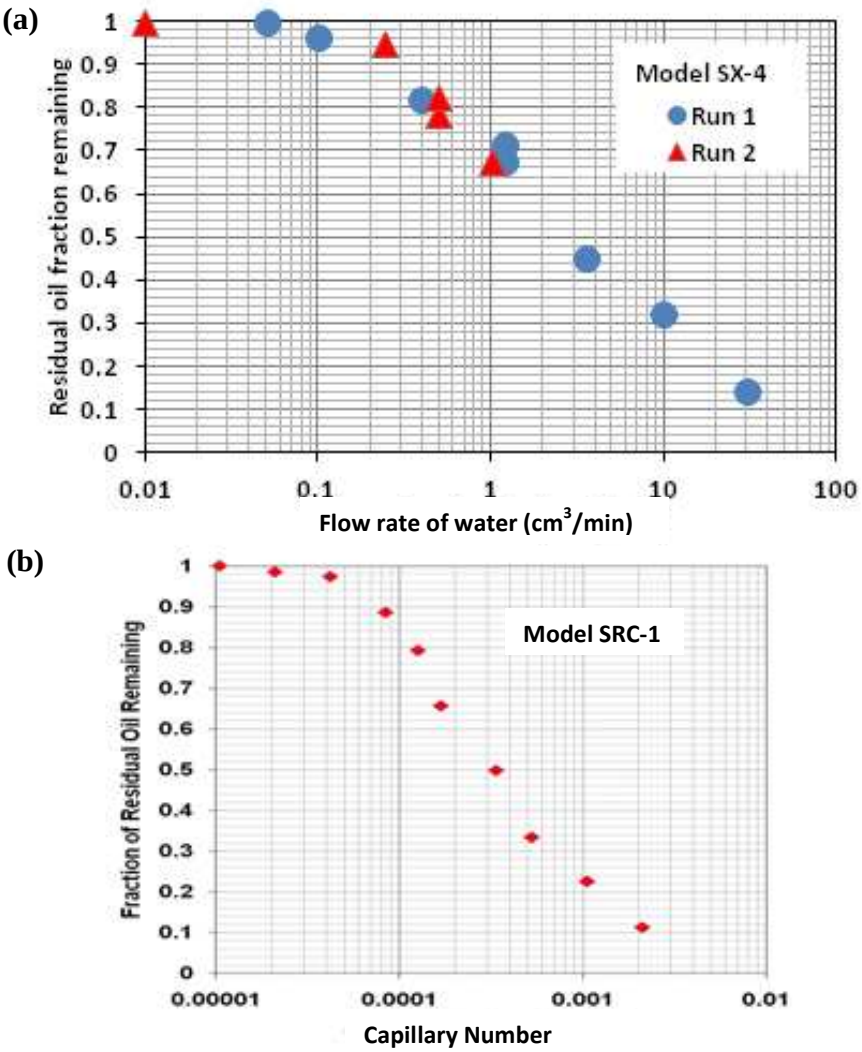

Figure 2-12: Fraction of of Residual Oil as a Function of (a) Injection Flow Rate and (b) Capillary Number (after Chatzis, 2011)

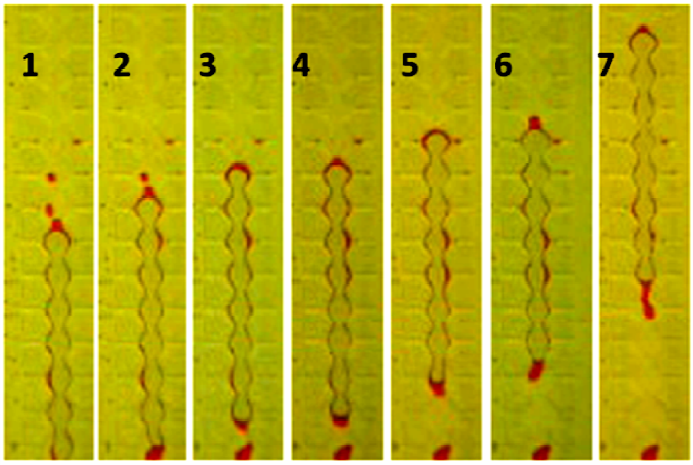

Figure 2-13: Mobilization of Oil by a Rising Bubble (after Chatzis, 2011)

2.4 Fundamentals of Bubble Nucleation

Bubble formation is important in many industrial and natural processes such as *in situ* air sparging and supersaturated water injection for groundwater remediation, cavitation (Young, 1989), and ebullition of greenhouse gases from the geological formations to the atmosphere. Thus, the mechanisms of bubble production and growth are discussed here.

Bubbles are formed when a supersaturated liquid undergoes a phase change. Supersaturation may be achieved by changing the temperature and pressure of the system, which affects the solubility of the gas in the liquid. For a given temperature and pressure, if the concentration of the gas in the liquid exceeds the equilibrium concentration, the liquid becomes supersaturated. At equilibrium conditions, the concentration of a dissolved gas in a liquid is related to the partial pressure of the gas in the vapor phase according to Henry's law:

$$P_i = H_i \cdot x_i \tag{2-9}$$

where P_i is the partial pressure, H_i is the Henry's constant, and x_i is the mole fraction of dissolved component i in the liquid. H_i is a value unique to substance i that depends on the solute, solvent and temperature. The solubility and vapor pressure of a component are functions of temperature; consequently, the Henry's constant also depends on the temperature. To view the concept of supersaturation from the pressure perspective, a system with the initial solute concentration x_1 and the partial pressure P_1 is considered. If the pressure is reduced from P_1 to P_2, the system becomes

supersaturated since x_1 exceeds the equilibrium concentration x_2 at the reduced pressure P_2. Lubetkin and Blackwell (1988) defined the supersaturation ξ for such a system as:

$$\xi = \alpha - 1 = \frac{x_1}{x_2} - 1 \tag{2-10}$$

where α is termed as the supersaturation ratio. Furthermore, the difference in the equilibrium partial pressure of the solute is:

$$\Delta P = P_1 - P_2 = H(x_1 - x_2) = H \cdot x_2 \left(\frac{x_1}{x_2} - 1\right) = P_2 \xi \tag{2-11}$$

Jones *et al.* (1999) conducted a comprehensive review of bubble nucleation. In their review, the term nucleation was used for the autogenous formation of a bubble and four major types of nucleation were described as follows:

Type I - Classical homogeneous nucleation: This type involves bubble formation in the liquid bulk of a homogeneous solution without any gas cavity present before supersaturation, requiring very high levels of supersaturation. The formed bubbles rise to the surface of the liquid. Further bubble formation at the same location is very rare.

Type II - Classical heterogeneous nucleation: This form of nucleation is very similar to type I where the bubble formation occurs in the absence of pre-existing gas cavities in the system and requires high levels of supersaturation. The bubble nucleation occurs when the supersaturation is suddenly induced and is catalyzed by the presence of another material in the liquid. The formed bubbles then detach and leave behind a portion of their gas. Figure 2-14 illustrates types I and II.

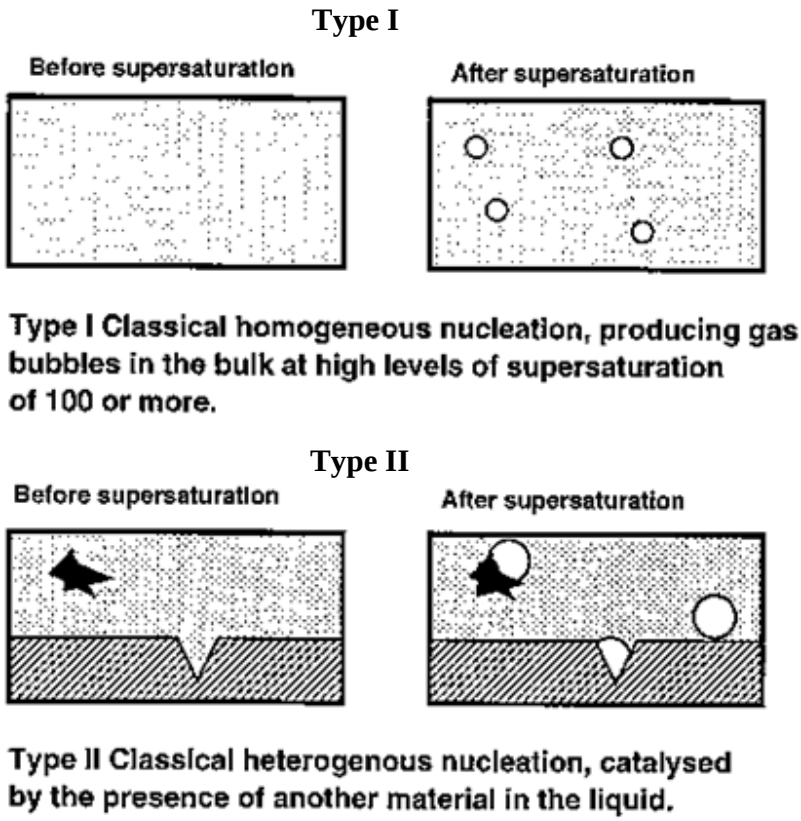

Figure 2-14: Type I and II Classical Homogeneous and Heterogeneous Nucleation (after Jones *et al.*, 1999)

Type III – Pseudo-classical nucleation: In this type, nucleation occurs at pre-existing gas cavities at the surface of the container and particles, and in the form of micro-bubbles in the liquid. At the moment the supersaturation occurs, the radius of curvature of each meniscus is less than the critical nucleation radius, as determined by the classical theory. Hence, there exists a nucleation energy barrier for each cavity, which must be overcome. The critical nucleation radius is given by:

$$R^* = \frac{-2\sigma}{\Delta g_v} \tag{2-12}$$

where Δg_v is the bulk free energy per unit of liquid volume. This type of nucleation can occur at low supersaturation levels and the local supersaturation fluctuations result in the bubble nucleation at cavity sites.

Type IV – Non-classical nucleation: In this type, there is no nucleation energy barrier to overcome since the nucleation occurs at pre-existing gas cavities with radii of curvature greater than the critical nucleation value, which are stable sources for bubble nucleation. Similar to type III, the bubble nucleation occurs in the presence of pre-existing gas cavities at the surface of the container or somewhere else in the liquid. Pre-existing gas cavities with the menisci radii curvature larger than a critical value are responsible for bubble nucleation. Types III and IV nucleation are shown in Figure 2-15.

Type III and IV

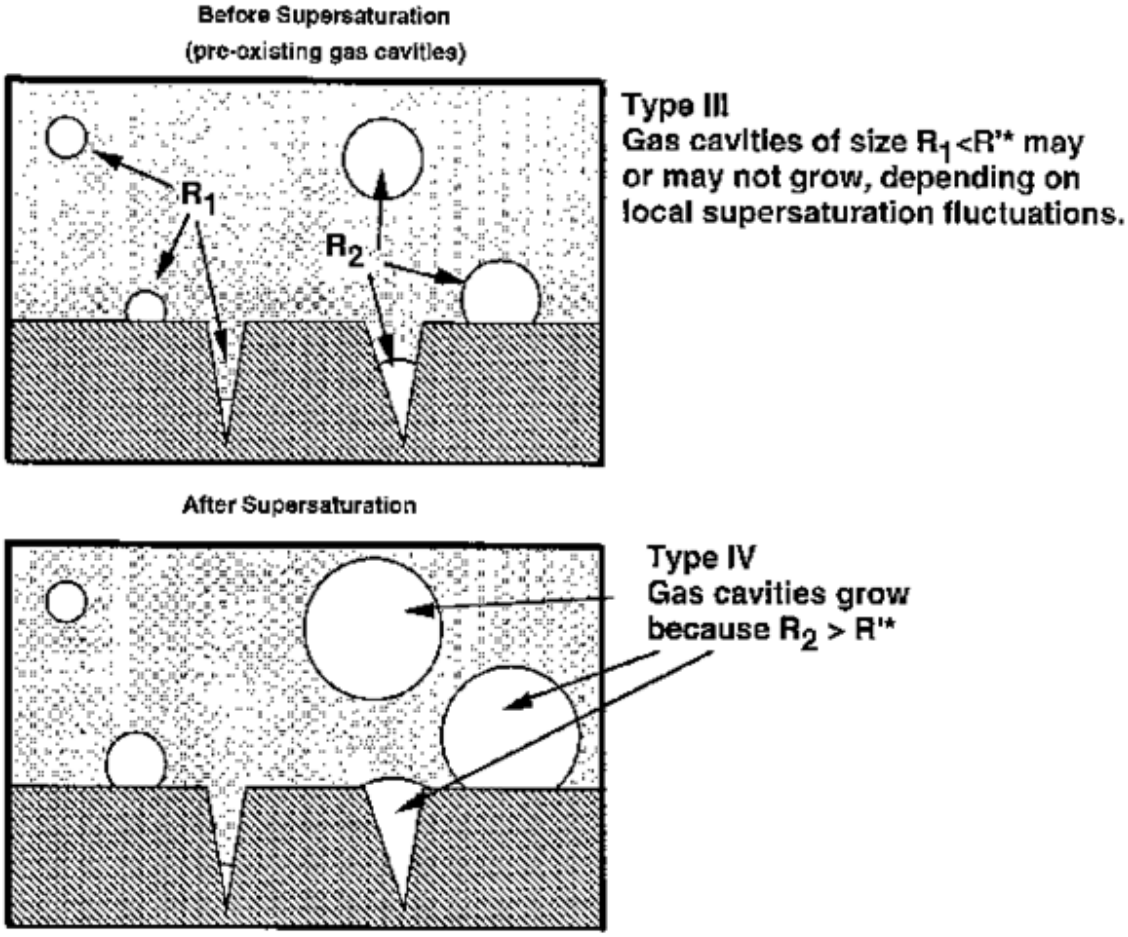

Figure 2-15: Type III Pseudo and Type IV Non-classical Nucleation (after Jones et al., 1999)

2.5 Migration Velocity of Bubbles

2.5.1 Bubble Rise Velocity in Tubes

Bretherton (1961) studied the motion of a long bubble moving steadily at small Reynolds number in a circular horizontal tube. Two related problems were analyzed in his work. In the first condition, the tube radius was so small that gravitational effects were negligible. It was shown mathematically that the velocity of the bubble u_b exceeds the average speed of the suspending fluid v_f by an amount $u_b W$ where W is given by:

$$W = 1 - \frac{v_f}{u_b} \tag{2-13}$$

W is related to the capillary number $(\mu u_b/\sigma)$, where μ is the dynamic viscosity of the suspending fluid and σ is the interfacial tension between the bubble and the wetting liquid, by the following equation:

$$W \cong 1.29\,(3Ca)^{2/3} \qquad \text{as} \qquad \text{Ca} \rightarrow 0 \tag{2-14}$$

Equation 2-14, which is based on the assumption that the bubble is of infinite length, is in error by no more than 10% if $Ca < 5\times10^{-3}$. The pressure drop ΔP_b across such a bubble is expressed by:

$$\Delta P_b \cong 3.58\,\frac{\sigma}{r}\,(3Ca)^{2/3} \qquad if \qquad Ca \leq 10^{-2} \tag{2-15}$$

where r is the tube radius.

Ratulowski and Chang (1989) provided a correction to Equation 2-15 for the next-order term as:

$$\Delta P_b \cong \frac{\sigma}{r}\left[3.58\,(3Ca)^{2/3} - 9.07Ca^{0.95}\right] \tag{2-16}$$

Equation 2-15 is a good approximation for $Ca \leq 10^{-2}$, whereas Equation 2-16 is useful for Ca up to 10^{-1} (Stark and Manga, 2000). Ratulowski and Chang (1989) extended the analysis of Bretherton (1961) for infinite bubbles to single bubbles of finite length with volumes V_b larger than V_c:

$$V_b > V_c = \frac{4}{3}\pi r^3 \tag{2-17}$$

Olbricht (1996) showed that the velocity of bubbles of infinite length is a good approximation for bubbles of finite length if $V_b > 0.95V_c$ (V_c is the volume of a spherical bubble with the same radius as the tube).

Ratulowski and Chang (1989) also studied bubble trains in tubes and surprisingly found that single bubbles in trains behave as an isolated bubble at low capillary numbers.

In the second problem, Bretherton (1961) analyzed the motion of a bubble in a wider, vertical sealed tube and found that in this condition, the motion of a bubble under gravity effects is completely prevented if:

$$\frac{\rho\, g\, r^2}{\sigma} < 0.842 \tag{2-18}$$

where ρ is the density difference between the bubble and the suspending fluid. However, for larger radii, the rate of free rise increased according to the following equation:

$$\frac{\rho\, g\, r^2}{\sigma} - 0.842 \cong 1.25 \left(\frac{\mu\, u_b}{\sigma}\right)^{2/9} + 2.24 \left(\frac{\mu\, u_b}{\sigma}\right)^{1/3} \quad if \;\; 0.842 < \frac{\rho\, g\, r^2}{\sigma} < 1.04 \tag{2-19}$$

Bendiksen (1984) experimentally investigated the motion of long air bubbles suspended in a constant liquid flow in inclined tubes. Effects of tube inclination angle and tube diameter on the bubble motion were determined through experiments by measuring Reynolds and Froude numbers. Experiments were performed using a transparent tube with the diameter of 2.42 cm for 13 different inclination angles between -30 and +90º, and additional tests were performed with tube diameters equal to 1.92 and 5.0 cm for $\theta \leq 0^o$. The results showed that for all inclination angles, the correlation given by Nicklin *et al.* (1962) for the bubble propagation rate in vertical tubes for 8000 < *Re* < 50,000 fit the experimental data well:

$$u_b = C_0 u_l + u_0 \tag{2-20}$$

but with $C_0 = C_0\,(Fr, Re, \Sigma, \theta)$ and

$$u_0 = u_0^*\,(Fr, Re, \Sigma, \theta) \cdot \left[g\, D\, \left(1 - \frac{\rho_g}{\rho_l}\right)\right]^{1/2} \tag{2-21}$$

$$u_0^* = \frac{u_0}{\sqrt{g\, D}} \tag{2-22}$$

$$\Sigma = \frac{4\,\sigma}{g\, \rho_l D^2} \tag{2-23}$$

$$Re = \frac{\rho_l\, u_l\, D}{\mu_l} \tag{2-24}$$

where u_l is the average velocity of the liquid, u_0 is the bubble rise velocity in the stagnant fluid, u_0* is the dimensionless bubble propagation rate, Σ is the surface tension parameter, θ is the inclination angle, D is the tube diameter, $Re = (\rho_l u_l D/\mu)$ is Reynolds number, $Fr = u_l/(gD)^{1/2}$ is Froude number, and C_0 is the distribution slip parameter. Based on his experimental results, Bendiksen (1984) found that when $\theta \geq 0^o$ and $Fr \leq 3.5$, coefficient C_0 varies from 1.00 to 1.20 while when $\theta > 0^o$ and $Fr \geq 3.5$, C_0 approaches 1.19-1.20 for all inclinations.

Bendiksen (1985) studied the motion of long bubbles in very long cylindrical vertical tube with the particular attention on the effects of both liquid motion caused by external forces and surface tension on the bubble velocity and the bubble shape. Analytical expressions for the bubble velocity in a stagnant liquid were proposed and numerical predictions for the bubble velocity in a flowing liquid for both laminar and turbulent velocity profiles were presented. In the laminar flow regime, liquids with a parabolic velocity profile increased the liquid flow downward close to the bubble surface at the bubble nose.In the turbulent velocity profiles, the increase in the bubble rise velocity due to the liquid velocity decreased with increasing Reynolds number since the velocity profile is flattened.

Nickens and Yannitell (1987) studied the rise of large bubbles in a closed, vertical tube filled with a liquid using potential flow theory. Potential flow theory is applicable to problems when the liquid has very small or negligible viscosity so that the boundary film at the wall of the tube is thin. Nickens and Yannitell (1987) extended the works of previous authors and added the effects of surface tension on the bubble shape by using the Kelvin-Laplace equation, which is significant in small tubes. They also took into account the effects of the liquid film thickness between the bubble and the tube wall by adding a viscous correction term into the solution, enabling the prediction of rise velocity for bubbles in liquids of moderate viscosity.

Nickens and Yannitell (1987) applied the Stokes stream function, which is an infinite series of Bessel functions, to express their solution to the problem. Furthermore, the analysis for the shape of the bubble nose was expanded in a Taylor series using the Laplace equation. A correlation was found for the bubble rise velocity by truncating both series after one term, i.e.:

$$u_b = 0.361\sqrt{2\,g\,r}\left(1 - \frac{14.68}{Eo}\right)^{1/2} \qquad (2\text{-}25)$$

where r is the tube radius, *Eö* is Eötvös number and u_b is the bubble velocity. The Eötvös number is defined by:

$$E\ddot{o} = \frac{\rho\, g\, D^2}{\sigma} \tag{2-26}$$

where D is the tube diameter.

The effect of the liquid viscosity was accounted for by defining an effective tube radius, r_{eff}, as:

$$r_{eff} = r\ - \kappa\delta \tag{2-27}$$

where κ depends on the liquid properties and $0 \leq \kappa \leq 1$, and δ is the thickness of the fully developed laminar liquid film at the wall. Parameter κ is expected to be equal to zero for an ideal liquid (no boundary layer) and generally increase with viscosity. It is shown that Equation 2-27 applies for viscosities up to a maximum at which κ = 1. Beyond this, the boundary layer is thicker than the fully developed film and a viscous analysis is required (the potential theory fails). By applying the mass and momentum balance to the fully developed laminar liquid film, the bubble velocity was found as:

$$u_b = \frac{2\,\eta\, r^2}{3} \cdot \frac{\varepsilon^3}{1-\varepsilon} \tag{2-28}$$

$$\varepsilon = \frac{\delta}{r} \tag{2-29}$$

$$\eta = \frac{\rho\, g}{\mu} \tag{2-30}$$

where ε is the dimensionless film thickness and η is a function of the liquid properties. In a practical method, it was assumed that κ is an exponential function of the non-dimensional liquid property number N_p:

$$\kappa = 6.40\, N_p^{-0.60} \tag{2-31}$$

$$N_p = \left(\frac{\rho^2\, g\, r^3}{\mu^2}\right)^{1/2} \tag{2-32}$$

ρ and μ are the density and viscosity of the liquid, respectively. Equation 2-32 is valid only for $N_p \geq 22$ (i.e. κ = 1). Due to the lack of information given on calculating δ, the applicability of the above equations is very limited.

Bico and Quéré (2002) studied the rise of a bubble in a vertical, closed, capillary tube with square or rectangular cross section, which traps liquids in its corners. For an air bubble rising in a closed square tube partially filled with a wetting fluid ($\theta = 0^o$), they considered the possible existence of a microscopic wetting film around the bubble connecting liquids above and below it. If such a film exists, the bubble would rise under gravity effects, although very slowly because of the thinness of the films. The drainage velocity due to gravity effects through the liquid film was calculated by Poiseuille's law, as:

$$u = \frac{\delta^2}{3\mu}\,\rho g \tag{2-33}$$

where δ is the wetting film thickness. A typical value for the bubble velocity was found to be as small as 10^{-13} m/s. In order to increase these low values, the film of liquid around the bubbles must be thicker. Thus, Bico and Quéré (2002) adopted a similar approach as Dong and Chatzis (1995) and extended their work to angular capillary tubes, in which liquid is also trapped in the corners. They obtained the following correlation for the bubble rise velocity:

$$u_b = 4.8 \times 10^{-5}\,\frac{\rho g a^2}{\mu} \tag{2-34}$$

where a is the characteristic size of the tube (a is equal to the length of a side for a square tube).

2.5.2 Bubble Migration Velocity in Porous Media

Understanding the behavior of air bubbles in porous media has been the subject matter of various studies. Ji *et al.* (1993) conducted a qualitative study to investigate the flow of air through a saturated porous medium and the effects of heterogeneity. Their laboratory experiments consisted of the injection of air through a diffuser into a Plexiglas tank packed with glass beads and visualization of the airflow through the porous medium. They observed two distinct airflow patterns depending on the grain size: air plumes with discrete bubbles for bead sizes of 4-mm or larger and air plumes with continuous air channels for bead sizes of 0.75-mm or less. Figure 2-16 shows the airflow patterns observed by Ji *et al.* (1993). In the work of Wehrle (1990), air phase migrating in soil was found in the form of rising bubbles, where soils were considered as fine gravel with diameter of 3 mm and medium gravel with diameter of 6 mm. McCray and Falta (1997) performed a numerical simulation to model the two-dimensional experiments conducted by Ji *et al.* (1993).

Bubble migration in porous media has been studied using glass micromodels, glass plates with etched channels and pores. Glass micromodels are two-dimensional network patterns composed of pore bodies

connected by pore throats (Chatzis, 1982; McKellar and Wardlaw, 1982). They are potential tools to demonstrate fluid flow through porous media. Goldenberg *et al.* (1989) observed the adhesion of clay minerals on the surface of air bubbles and the transport of units formed by bubbles and particles in a micromodel. Wan and Wilson (1994) performed visualization experiments to investigate the role of gas-water interfaces on the transport of colloid particles in porous media using glass micromodels. Their results suggested that colloidal particles sorb preferentially at the gas-water interface rather than at the solid-water interface in porous media, retarding the transport of particles if stagnant.

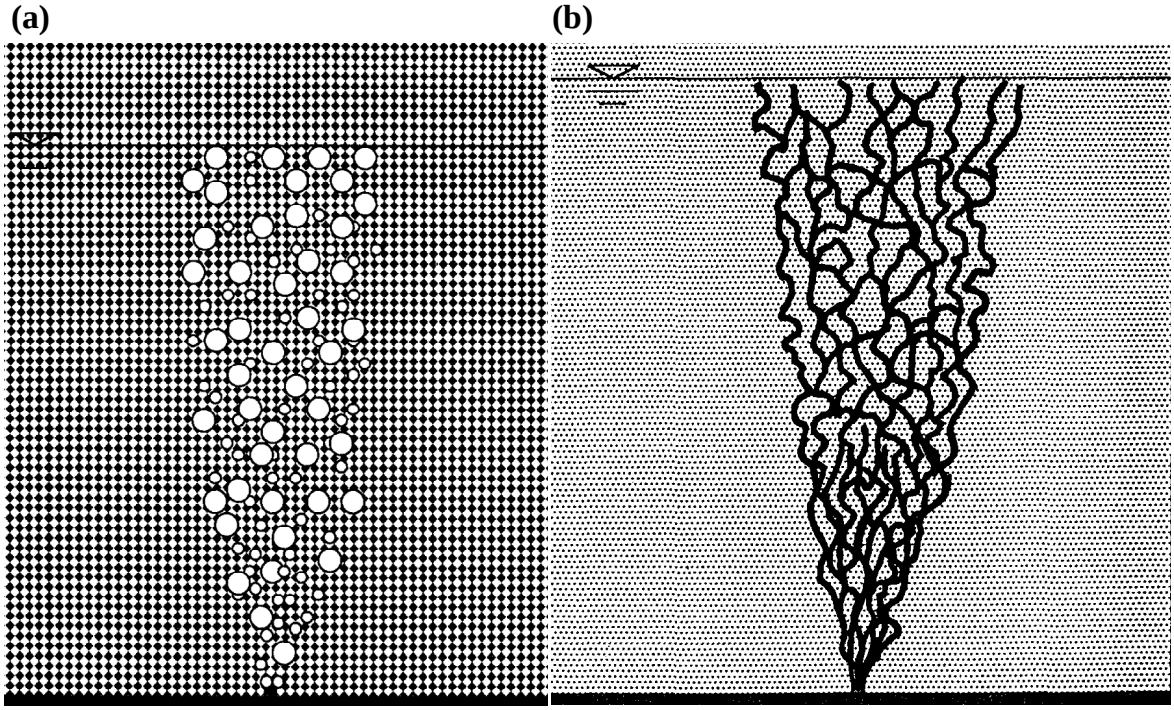

Figure 2-16: Schematic of Air flow Patterns at Moderate Air Injection Rates: (a) Bubble Flow in 4-mm Particle Diameter Uniform Medium and (b) Air Channels in 0.75-mm Particle Diameter Uniform Medium (Ji *et al.*, 1993)

Roosevelt and Corapcioglu (1998) were the first to do a quantitative study to measure the terminal velocity of air bubbles rising in a stationary porous medium using video recordings. In their experiments, single air bubbles of varying sizes were injected into the bottom of two glass bead columns of different diameters, 3.9 and 3.6 cm inside diameter, packed with 4-mm glass beads. Both columns were filled to a height of 90 cm of beads with 10 cm of water above and left open from the top. Two video camcorders and a light source were used to record and visualize the bubble motion through the columns. Figure 2-17

shows a schematic of their experimental set-up. Images of the single bubbles rising in the porous medium were obtained by capturing frames from the videotape and enhancing with an image analyzer. Vertical rise velocity was then determined by measuring the displacement of a bubble from the top of the porous medium and plotting the displacement versus time with a linear best fit. The volume of a bubble was determined by capturing a frame of the bubble in the water above the beads just after it exited the porous medium and comparing it to the images of bubbles of known volume. Velocities measured for bubbles with equivalent radius varying from 0.2 to 0.5 cm, were in the range between 16.7 and 20.2 cm/s. Their results for the rise velocities of bubbles in the porous medium displayed a linear dependency on time. Roosevelt and Corapcioglu (1998) found that the data measured for the velocity of air bubbles in the porous medium were 17.4-27.4% smaller than the values obtained for single bubbles rising in a column filled with only water, while the corrections for wall effects were made accordingly.

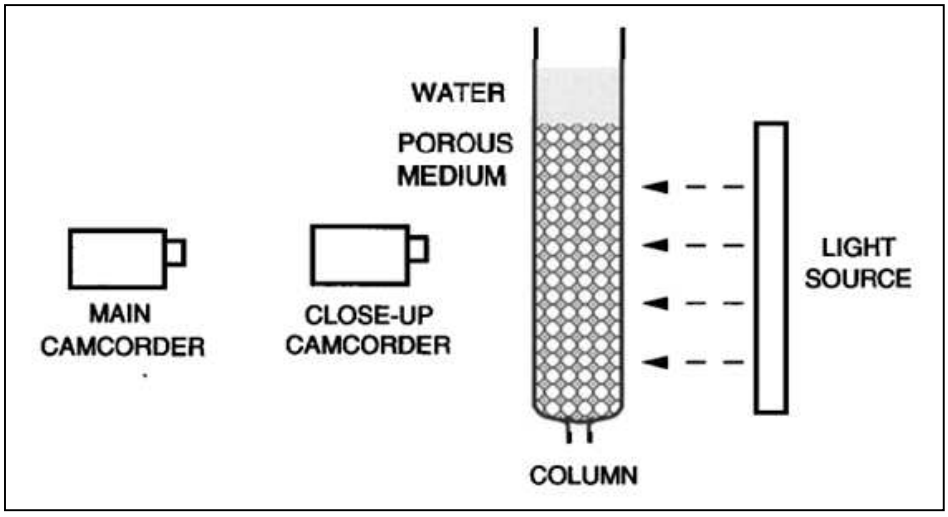

Figure 2-17: Schematic of the Experimental Apparatus from the Work of Roosevelt and Corapcioglu (1998)

Corapcioglu *et al.* (2004) developed an expression to estimate the rise velocity of an air bubble in porous media based on the experimental results of Roosevelt and Corapcioglu (1998). Their assumptions for the formulation were a stationary, homogeneous, isotropic porous medium fully saturated with water, and incompressible water and gas phases (although this assumption is hard to achieve). Considering a single bubble, pore level mechanisms such as snap-off and division were neglected. They also assumed that the bubble was completely surrounded by water, and the energy used to stretch the bubble through

the pore bodies was completely recovered upon compression through the pore throats. The force balance in the vertical direction was written as:

$$\sum F = F_b - F_d - F_{st} = \frac{4}{3}\,\pi\, R_b^3\, \rho_g \left(\frac{\partial u_b}{\partial t} + u_b \frac{\partial u_b}{\partial z}\right) \tag{2-35}$$

where F_b is the buoyancy force, F_{st} is the surface tension force, F_d is the drag force and R_b is the equivalent radius of a sphere with the a volume equal to that of a bubble. Corapcioglu *et al.* (2004) neglected the Basset force (also termed as Basset history force) resulting from the viscous effects generated by the acceleration of a particle relative to a fluid under the creeping flow conditions because of high bubble velocities. Basset force is described as the force due to the temporal delay in boundary layer development as the relative velocity of moving bodies in a fluid changes with time (Crowe *et al.*, 1998). The lift force on the bubble was also neglected due to the irrotational flow conditions. The expression for the buoyant force was given by:

$$F_b = \left(\rho_f - \rho_g\right) g\, \tfrac{4}{3}\, \pi\, R_b^3 \tag{2-36}$$

where ρ_f is the density of water.

The surface tension force was expressed in the vertical direction by:

$$F_{st} = 2\,\pi\, R'\, \sigma\, \sin\theta \tag{2-37}$$

where σ is the surface tension, θ is the contact angle assumed to be constant during the bubble motion and R' is the equivalent radius of a pore throat through which a bubble can pass in particular arrangement of grains as shown in Figure 2-18. Assuming equilibrium between the phases in porous media, θ is taken as 30º.

Using the empirically-based, modified Ergun equation, which incorporates both kinetic and viscous energy losses, to address the drag force, Corapcioglu *et al.* (2004) expressed the force balance (Equation 2-35) as:

$$\left(\rho_f - \rho_g\right) g \frac{4}{3}\pi R_b^3 - A\left[\frac{150\,\mu_b u_b (1-\emptyset)^2}{d_p^2\,\emptyset^3} + \frac{1.75\rho_g u_b^2 (1-\emptyset)}{d_p\,\emptyset^3}\right]\frac{4}{3}\pi R_b^3 \tag{2-38}$$

$$- 2\pi R'\sigma \sin\theta = A_d \rho_g \frac{4}{3}\pi R_b^3 \left(\frac{\partial u_b}{\partial t} + u_b \frac{\partial u_b}{\partial z}\right)$$

where μ_b is the bubble viscosity, ϕ is the porosity, d_p is the mean particle diameter, A is the correction factor that depends on the properties of porous media, and A_d is the additional mass term to account for the fact that a bubble takes an additional apparent mass as it creates a flow field upon acceleration, which increases its particular mass.

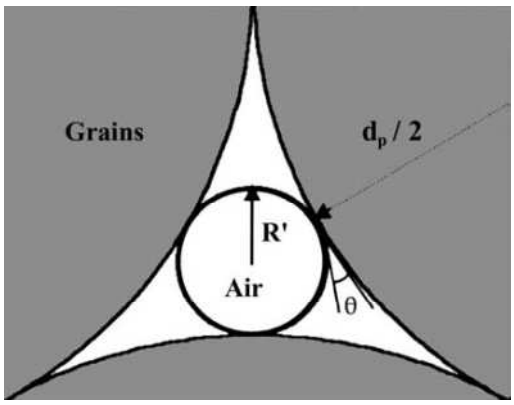

Figure 2-18: Schematic Diagram of a Bubble in a Porous Medium with Orthorhombic Packing Arrangement (Corapcioglu *et al*., 2004)

The terminal rise velocity of the bubble was obtained by finding the steady state solution of Equation 2-38 as given by:

$$u_b = \frac{\mu_b}{\rho_g}\frac{(1-\emptyset)}{d_p}\left[-42.86 \pm \sqrt{1836.74 - \frac{0.57}{A}\left(\frac{\rho_g\, d_p^3\, \emptyset^3}{\mu_b^2\,(1-\emptyset)^3}\right)\left(\frac{3}{2}\frac{R'}{R_b^3}\sigma\sin\theta - (\rho_f - \rho_g)g\right)}\right] \quad (2\text{-}39)$$

where the medium-specific correction factor A was calculated as 26.8 by matching the experimental data of Roosevelt and Corapcioglu (1998).

Smith (2005) raised some objections to the theoretical analysis of Corapcioglu *et al.* (2004). The first one was related to the surface tension force, defined by Equation 2-37 in their work. Smith (2005) explained that Equation 2-37 overestimates the surface tension force resisting the upward motion of the bubble as it accounts for only drainage effects at the leading meniscus and ignores the imbibition effects at the trailing meniscus. Another problem was found in the drag force expression based on the modified

Ergun equation. It was explained that the viscosity used in the drag force expression defined by Corapcioglu *et al.* (2004) should be the water viscosity instead of the bubble viscosity, because the gas viscosity is very low and the viscous effects within the bubble are negligible compared to the contribution of the displaced water in the viscous drag resistance. The last problem in the analysis of Corapcioglu *et al.* (2004) was related to their force balance. According to Smith (2005), the expression for surface tension force defined by Equation 2-37 is incorrect when the buoyancy force is expressed by Equation 2-36, because the surface tension force must be modified based on the bubble orientation, i.e. it must be multiplied by the number of interfaces in the vertical direction, which is not suggested by Equation 2-37.

Oldenburg and Lewicki (2006) applied the model of Corapcioglu *et al.* (2004) for incompressible bubbles to predict the rise velocity of CO_2 bubbles in porous media leaking from storage in deep geologic formations under the effect of buoyancy. Their results showed that the rise of CO_2 bubbles in saturated porous media is more likely to occur as channel flow rather than bubble flow. A maximum velocity of 30 cm/s was calculated for buoyancy-driven rise of CO_2 bubbles in surface water. However, the assumption of incompressibility for gas bubbles rising through deep saturated sediments may significantly affect the analysis of the behavior and biochemical production of the gas bubbles in porous environment (Amos and Mayer, 2006).

Cihan and Corapcioglu (2008) developed another model by combining Newton's second law of motion and the ideal gas law to analyze the effect of air compressibility on the bubble rise velocity in porous media. Their results showed a strong dependency of the rise velocity of a compressible air bubble on the depth at which the air phase was injected. The rise velocity of a bubble released from greater depths was slower than the velocity of a bubble with an equal volume released from shallower depths due to the larger drag force acting on the bubble resulting from the higher hydrostatic water pressure. Furthermore, the volume of air bubbles increased as pressure decreased with depth, as the bubbles migrated up through the porous medium. Cihan and Corapcioglu (2008) showed that the difference between the rise velocity of a compressible bubble and that of an incompressible one approaches zero as the bubble reaches the water table. The velocity of a compressible bubble did not exceed 18.8 cm/s in their work regardless of varying injection depth and the bubble volume.

Stark and Manga (2000) conducted a numerical study to simulate the flow of discrete bubbles through porous media using a network model. Their model consisted of a network of tubes through which the bubbly liquid was transported from one location in the reservoir to another due to an applied pressure gradient. In their simulation, Stark and Manga considered only the motion of discrete bubbles separated

from walls by a film of fluid. Thus, they ignored dynamics of the contact line and focused on the hydrodynamics of the flow assuming that the film is hydrodynamically stable because of the bubble motion. They calculated the fluid and bubble velocities in the tubes using the equations of Bretherton (1961) for bubble velocity and pressure drop across a bubble, as previously expressed in Equations 2-14 and 2-15. Although the equations of Bretherton (1961) apply for infinitely long bubbles, as discussed in §2.5.1, the speed of infinitely long bubbles is an adequate approximation for bubbles of finite lengths with volumes larger than 95% of the critical volume (Olbricht, 1996). The effective permeability of the network was defined as the ratio of the flux in the presence of bubbles to the flux in the absence of bubbles at same conditions, and was determined as a function of two dimensionless parameters, the capillary number and the volume fraction of bubbles. Stark and Manga (2000) found a critical value of capillary number equal to 8.6×10^{-3} at which the pressure drop across a bubble is equal to the pressure drop across the same length of the suspending fluid. It was also shown that above this critical capillary number, the effective permeability of the network increases with decreasing the volume fraction of bubbles due to dominant viscous forces in the system, while below this critical value, the effective permeability decreases with increasing the volume fraction due to dominant surface tension effects.

For the purpose of current study, an attempt is made to simulate the flow behavior of rising bubbles based on the code developed by Smith (2005). This is presented later in this thesis.

Chapter 3

Theory Development

Consider a porous medium with uniform pore geometry saturated with a liquid of density ρ_l and viscosity μ_l. The velocity of the liquid phase in a saturated porous medium for one-dimensional flows is governed by Darcy's law, as:

$$u_l = \frac{K}{\mu_l}\frac{\Delta P_l}{L} \tag{3-1}$$

where K is the absolute permeability of the medium and $\Delta P_l/L$ is the pressure gradient. Furthermore, the medium contains a gas bubble of length L_b, density ρ_g and viscosity μ_g (Figure 3-1).

For a trapped bubble, as shown in Figure 3-1, the total pressure difference across the gas bubble in a pore network with inclination/dip angle α_{dip} is given by:

$$\Delta P_b = \left(\rho_{\,l} - \rho_g\right) g\, L_b\, \sin\alpha_{dip} - \left(P_{c1} - P_{c2}\right) \tag{3-2}$$

where P_{c1} and P_{c2} are capillary pressures at the meniscuses of the bubble front and bubble tailing end, respectively.

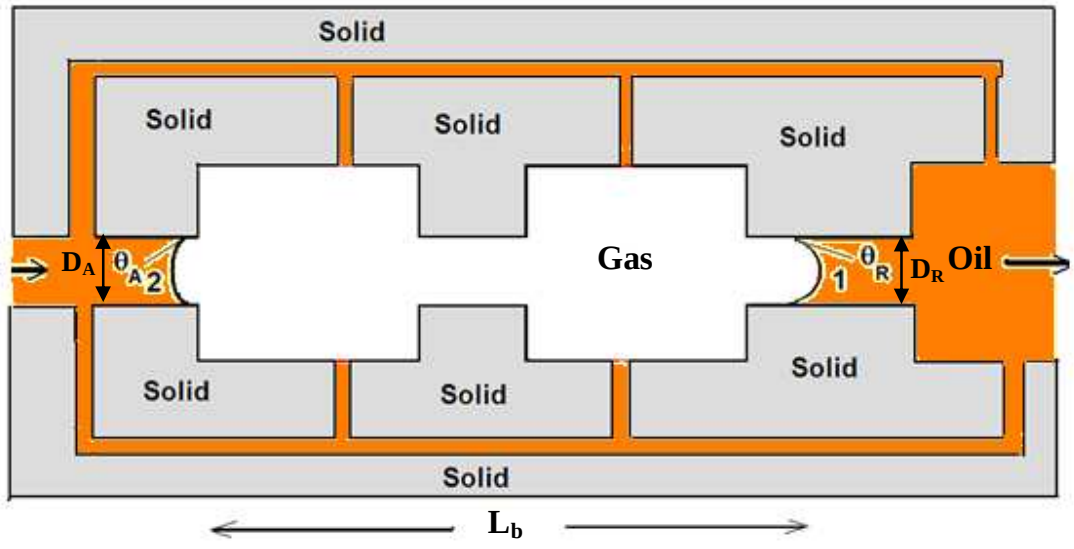

Figure 3-1: Schematic of an Air Bubble Surrounded by Oil in a Pore Network

It is assumed that the velocity of the bubble is equal to the velocity of the liquid phase at the gas/liquid interface (u_b=u_l). Thus, the pressure gradient in the liquid phase can be equated to the pressure drop across the gas bubble ($\Delta P_l = \Delta P_b$).

Furthermore, for bubble migration in a porous medium the liquid displaced by the motion of the bubble does not travel a particular distance as in the capillary tube, but rather, travels along a generally unknown route over a length termed the "effective length" L_{eff}. The effective length is a measure of the path length over which the liquid displaced by the bubble front must travel to reach the bubble tail. L_{eff} varies with the structure of the porous medium and the bubble length. From the aforementioned assumption and definition, the pressure gradient term in Equation 3-1 is expressed as:

$$\frac{\Delta P_l}{L_{eff}} = \frac{\Delta P_b}{L_{eff}} \tag{3-3}$$

Substituting Equations 3-2 and 3-3 in Equation 3-1, the velocity of a moving gas bubble in a liquid saturated porous medium is given by:

$$u_b = \frac{K}{\mu_l \, L_{eff}} \left[\Delta\rho \; g \; L_b \sin\alpha_{dip} - (P_{c1} - P_{c2})\right] \tag{3-4}$$

Rearranging Equation 3-3 yields:

$$u_b = \frac{K \; \Delta\rho \; g \;\; \sin\alpha_{dip}}{\mu_l} \left(\frac{L_b}{L_{eff}}\right) - \frac{K \; (P_{c1} - P_{c2})}{\mu \; L_{eff}} \tag{3-5}$$

In the calculation of the capillary pressures P_{c1} and P_{c2} at the front and rear of a moving bubble in a porous medium, it must be noted that, unlike bubble rise in a capillary tube, the pore diameters in which the advancing and receding menisci are formed, D_A and D_R in Figure 3-1, are not necessarily the same. Accordingly, Equation 3-4 can be rewritten as;

$$u_b = \frac{K \; \Delta\rho \; g \;\; \sin\alpha_{dip}}{\mu_l} \left(\frac{L_b}{L_{eff}}\right) - \frac{K}{\mu \; L_{eff}} \left[4\sigma \left(\frac{\cos\theta_R}{D_R} - \frac{\cos\theta_A}{D_A}\right)\right] \tag{3-6}$$

where σ is the interfacial tension between the liquid and gas. Figure 3-2 shows two different interface configurations in a network of pore bodies and pore throats for a gas bubble rising upwards. Figure 3-2 (a) shows the configuration of minimum driving force, in that the receding meniscus is located in a pore throat and thus produces maximum resistance to upward motion of the bubble, while the advancing interface is located in a pore body and produces minimum force in the direction of the bubble motion. On

the other hand, Figure 3-2 (b) represents a condition in that maximum driving force for the bubble motion is produced. The receding meniscus is located in a pore body and thus produces minimum capillary pressure to upward migration of the bubble, while the advancing interface is located in a pore throat, producing maximum force pushing the bubble upwards. In configuration (a), surface tension forces oppose buoyancy forces, while in configuration (b), they act in the same direction as buoyancy forces and facilitate upward bubble motion.

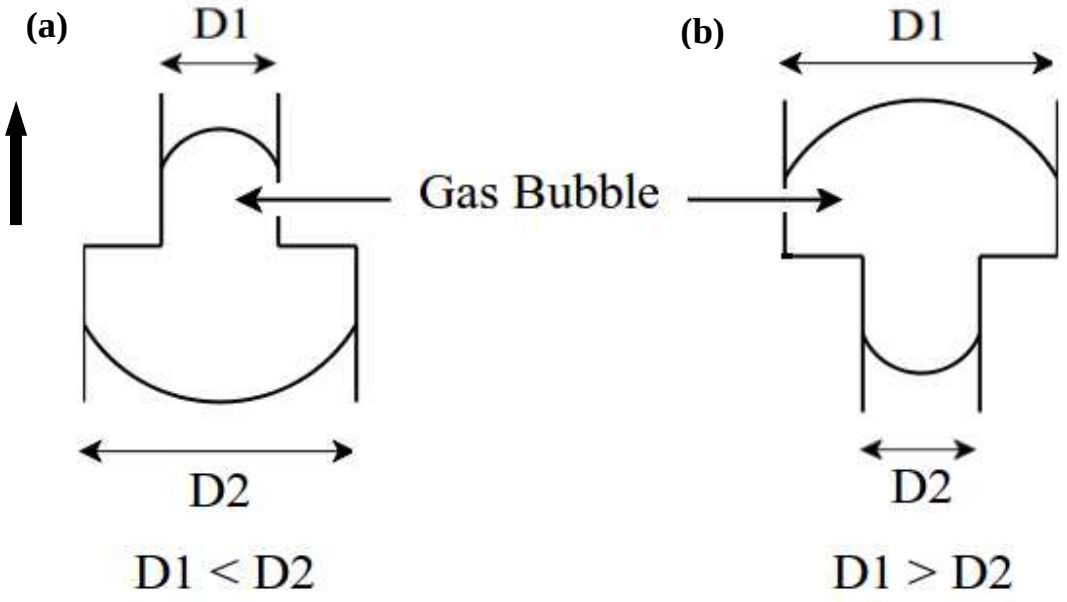

Figure 3-2: Configurations for the Interface Position Leading to (a) Minimum and (b) Maximum Capillary Driving Force during Bubble Motion (Edited after Smith, 2005)

In fact, a bubble moving in a porous medium never reaches a steady-state condition since the positions of the advancing and receding interfaces and, consequently, the driving forces for bubble motion are constantly changing. However, the bubble can achieve a pseudo-steady state condition, where the velocity varies periodically around an average value (Smith, 2005).

To validate Equation 3-6, many experiments were conducted in this work. Numerical simulation for bubble migration in a pore network was also performed to verify Equation 3-6. The bubble velocity u_b density difference $\Delta\rho$ and inclination/dip angle α_{dip} are measurable parameters. Gravity acceleration, g, is also known; thus, permeability of the medium, K, and effective length, L_{eff}, are the only unknown parameters in Equation 3-6. First, it will be assumed that effective length L_{eff} is equal to the bubble length,

L_b, and K will be calculated. Then, based on the value of the calculated permeability, the effective length will be calculated for various bubble lengths.

Chapter 4

Bubble Migration Experiments in Micromodels

4.1 Average Rise Velocity Experiments

4.1.1 Experimental Method and Materials

Experiments were conducted in a water-wet micromodel with a pore network pattern etched into the glass to represent an actual porous medium in two dimensions. The micromodel denoted Micromodel MP-7 has a series of channels with relatively equal sizes interconnected by smaller sized pore throats on either side of the central channel. The fluids were injected into the pore network through the access holes drilled at both ends of the micromodel. Figure 4-1 shows the microstructure pattern of the Micromodel MP-7 in which the liquid displaced from the main channel can travel along multi side channels during bubble migration. A photograph of the pore geometry of this model taken using a BAUSCH & LOMB StereoZoom7 microscope is shown in Figure 4-2. The network pattern used in this work was 9 pores wide by 100 pores long. The characteristics of the micromodel are listed in Table 4-1. Micromodel characterization will be discussed in detail in §4.1.2.

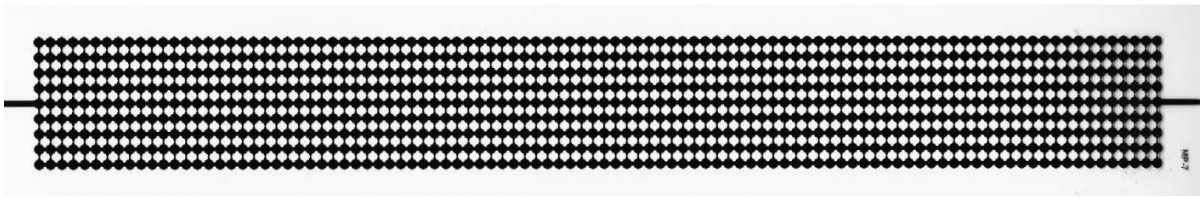

Figure 4-1: Pattern Etched in the Micromodel MP-7

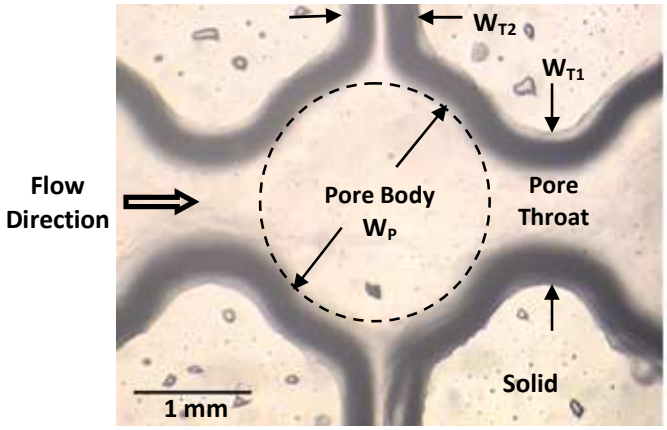

Figure 4-2: Photograph of the Pore Geometry in Micromodel MP-7

Table 4-1: Characteristics of the Micromodel MP-7

Length (mm)	Width (mm)	Pore-to-Pore Distance (mm)	Pore Width (W_P) (mm)	Throat Width (W_{T1}) (mm)
278	**32**	**3±0.1**	**2.0±0.1**	**1.2±0.1**

Fluids used as the wetting phase to saturate the micromodel were kerosene, Soltrol 170, and White Oil with red dye added to it. These fluids are relatively non-volatile so that they should not influence bubble size due to vaporization. To determine the density of the fluids, the weight of a clean and dry 50 ml volumetric flask was measured using a VICON ACCULAB digital scale (accuracy: 0.005 g). A conventional thermometer was used to measure the ambient temperature in the lab. The volumetric flask was filled with the test liquid up to the marked line and the traces of the liquid deposit on the flask were removed using a cotton swab to ensure the accuracy of the measurement. The filled flask was then weighed and the mass of the liquid was calculated. The density was determined knowing the mass and volume of the liquid.

The viscosity of the liquids used was measured by using CANNON-FENSKE Routine glass viscometers in a constant temperature bath. The efflux time of the free downward flow of the liquid between the two marked lines was measured once it passed the marks. The kinematic viscosity (μ/ρ) was calculated by multiplying the efflux time in seconds by the viscometer constant. Two sizes of the viscometer were used depending on the viscosity range, size 50 for Kerosene and Soltrol 170 and size 100 for White Oil. Kerosene and Soltrol 170 have relatively similar viscosities, but the viscosity of White Oil

was about 12 times more than the other two. A picture of the viscometer containing White Oil (dyed red) inside the constant temperature bath is shown in Figure 4-3. Surface tension of the liquids was measured by a Video Contact Angle System (VCA 2500XE) in an open atmosphere. The physical properties of the test fluids at 25 ºC are given in Table 4-2.

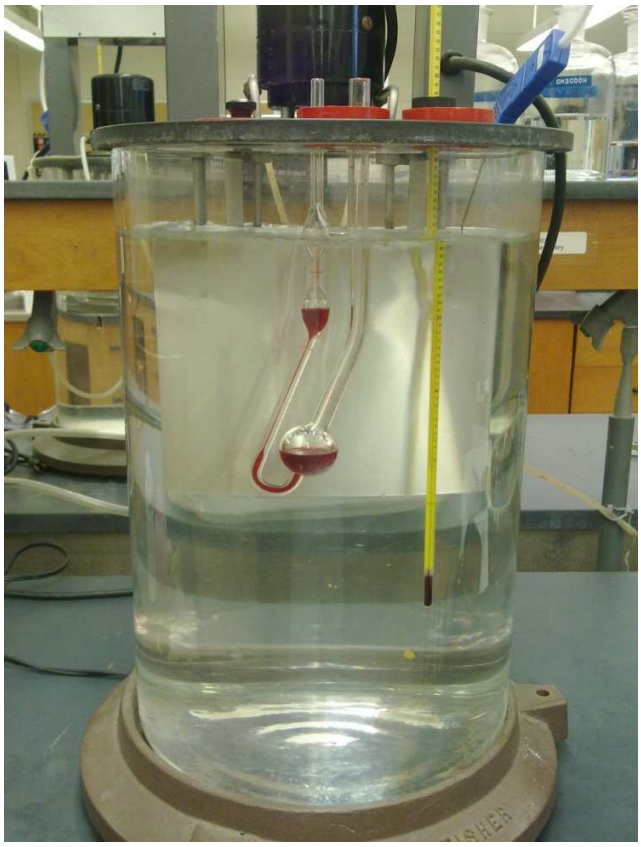

Figure 4-3: Photograph of the Cannon Viscometer Containing Dyed White Oil inside the Constant Temperature Bath

Table 4-2: Physical Properties of the Test Fluids Used in Micromodel Experiments at 25ºC

Property \ Fluid	Kerosene	Soltrol 170	White Oil
Density (g/cm^3)	0.782	0.736	0.844
Viscosity (mPa.s)	0.95	1.0	12
Surface Tension (mN/m)	24.6	21.3	27.9

The micromodel was first washed with acetone and dried with clean, compressed air. Then, it was saturated with the test liquid by using a glass syringe and injecting the fluid through a fitting attached to either of the two access ports. An air bubble was created in the following way: The micromodel is tilted upwards slightly from one end, which imposes the drainage of liquid on the other-end of the micromodel. Thus, air enters into the model through the access hole at the elevated end and a very small volume of the liquid is drained through the opposite end port. The micromodel structure was designed such that the central passageway was a bit larger than the pore throats connecting the central passage to the side passages; thus, the air invaded preferentially into the central row of pore bodies and pore throats. Once a bubble with an arbitrary length was formed, the model was set in a horizontal position and both access ports were closed with small pieces of septum to ensure an air-tight seal and prevent further drainage of the liquid. After this, the model was placed and fixed on the top flat surface of the experimental set-up, designed to allow different inclinations of the model. To change the inclination angle of the model gently, an EBERBACH cathetometer was used with a rod shape as a holder. A metering tape was attached to the bottom surface of the set-up for easy measurement of the horizontal component of the inclination angle for the system. Figure 4-4 shows a picture of the experimental apparatus.

Before starting an experiment, the micromodel was oriented such that the bubble was positioned near one end immediately behind the pre-start line. The length of the bubble was measured accurately when the model was rested horizontally. The pre-start line was marked a small distance (1.2 cm) behind the start line to allow bubble to begin moving before timing was started and to reach a steady-state velocity. Results of Corapcioglu *et al.* (2004) showed that air bubbles migrating upwards through a porous medium reach their equilibrium state after traveling only a very short distance. The opposite end of the model was then elevated gently by the cathetometer by an unknown angle α with respect to its horizontal position causing the bubble to start moving under the action of buoyancy. The ambient temperature was measured using a mercury thermometer in order to correct for any possible changes in temperature. The critical inclination angle α_{cr} of the model, hereafter referred to as dip angle, at which the air bubble started to move was recorded. The angle of inclination was calculated by measuring both horizontal and vertical sides of the right triangle. For each dip angle above the critical angle ($\alpha_{dip} < \alpha_{cr} < 90^o$), the time of the bubble displacement over a set distance of 10 cm was recorded using a stopwatch once it passed the start line. Both bubble length and the dip angle for the micromodel were altered during experiments for each test fluid; however, the measurements were made by varying the dip angles and measuring the velocities for a given bubble length. This procedure has the advantage of enabling several data points to be collected without changing the bubble length. In this work, the angles of inclination were varied within the range of

3 to 38º. Two runs of each experiment were performed to ensure accurate measurements and repeatability. The data collected for both runs were close enough so that their average value was reported as the measured bubble velocity. The bubble migration experiments were performed with different bubble lengths and liquids. The data collected are given in Table 4-3.

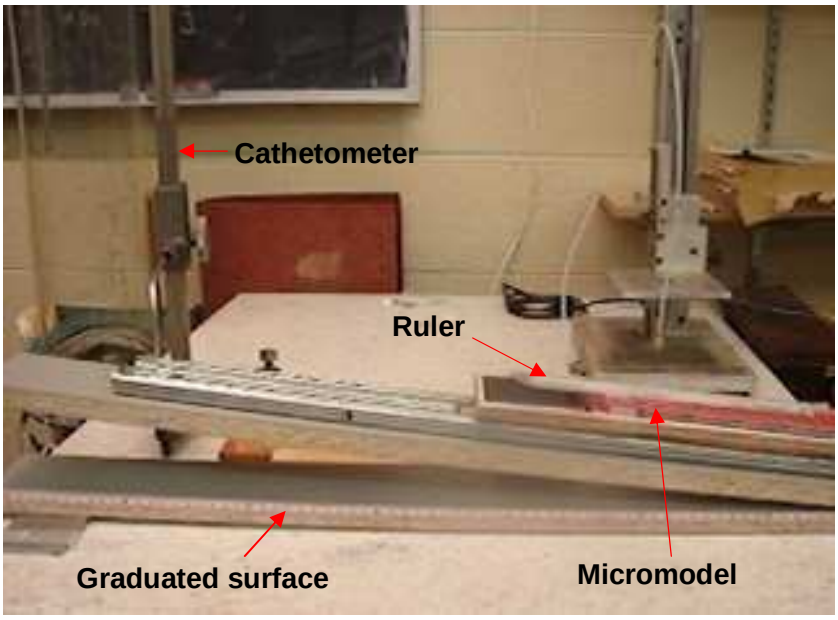

Figure 4-4: Photograph of the Experimental Apparatus for Bubble Migration in Micromodel

Table 4-3: Data Collected for Rise Velocity of Bubbles with Different Lengths at $\alpha_{dip} = 10^{o}$

	Velocity (cm/s)		
Bubble Length (mm)	**Kerosene**	**Soltrol 170**	**White Oil**
14	**0.66**	**0.81**	**-**
19	**0.98**	**0.93**	**-**
25	**1.29**	**1.22**	**-**
31	**1.65**	**1.59**	**0.10**
36	**1.92**	**1.81**	**0.14**
42	**2.18**	**2.16**	**0.16**
47	**2.29**	**2.34**	**0.17**
53	**-**	**2.47**	**-**
55	**-**	**-**	**0.21**

4.1.2 Micromodel Characterization

Micromodel MP-7 was characterized for its pore structure information to predict the permeability of the model and to analyze the data. Pore widths W_P and throat width, W_T, were directly measured using a microscope to yield data shown in Table 4-1. Widths of several pores and throats were measured randomly and the average value was reported as the pore width and throat width of the micromodel. Furthermore, drainage and imbibition capillary height tests were performed to verify the values of capillary pressure obtained for the micromodel and calculate the depth of etching for pores and throats. In drainage capillary height tests, a tube filled with the wetting liquid was connected to the liquid-saturated micromodel at one end and placed inside a sufficiently large beaker full of the liquid at the other end. The micromodel was then held in a vertical position and lifted up to cause the liquid to drain under gravity. The height of the model was gradually increased above the beaker and the heights of new capillary interfaces established in the model were recorded after allowing the system some time to equilibrate. The drainage capillary pressure $P_{c,dr}$ at each elevation was calculated from the difference between the lowest height recorded for the interface in the model and the level of the liquid in the beaker by:

$$P_{c,dr} = h_{c,dr}\, \rho\, g \tag{4-1}$$

where ρ is the liquid density. The same procedure was repeated for imbibition capillary height measurements except that the vertically positioned micromodel was lowered to cause the liquid to push the air upwards in the model. The heights of the newly established capillary interfaces were measured and the imbibition capillary pressure of the model $P_{c,imb}$ was computed from the difference of heights between the highest interface level recorded during the test and the level of the liquid in the beaker, similar to Equation 4-1 i.e.,

$$P_{c,ibm} = h_{c,imb}\, \rho\, g \tag{4-2}$$

From the measurements of drainage and imbibition capillary pressures, the depth of pores and throats of the micromodel were estimated assuming $\theta_A = 0^o$ from the relations (Lenormand *et al.* 1983, Ioannidis *et al.* 1991):

$$P_{c,dr} = 2\sigma \left(\frac{1}{D_T} + \frac{1}{W_T}\right) \tag{4-3}$$

$$P_{c,imb} = 2\sigma \left(\frac{1}{D_P} + \frac{1}{W_P}\right) \tag{4-4}$$

where σ is the surface tension of the liquid used for the capillary height tests. D_P and D_T are depths of pores and throats, respectively.

To obtain information about the geometry of the pore network in the Micromodel MP-7, the experimental technique Constant Rate Air Injection (CRAI) Porosimetry first introduced by Smith *et al.* (2005) was used to measure the breakthrough capillary pressure of the model. The experimental set-up consisted of a constant rate displacement syringe pump, a pressure transducer and the glass micromodel connected at a T-joint. A schematic of the experimental apparatus is shown in Figure 4-5. The tubing between the injection pump and the pressure transducer was completely filled with water to have the pressure response only at the air-filled part of the tubing between the T-connection and the test model. The micromodel was placed in a horizontal position and the tubing was kept at a constant elevation with the transducer to prevent hydrostatic pressure effects. Several steady injection flow rates were selected and the data transferred from the pressure transducer were recorded using a data acquisition system.

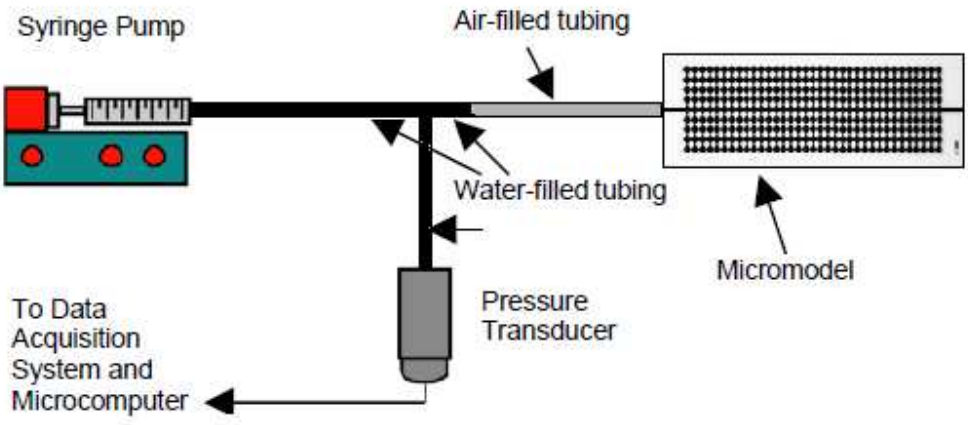

Figure 4-5: Experimental Set-up for Constant Rate Air Injection Tests (after Smith *et al.*, 2005)

The results for a low injection rate of 0.518 ml/hr are presented in Figure 4-6 as a plot of capillary pressure versus time. In this plot, maxima represent capillary pressures of pore throats and minima represent those of pore bodies. As seen, the pore throats throughout the model have similar capillary pressures required for invasion indicating that an almost uniform throat size distribution in the micromodel. This verifies the assumption of uniform geometry within the Micromodel MP-7 made in the analysis of results presented in this thesis.

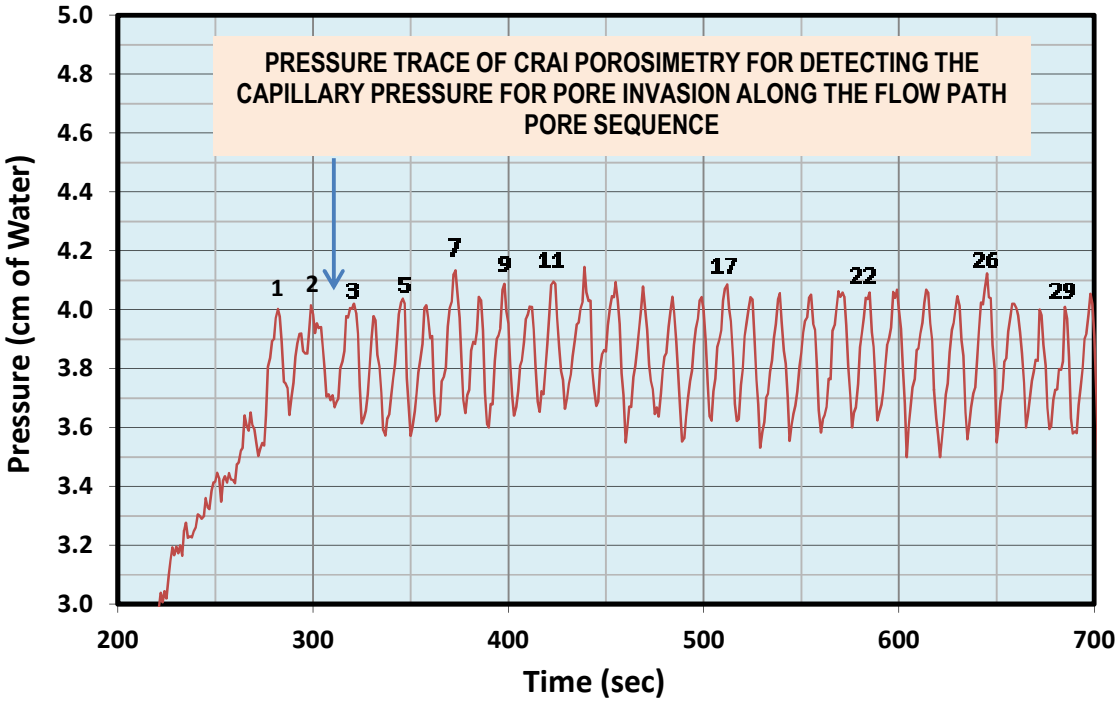

Figure 4-6: Capillary Pressure versus Time for a CRAI Porosimetry Test with Q_w = 0.518 mL/hr (V_{pore} ≈ 0.002 mL)

4.1.3 Results and Discussion

Figure 4-7 and Figure 4-8 show the bubble velocity as a function of the sin α_{dip} for different bubble lengths in the presence of kerosene and White Oil, respectively. The bubble velocity shows a linear trend with Sin α_{dip} ; the larger the dip angle, the higher is the velocity of the bubble, due to an increase in the pressure gradient. This was expected from Equation 3-6, restated here for convenience:

$$u_b = \frac{K\,\Delta\rho\; g\;\sin\alpha_{dip}}{\mu_l}\left(\frac{L_b}{L_{eff}}\right) - \frac{K}{\mu\, L_{eff}}\left[4\sigma\left(\frac{\cos\theta_R}{D_R} - \frac{\cos\theta_A}{D_A}\right)\right] \qquad (3\text{-}6)$$

The slope of the trendlines for $u_b = f\,(Sin\ \alpha_{dip})$ is equal to $[(K\Delta\rho g/\mu)(L_b/L_{eff})]$. Thus, as seen in Figure 4-7 and Figure 4-8, for a given fluid (constant ρ and μ), the slopes increase with increasing (L_b/L_{eff}), where L_{eff} is the effective distance over which the fluid displaced by the upward motion of the bubble travels from the bubble front to reach the bubble tail. This indicates that the experimental data agree well with Equation 3-6.

Table 4-4 lists the values of the micromodel permeability obtained with various bubble lengths and different test liquids assuming $L_b = L_{eff}$. For all wetting fluids, the calculated permeability of the system increases with increasing bubble length. According to Equation 3-6, for increased bubble lengths, the second term decreases leading to a rise in bubble velocity and the calculated permeability. The variation of the calculated permeability of the micromodel with the bubble length for the three liquids is presented in Figure 4-9. It is seen that calculated permeability increases with increasing bubble length in all test liquids. The variability between different fluids is seen in Table 4-4.

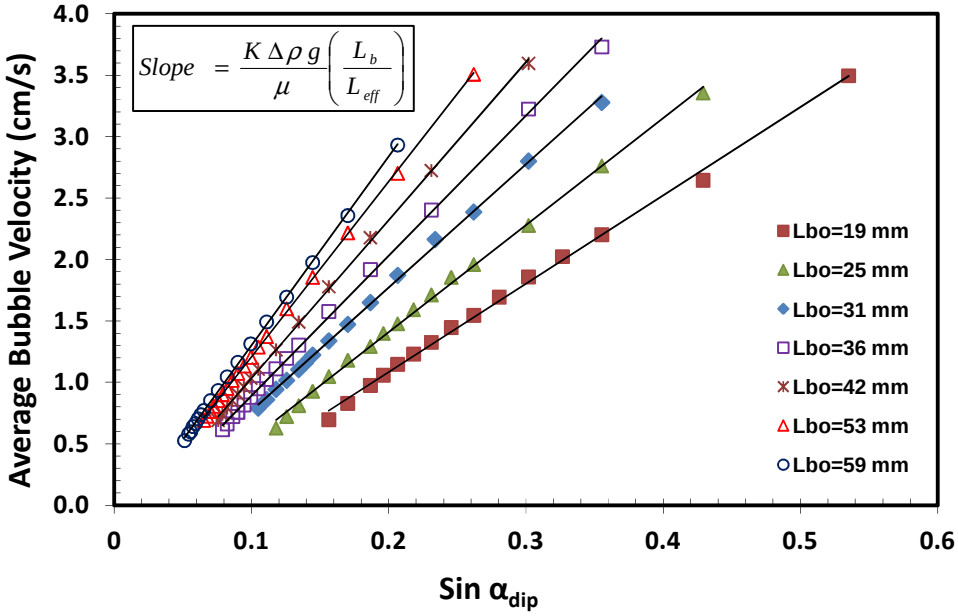

Figure 4-7: Bubble Velocity versus the Sin α_{dip} for Different Bubble Lengths for Kerosene

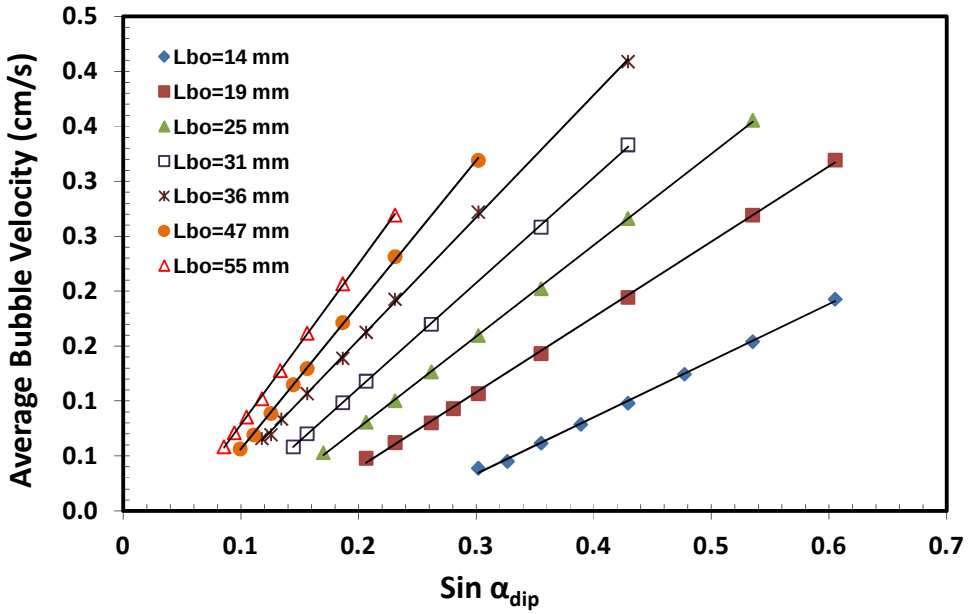

Figure 4-8: Bubble Velocity versus the Sin α_{dip} for Various Bubble Lengths for White Oil

Table 4-4: Calculated Permeability for Micromodel MP-7 for Different Bubble Lengths and Liquids when Assuming $L_{bo} = L_{eff}$

Kerosene		Soltrol 170		White Oil	
L_{bo} (cm)	K_{cal} (cm^2)	L_{bo} (cm)	K_{cal} (cm^2)	L_{bo} (cm)	K_{cal} (cm^2)
1.4	7.3115×10^{-5}	1.4	7.6810×10^{-5}	1.4	7.6459×10^{-5}
1.9	9.0759×10^{-5}	1.9	1.0415×10^{-4}	1.9	9.9254×10^{-5}
2.5	1.0978×10^{-4}	2.5	1.3396×10^{-4}	2.5	1.2101×10^{-4}
3.1	1.2624×10^{-4}	3.1	1.5301×10^{-4}	3.1	1.4146×10^{-4}
3.6	1.4259×10^{-4}	3.6	1.6648×10^{-4}	3.6	1.4872×10^{-4}
4.2	1.6045×10^{-4}	4.2	1.8847×10-4	4.2	1.7884×10^{-4}
4.7	1.6470×10^{-4}	4.7	1.9449×10^{-4}	4.7	1.8351×10^{-4}
5.3	1.7781×10^{-4}	5.3	2.1442×10^{-4}	5.5	1.9993×10^{-4}

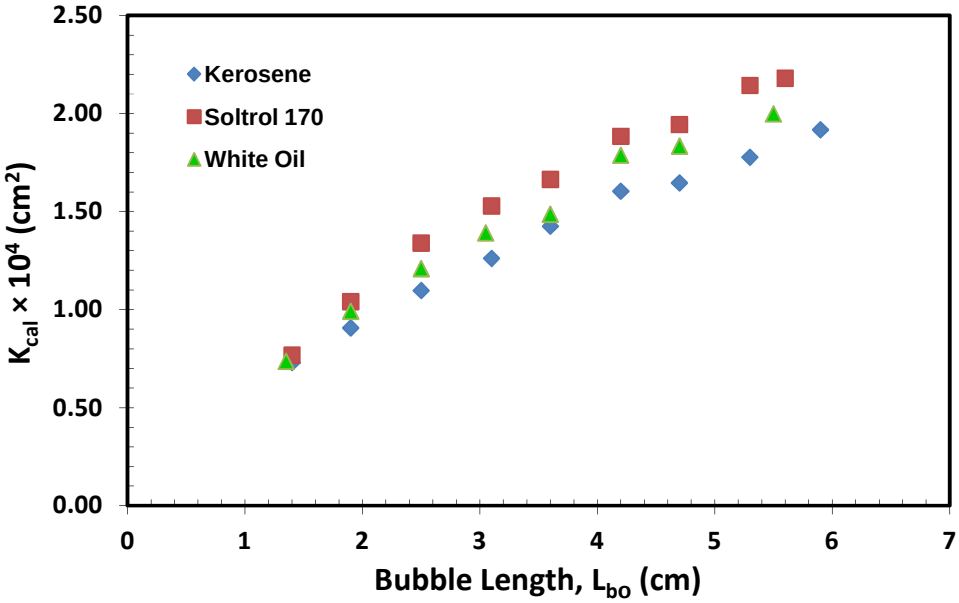

Figure 4-9: Variations of Calculated Permeability with Static Bubble Length for Micromodel MP-7 Assuming $L_{bo} = L_{eff}$

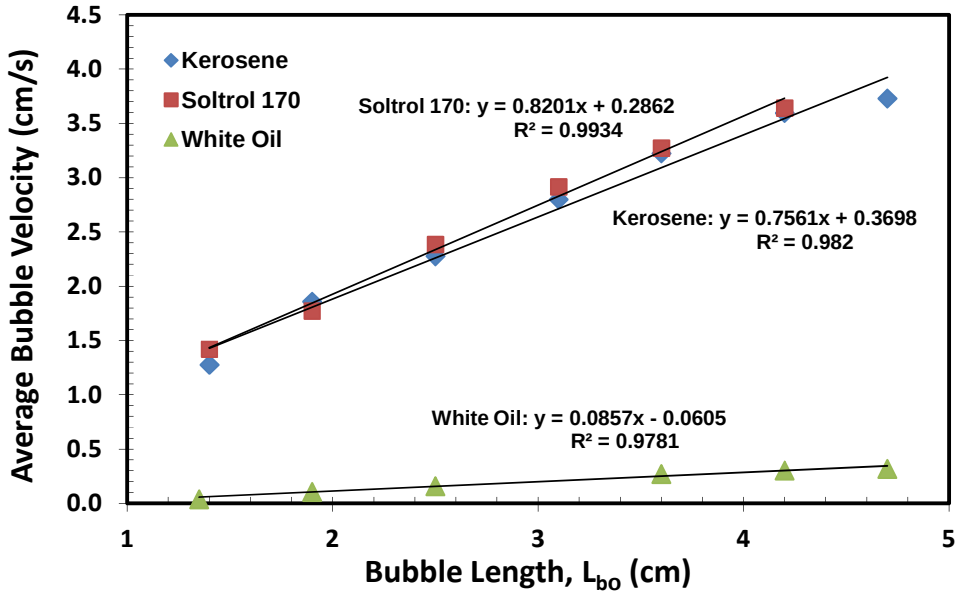

Figure 4-10: Average Bubble Rise Velocity versus Bubble Length for $\alpha_{dip} = 18^o$

Figure 4-10 shows the average bubble rise velocity versus the static bubble length, L_{bo}, based on the measurements made at $\alpha_{dip}= 18^o$ for three different liquids. The average bubble velocity varies linearly with the bubble length for most of the data range excluding the few points at larger bubble lengths. Roosevelt and Corapcioglu (1998) showed that the bubble rise velocity was nearly independent of bubble volume (which is a function of the bubble length) in the data range of their study. This was later confirmed by the theoretical model of Corapcioglu *et al.* (2004) when the bubble volume is larger than a critical value. However, our data showed that our data can be linear dependent on length with a high correlation coefficient (R^2=0.98). As expected from the variation of the calculated permeability with the bubble size, the average rise velocity of bubble increases with increasing the bubble length.

Figure 4-11 shows the dependence of average bubble velocity on the gravitational force. The bubble velocity increases linearly with rising the gravity force. Based on Equation 3-4, calculated permeability of the porous medium can be determined from the slope as follows:

$$K_{cal} = Slope \cdot \mu \cdot \left(\frac{L_{eff}}{L_b}\right) \tag{4-5}$$

where "Slope" is the slope of trendline of $u_b=f\ (\Delta\rho\ g\ sin\ \alpha_{dip})$ *data*. The values of the calculated permeability (assuming that L_{eff}/L_b = 1) and the slope of the trendlines in Figure 4-11 for various bubble lengths for Soltrol 170 are listed in Table 4-5. It was found that the slope and, consequently, calculated permeability increased with increasing bubble length. The observed changes suggest the existence of an effective bubble length L_{eff} that is responsible for the flow around the bubble during its upward motion.

Assuming that the micromodel permeability is constant, the values of L_{eff} were calculated from Equation 4-5. The results show that L_{eff} does not change significantly as L_b increases. Figure 4-12 shows dependence of (L_{bo}/L_{eff}) on L_{bo} . As seen, (L_{bo}/L_{eff}) is a linear function of bubble length. Effective length is also a function of medium permeability, pore geometry and connectivity, and also the presence/absence of other bodies in the vicinity of bubble (Smith, 2005). Figure 4-13 illustrates that the effective length for viscous pressure drop in the liquid displaced by the gas bubble is increasing gradually with bubble length.

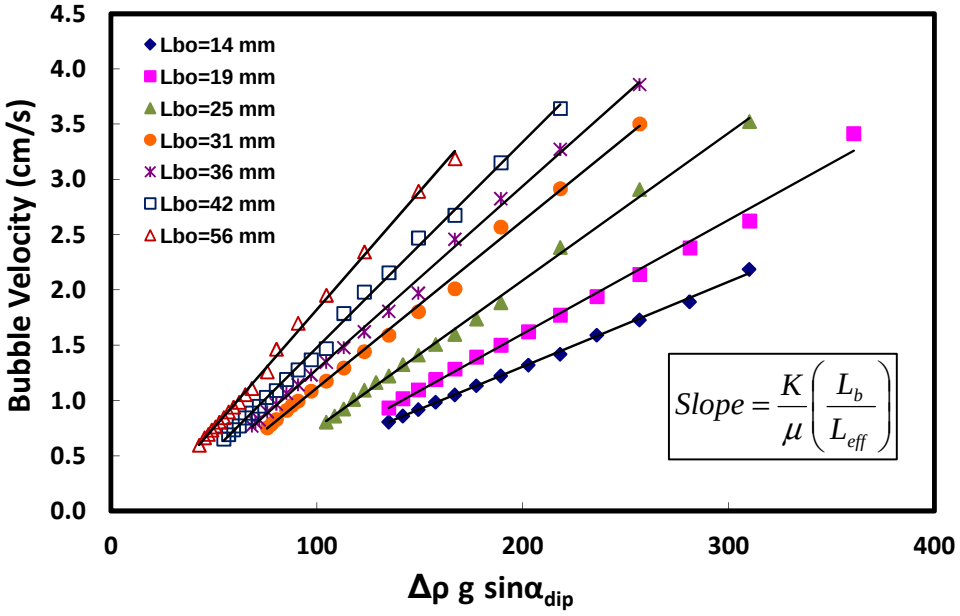

Figure 4-11: Variations of Bubble Velocity with the Gravity Force for Soltrol 170

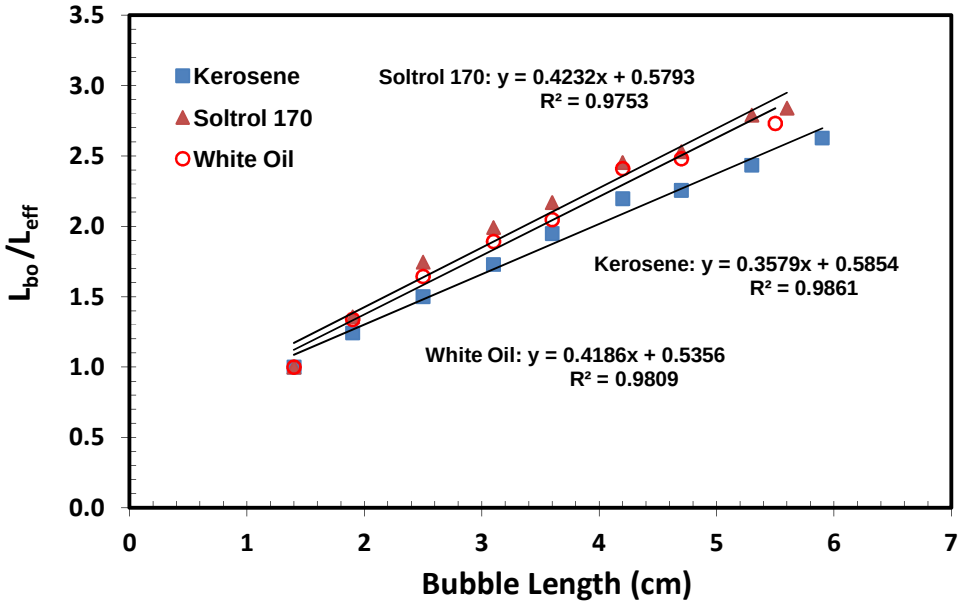

Figure 4-12: Calculated Ratio (L_{bo}/L_{eff}) versus Bubble Length for Different Liquids

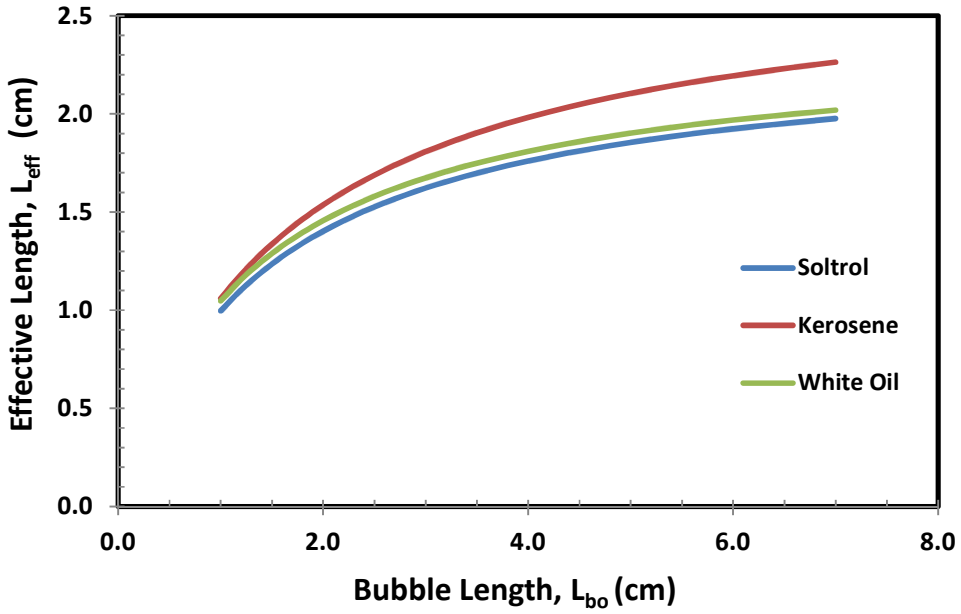

Figure 4-13: Effective Length versus the Bubble Length for Different Liquids

Table 4-5: Effect of Bubble Length on Calculated Permeability for Soltrol 170

L_{bo} (cm)	1.4	1.9	2.5	3.1	3.6	4.2	5.6
$K_{cal} \times 10^4$ (cm^2)	0.768	1.042	1.340	1.529	1.665	1.883	2.180
Slope	0.0077	0.0103	0.0133	0.0151	0.0166	0.0186	0.0214
L_{eff} (cm)	1.40	1.40	1.43	1.56	1.66	1.71	1.97

4.2 Visualization Experiments of Bubble Migration in Pore Network

4.2.1 Experimental Procedure

Visualization experiments for bubble migration in the micromodel were conducted by a procedure very similar to that described in§4.1.1, with the additional step of recording the bubble motion through the pore network by a SONY Cyber-shot digital camera with 12x optical zoom. Micromodel MP-7 was first washed, dried completely and then saturated with the wetting liquid. Only White Oil dyed red was used as the test fluid for visualization experiments because its viscosity is about 12 times higher than Kerosene and Soltrol 170. Only in this case was the velocity of bubble migration in the micromodel within the range that could be accurately measured with our digital camera. To create an air bubble, the same method was that used previously in that the model is elevated slightly from one end causing the drainage condition on the model and allowing air to come into the model through the access hole at the same end. White Oil exits from the opposite end port and a bubble is formed in the central channel because of its larger dimension relative to the small size throats connecting the central passageway to the neighboring channels. When the desired bubble length is achieved, the micromodel is set horizontally and both end access holes are closed with a small septum (play dough). This provides sealing for the model and prevents air from further coming in and the liquid from draining out.

Before an experiment began, the micromodel was positioned sothat the air bubble was located behind the pre-start line. The model was fixed in a stable place on the set-up and the bubble length was recorded. The camera was held by a laboratory camera stand in front of the set-up with that the lens of the camera facing the micromodel in a parallel position. A schematic of the set-up configuration is shown in Figure 4-14. The angle of inclination was altered gently using a cathetometer until the bubble started to move. This angle was recorded as the critical angle α_{cr} .When a dip angle for the model ($\alpha_{dip} < \alpha_{cr} < 90^o$) was set, recording by the camera was initiated immediately and timing was started once the bubble passed the marked start line. Similar to the previous set of experiments, the bubble was given a short time to accelerate and reach a steady-state velocity before its traverse over the set distance was timed. Once the front of the bubbles crossed the end line, timing was stopped, but the video recording was continued until the tail of the bubble also passed the end line. Again, in this set of experiments, both bubble length and the inclination angle of the micromodel were varied. Two repeated runs were made for each experiment for more accuracy. The data measured in both runs were close enough so that their average value was calculated and reported as the measured velocity.

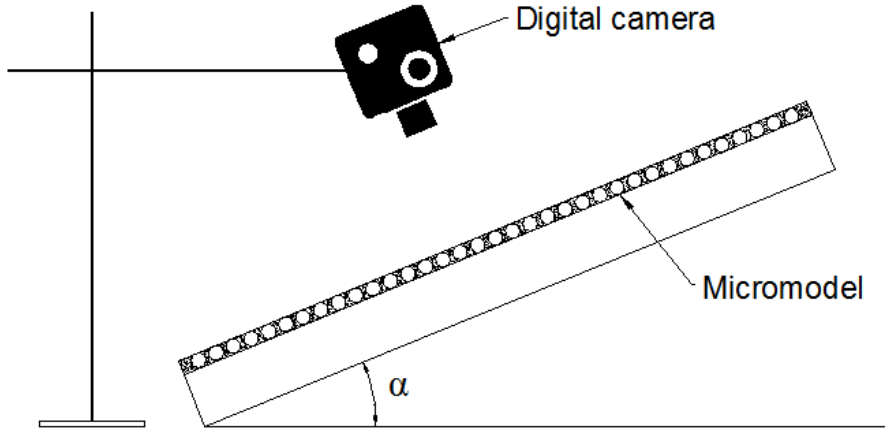

Figure 4-14: Schematic of the experimental Set-up for Bubble Migration Experiments in Micromodel

The videos were reviewed on the computer and the analysis was performed using the PowerDVD 11 software. To obtain images of an air bubble migrating through the micromodel, the frames were captured from the video at the same time intervals of 1, 2, or 3 seconds and magnified up to 5 times. The image analysis was performed and from that, the time of the bubble traverse over the set distance, exact locations of the bubble front and bubble tail ends at different times during motion, the dynamic length of the bubbles, and the instantaneous bubble velocities were determined.

4.2.2 Results and Discussion

Figure 4-15 andFigure 4-16 show the variations of the bubble velocity versus time and the bubble front position for White Oil. The measurements were made for a bubble with the static length of 1.35 cm over 3-second time intervals and a bubble with the static length of 2.5 cm over 1-second time intervals, both at the same dip angle of 25º. Changes in velocity profile as a function of time and bubble position illustrate that bubbles do not migrate at a constant velocity through a porous medium. The measured velocity for moving bubbles is significantly higher at some points (e.g. at X_F~1.8 cm) and reaches its minimum somewhere close to the end of the traverse distance (i.e. X_F~9.5 cm) for all experiments, which suggests some non-uniformity in the pore sizes and depth of etching throughout the model. Therefore, some pore throats may be larger and others smaller relative to the neighbors through which the air bubble invasion is easier or more difficult, respectively. Figure 4-15 and Figure 4-16 show that the local bubble velocity

changes with bubble length for a given dip angle. As shown in Figure 4-15, the bubble migration velocity can vary by a factor of 2.5 over the length of model, while Figure 4-16 indicates that the local velocity changes by factor of 3 for a larger bubble. However, the maximum and minimum velocities appear to occur at the same distances of 1.8 and 9.5 cm from the starting point.

Figure 4-17 shows variations of the bubble front and bubble tail positions versus time for a bubble with the static length of 1.9 cm and α_{dip}=32°. As evident, both the bubble front and bubble tail positions vary linearly with very high correlation coefficients (R^2=0.99). The difference between the positions of the bubble front and the bubble tail during the bubble migration represents the dynamic bubble length L_b *dynamic*.

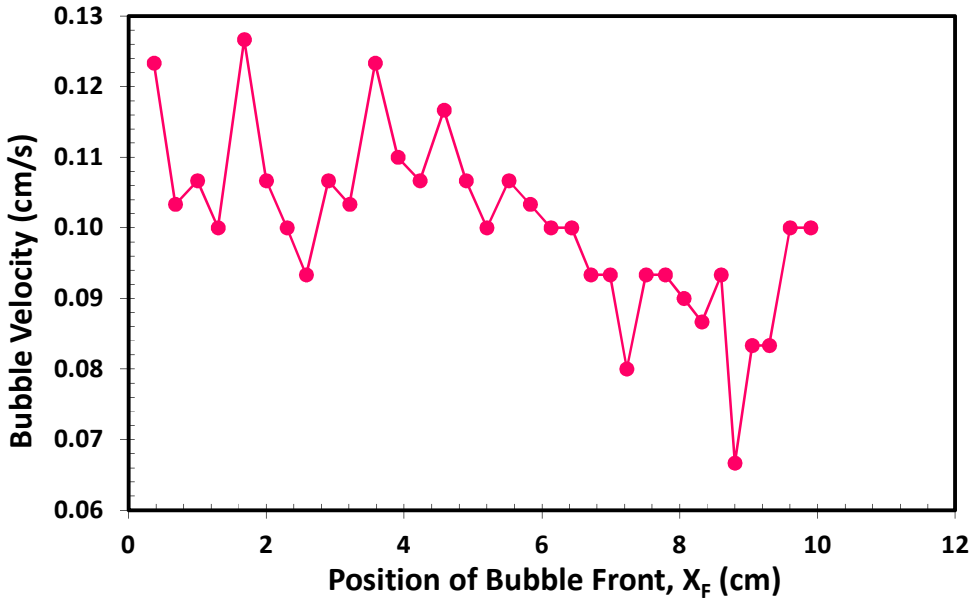

Figure 4-15: Variations of Bubble Velocity versus Bubble Front Position for L_{bo} = 1.4 cm and α_{dip} = 25° for White Oil

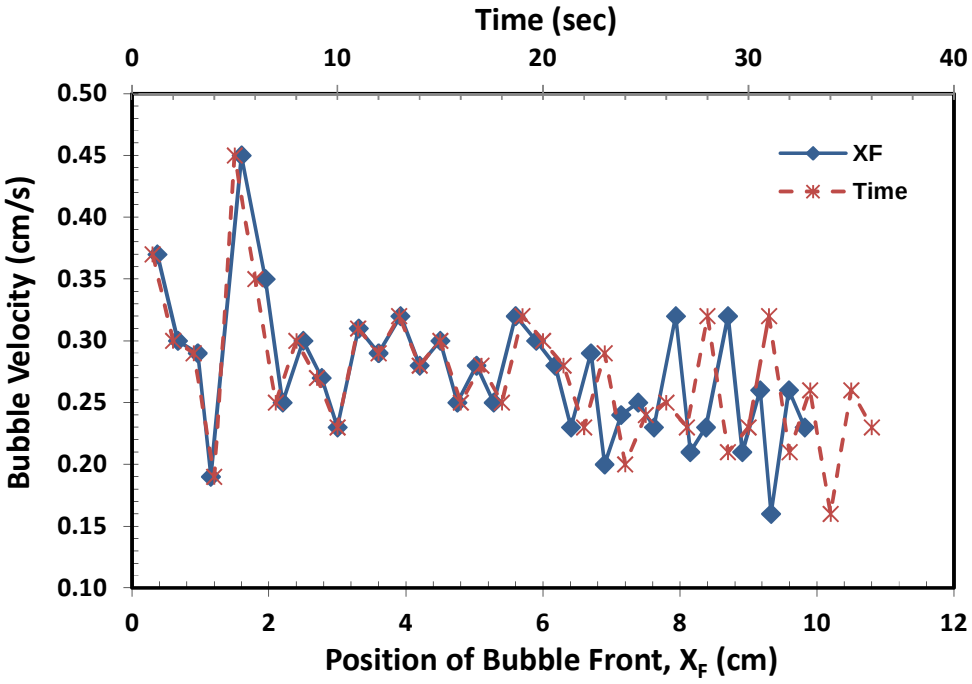

Figure 4-16: Variations of Bubble Velocity with Time and Bubble Front Position for L_{bo} = 2.5 cm and α_{dip} = 25° (White Oil)

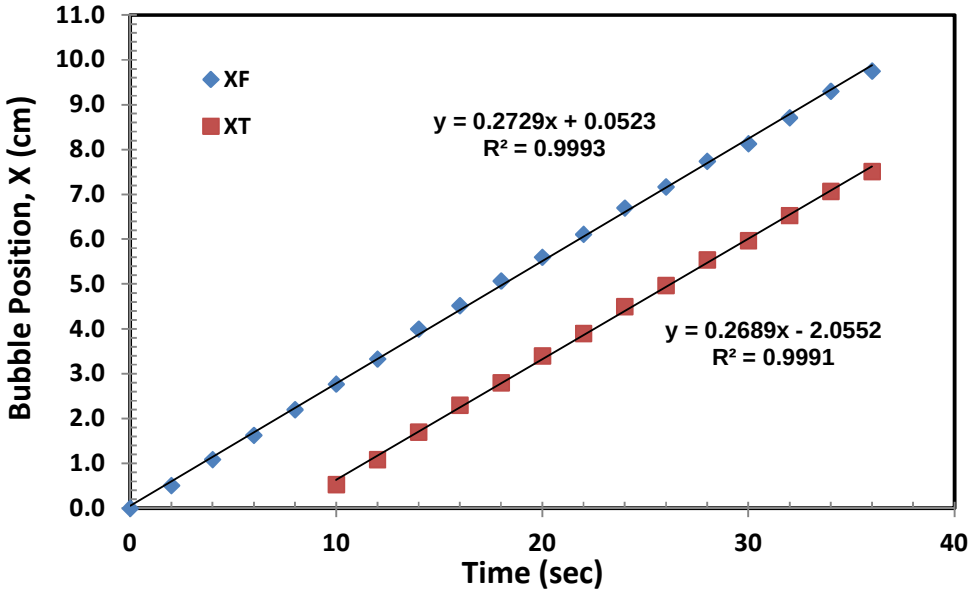

Figure 4-17: Plot of Bubble Front and Bubble Tail Positions versus Time for L_{bo} = 1.9 cm and α_{dip} = 32° (White Oil)

The values of dynamic bubble lengths differ from the static bubble lengths measured at the beginning of the experiments before the bubble was made to move. Figure 4-18 shows photographs of the moving bubbles with different lengths and dip angles. It was observed that bubbles with the same static lengths, [(a) and (b)] or [(c) and (d)], exhibited different dynamic lengths during upward movement due to different angles of inclination. Moreover, the dynamic lengths were always larger than their initial length over the range of dip angles in this work. Another interesting observation was that the shapes of the bubble tail ends changed while traveling fast enough. Moving bubbles stretched in length and their tail deformed in shape and became very narrow during upward migration through an inclined porous medium. These changes were most significant for longer bubbles during fast motion, and nearly nonexistent for bubbles moving at low speeds. The deformation of the bubble tail was such that the curvature of the interface at the back of the bubble increased significantly. This rear interface stopped expanding and could not occupy the pore space upon reaching a pore body. The reason for this behavior may be explained by the fact that some of the liquid displaced from the front of the bubble returned back to the rear of the bubble through the side passageways and accumulated between the bubble and the pore walls, resulting in a narrowing of the shape of the tail-end. Another possible explanation of this phenomenon is that a pressure build-up occurred at the top of the fast-moving bubbles, which would be relatively large in comparison with its pressure under static conditions. Therefore, the shape and the curvature of the bubble tail changes in order to create the same pressure inside the bubble. According to Ajaev and Homsy (2006), both capillary and viscous effects are important at the leading edge of the bubble. However, near the sides of the bubble at the tail end, the dominant effect is the capillary pressure gradient, which causes a draining flow from the top of the bubble (low curvature) to the rear end of the bubble (higher curvature). Another type of deformation was observed for bubbles moving very quickly (i.e. very long bubbles). In this case, the tail of the bubble became flattened, but the very end tip grew a little bit such that the size of the bubble at the tail section decreased from normal size to very thin and then increased again. A photograph of a long bubble with this type of deformation in the shape of the tail section is shown in Figure 4-19. The bubbles with long enough lengths showed such shape deformations and were more likely to cause break-up during fast motion, leaving behind a portion of immobile bubble.

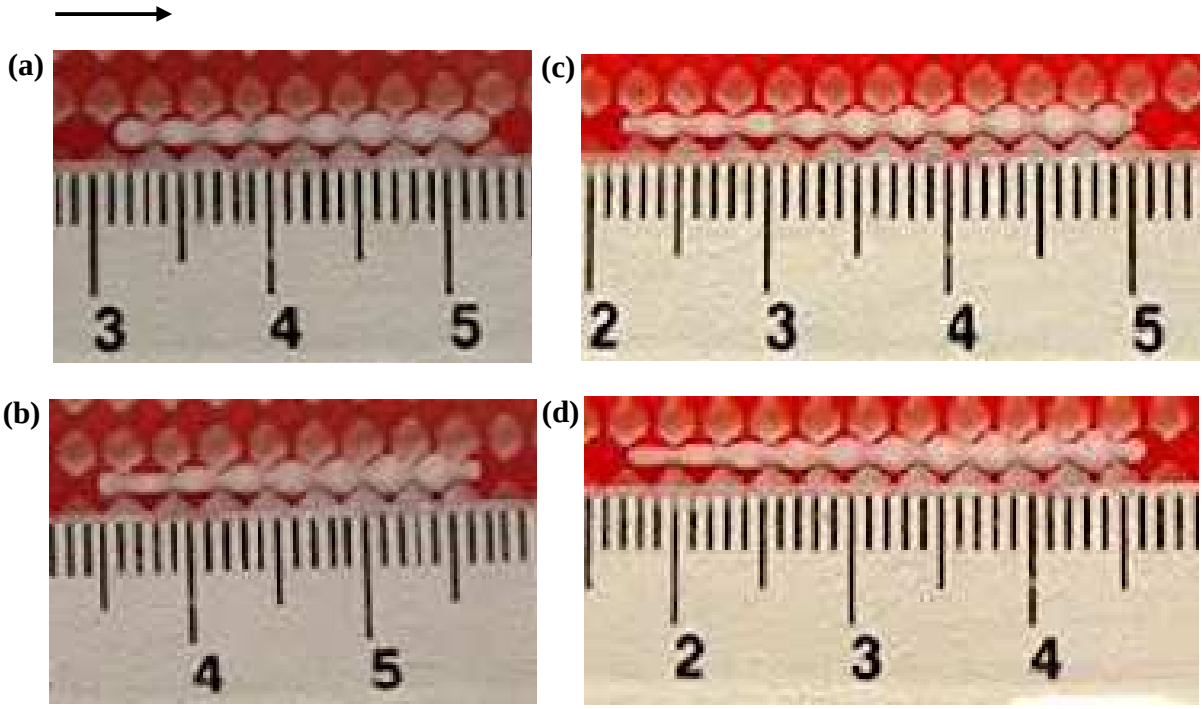

Figure 4-18: Photographs of Rising Bubbles Showing the Dynamic Lengths and Shapes for (a) L_{bo} = 1.9 cm and α_{dip} = 12°, (b) L_{bo} = 1.9 cm and α_{dip} = 25°, (c) L_{bo} = 2.5 cm and α_{dip} = 12°, and (d) L_{bo} = 2.5 cm and α_{dip} = 25° (dyed White Oil)

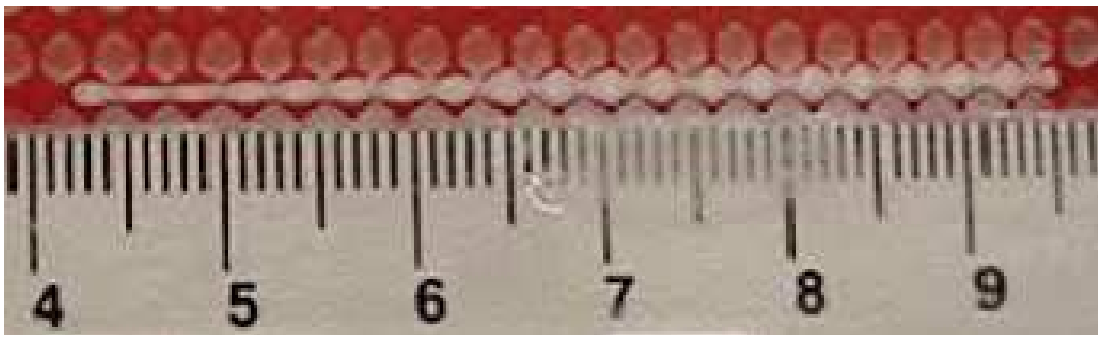

Figure 4-19: Photograph Showing the Bubble Tail Deformation for Very Long Bubbles for the Case L_{bo} = 4.7 cm and α_{dip} = 11° (dyed White Oil)

Variations of dynamic bubble length with Sin α_{dip} for various bubble sizes are shown in Figure 4-20. As seen, dynamic bubble length increases with increasing the sine dip angle for a given static bubble length and then decreases upon reaching a certain value of bubble velocity at larger angles of elevation. The critical velocity above which the dynamic length of bubbles decreases with further increase in velocity was about 0.2 cm/s in this work. The reason for the change in the bubble behavior at critical velocity is

that the bubble tends to keep its stability and prevent division by shrinkage. These changing trends are more remarkable for larger bubbles. Figure 4-21 shows the average bubble velocity as a function of both dynamic and static bubble lengths measured at $\alpha_{dip}=13^{o}$. Similar to the results discussed in §4.1.3, the bubble velocity increases linearly with increasing dynamic bubble length (or static bubble length). The higher correlation coefficient for the trendline of the bubble velocity versus the dynamic length indicates that the experimental data dictate consideration of the bubble motion in the rise velocity measurements.

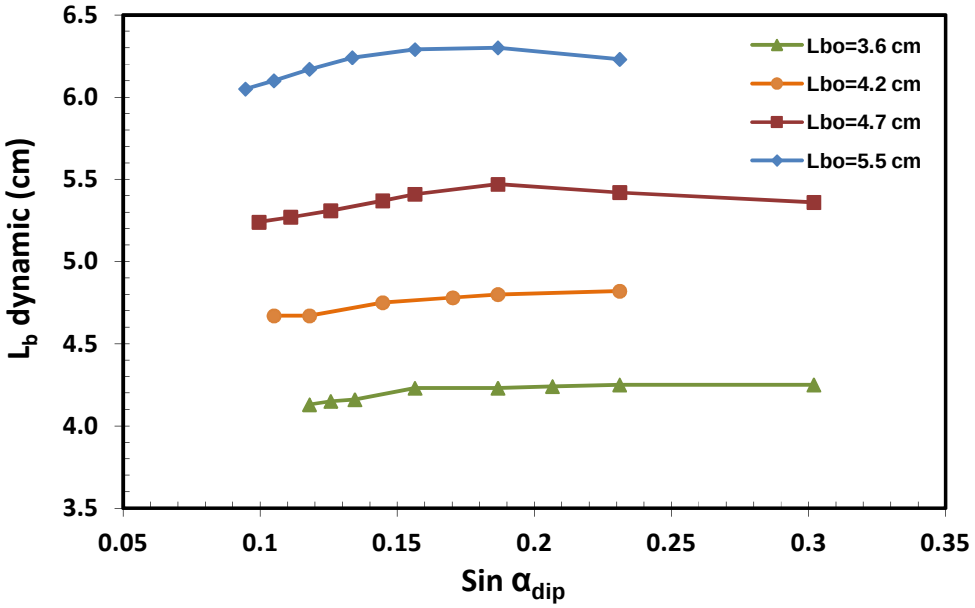

Figure 4-20: Variations of Dynamic Bubble Length with the Sin α_{dip} for Different Bubble Sizes (White Oil)

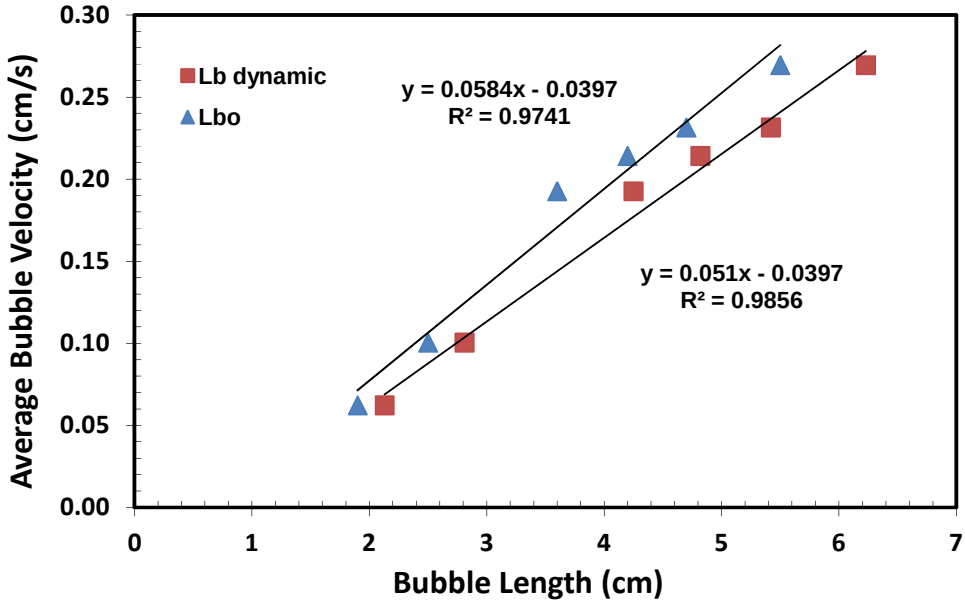

Figure 4-21: Average Bubble Velocity versus Bubble Length for α_{dip} = 13° (White Oil)

To find a relationship L_b *dynamic* and L_{bo}, for bubbles rising in White Oil, the linear correlations found for the average bubble velocity versus the static and dynamic lengths (Figure 4-21) are equated. A linear relationship is obtained between L_{bo} and $L_b$dynamic for the specific angle of inclination, α_{dip}=13°. The relationship between the dynamic and static bubble lengths is also found by plotting the dynamic bubble length versus the static one as shown in Figure 4-22. This has been done for data obtained for the whole range of dip angles in this work.

The permeability values for the system was calculated using dynamic bubble lengths to determine the effects of bubble motion on the calculated permeability of the micromodel. Figure 4-23 presents the variations of the micromodel calculated permeability with the dynamic bubble length as well as the static length of the bubbles. The values of calculated permeability measured using static bubble lengths and dynamic bubble lengths are slightly different, but those calculated for dynamic bubbles are closer to real values as they take into consideration the bubble motion and, thus, the effects of the forces acting on the bubble during motion.

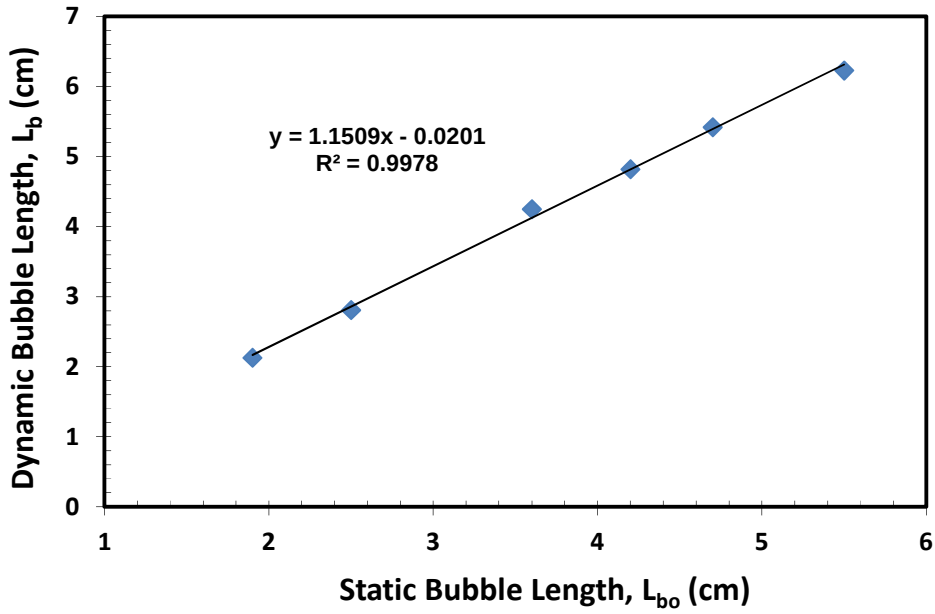

Figure 4-22: Relationship between Dynamic and Static Bubble Lengths for α_{dip} = 13° (White Oil)

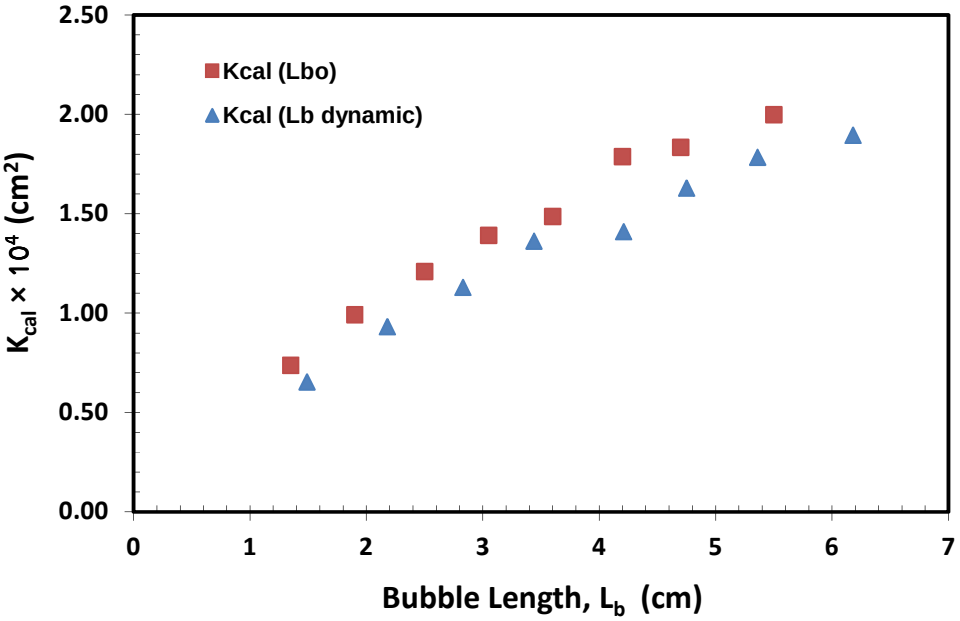

Figure 4-23: Calculated Permeability versus Bubble Length for Micromodel MP-7

4.2.3 Dimensionless Numbers

Relationship between various dimensionless numbers is discussed here to provide an investigation of the bubble migration in porous media more specifically. Reynolds number, Re, is described as the ratio of inertial to viscous forces as:

$$Re = \frac{inertial\ force}{viscous\ force} = \frac{\rho_l u_b D_T}{\mu_l} \tag{4-6}$$

where u_b is the bubble velocity, D_T is the throat diameter, ρ_l and μ_l are the density and viscosity of the test liquid, respectively. Capillary number, as discussed earlier, is the ratio of viscous to surface tension forces as:

$$Ca = \frac{viscous\ force}{surface\ tension\ force} = \frac{\mu_b u_b}{\sigma} \tag{4-7}$$

Another dimensionless number is the Bond number *Bo,* defined for a porous medium as:

$$Bo = \frac{gravity\ force}{surface\ tension\ force} = \frac{K(\rho_f - \rho_g) g \sin \alpha_{dip}}{\sigma} \tag{4-8}$$

where ρ_g is the density of gas (i.e. air), g is the gravitational acceleration, K is the calculated permeability of the pore network and σ is the surface tension of the test liquid. The density of air is too small compared to the liquid density and can be neglected in the calculations. Similar to the bubble rise velocity, the dimensionless numbers can be presented as a function of the bubble length as shown in Figure 4-24 . Capillary number (Ca) and Bond number (Bo) increase with increasing the dynamic bubble length and are numerically equal in bubble migration cases. This indicates that the viscous force and the gravitational force are in balance. A log-log plot of the relationship between the dimensionless numbers and Reynolds number is presented in Figure 4-25. Reynolds numbers calculated in this work varied from 75 to 1500 for Kerosene, from 80 to 1300 for Soltrol 170 and from 0.38 to 12.5 for White Oil.

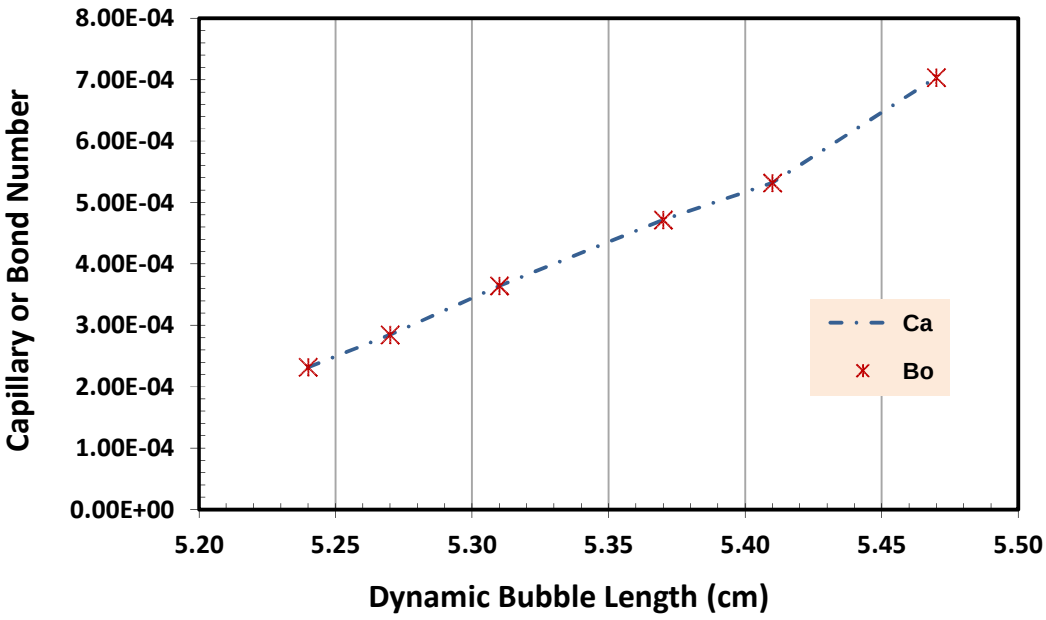

Figure 4-24: Dimensionless Numbers as a Function of the Dynamic Bubble Length for L_{bo} = 4.7 cm (White Oil)

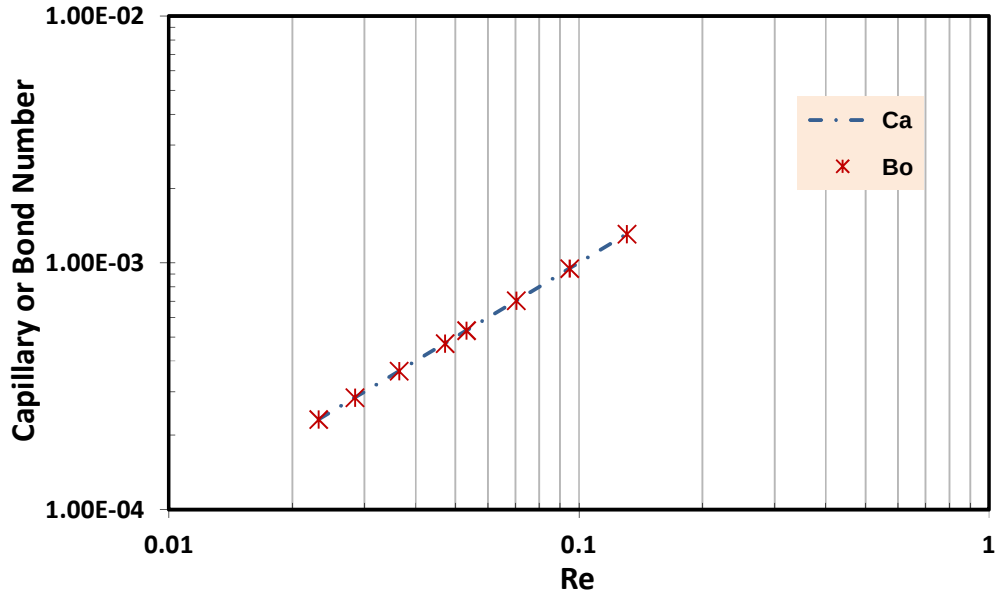

Figure 4-25: Variations of Dimensionless Numbers with Reynolds Number for L_{bo} = 4.7 cm (White Oil)

Chapter 5

MATLAB® Simulation for Bubble Migration

An appropriate and accurate numerical model can save considerable amount of time and money required in experimental analysis. A reliable numerical simulation, however, should be based on a theoretical analysis, which can produce the results reasonably close to the data obtained from experiment. Smith (2005) carried out a numerical simulation for a rising bubble in a porous medium. He used a model consisting of a two-dimensional network of pores (black circles) which are connected to their neighbors by four circular tubes (coordination number = 4) of uniform length. The bubble was placed at the central pores of the network. A schematic of the network used in his simulation is illustrated in Figure 5-1. In this work, the simulation code of Smith (2005) was modified for a more realistic condition. Some selected results are presented and compared with experimental data.

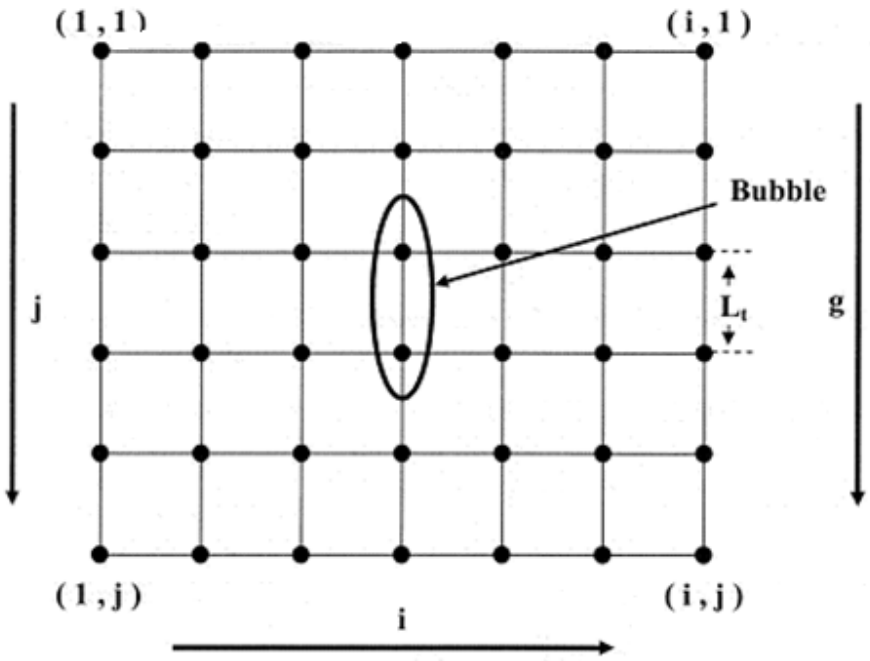

Figure 5-1: Schematic of Tube Network Used in Bubble Velocity Simulations (Smith, 2005)

5.1 Objectives

In the numerical side of this study, a Matlab® code prepared by Smith (2005) was modified in order to: (1) visualize directions of the flow inside the connecting tubes of a pore network similar to that shown in Figure 5-1, (2) study the effects of the micromodel dimensions on bubble migration velocity, and (3) study effects of accounting for different tube sizes in the vertical and horizontal orientations as well as effects of different liquids and bubble lengths on the bubble velocity calculation.

5.2 Geometry of the Model

The length of the bubble is represented by the number of nodes N_b occupied by the bubble (In Figure 5-1, N_b = 2). A special attention should be taken for determining the tube diameter, D_t, to account for the actual volume of the bubble according to the geometry of the pore structure. On the other hand, D_t should be chosen in such a way that the pressure drop calculated from the fluid flow inside tubes can accurately simulate the actual pressure drop in the micromodel used in the experiments.

The assumptions implied by the calculation procedure in this work include: (1) bubble migrates at steady state condition in the opposite direction to gravity, (2) the bubble is incompressible and thus the energy associated with the expansion and contraction of the bubble while invading pore bodies and pore throats is neglected, (3) the energy loss due to the fluid flow through the "elbows" in the tube network is negligible, and (4) no energy loss occurs from friction between the rising bubble and the liquid.

During the simulation, the position of the bubble is not changed. Instead, the effect of its movement is modeled by assuming the liquid is pushed ahead with the same velocity as the bubble to the pore located right at the tip of the bubble and accordingly, by suction of the same flow from the pore located just at the bubble tail. A pressure field is then created due to this boundary treatment according to a mass conservation scheme presented in the following section. This was also observed in the videos recorded from the bubble migration.

5.3 Numerical Model

The procedure of calculating the flow inside the tube network begins with calculating the buoyancy pressure, P_b as:

$$P_b = \left(\rho_l - \rho_g\right) g \sin\alpha_{dip} \; L_t \; N_b \tag{5-1}$$

where L_t is the length of the tubes in the network, N_b is the number of nodes occupied by the bubble, $g\sin\alpha_{dip}$ is the gravity force, ρ_l is the liquid density and ρ_g is the density of gas inside the bubble. The net capillary pressure is calculated by:

$$\Delta P_c = \frac{4\sigma}{D_t}(\cos\theta_R - \cos\theta_A) \tag{5-2}$$

where σ is the gas-liquid surface tension, D_t is the tube diameter, and θ_R and θ_A are the receding and advancing contact angles. The migration process will continue only if $P_b > \Delta P_c$ which is the necessary condition for bubble movement. An initial value for the bubble velocity is then assumed and is reduced by a constant coefficient (0.8 is considered in this work) in each step. Based on the value of bubble velocity u_b at each step, the values of pressure at all nodes are evaluated and accordingly, the total dissipation of power due to all liquid flows inside the entire network of tubes is calculated. The bubble reaches its trans velocity when the total power dissipation is equal to the power introduced into the system by the bubble motion, $Power_{in}$ defined as:

$$Power_{in} = u_b.\frac{\pi D_t^2}{4}(P_b - P_c) \tag{5-3}$$

and the total dissipated power by viscosity $power_{loss}$ is calculated from:

$$Power_{loss} = \Sigma Q_i \Delta P_{\text{tot,i}} \tag{5-4}$$

where summation, Σ, is performed over all connecting tubes, Q is the volumetric flow rate of the liquid, and $\Delta P_{tot,i}$ is the pressure drop for a laminar flow inside a tube connecting node A and B, which is calculated from the Bernoulli's Equation by:

$$(P_A + \rho g z_A + \rho u_A^2/2) - (P_B + \rho g z_B + \rho u_B^2/2) = \Delta P_{\text{tot}} = \frac{128\,\mu\, L_t Q}{\pi {D_t}^4} \tag{5-5}$$

where P_A and P_B are absolute pressure values of nodes A and B, respectively, which are calculated based on the method explained in the next section, and z_A and z_B are the hydrostatic heights measured from the top surface. The left hand side of Equation 5-5 represents the change in the potential pressures and the right hand side represents the pressure drop. The value of $\rho U^2/2$ is in fact the kinetic energy at each node and is important for higher flow velocity values. Since laminar flow with low velocity is analyzed here, this term is neglected. The value of volumetric flow is then obtained by rearranging the Equation 5-5 as:

$$Q = \frac{\pi D_t^4}{128\mu L_t}\left(P_A - P_B + \rho g\ \sin\alpha_{dip}\,\Delta z\right) \tag{5-6}$$

In order to improve the convergence of the program and finding the bubble velocity with any required tolerance, a simple half-division method is employed when the sign of ($Power_{loss}$-$Power_{in}$) changes due to reduction in u_b, i.e. when the value of u_b is close to the desired trans velocity. The solution is terminated when [($Power_{loss}$-$Power_{in}$) / $Power_{in}$] is less than a given tolerance value (set as 0.001 in this work).

5.3.1 Evaluation of Pressure Values at the Nodes

In this section, first, the implicit method of evaluating pressure values at the nodes is described and then the required boundary conditions are presented. The nodal arrangement is illustrated in Figure 5-2. By applying conservation law on each node, we have:

$$\sum_{i=1}^{4} Q_i = 0 \qquad (5\text{-}7)$$

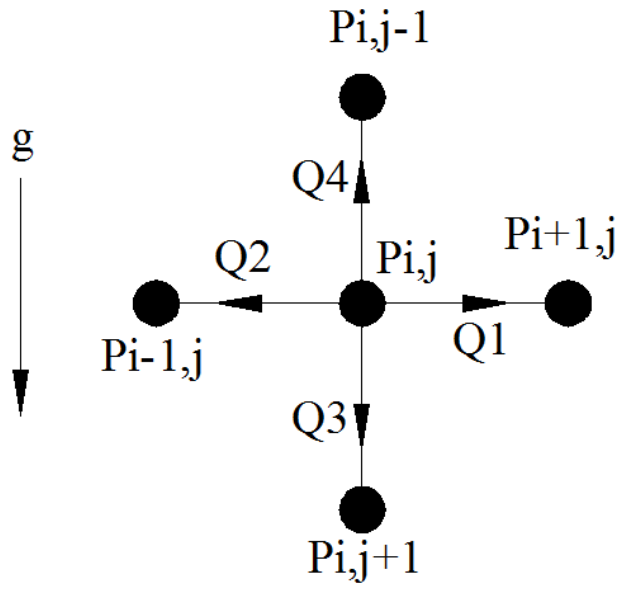

Figure 5-2: Schematic of Nodal Arrangement Used in Sample Calculations (after Smith, 2005)

Substituting Equation 5-6 into Equation 5-7 yields:

$$\frac{\pi D_t^4}{128\mu L_t}\Big(\big(A_{i,j}(P_{i,j}+\rho g z_{i,j})-A_{i,j+1}(P_{i+1,j}+\rho g z_{i+1,j})-A_{i-1,j}(P_{i-1,j}+\rho g z_{i-1,j})-A_{i,j+1}(P_{i,j+1}+\rho g z_{i,j+1})-A_{i,j-1}(P_{i,j-1}+\rho g z_{i,j-1})\big)\Big)=0 \quad (5\text{-}8)$$

This equation forms a system of linear equations when it is written for all nodes of the network (i. e. $A.P = B$, where A is the constant matrix, P is the matrix of nodal pressures, and B is the solution matrix). For a normal node inside the domain, A_{ij} is equal to four and the rest of coefficients will be equal to one. In addition, for such nodes, hydrostatic pressure terms will cancel out. For the boundary nodes located at the edges of the domain or next to the bubble nodes, the corresponding coefficient, $A_{\alpha,\beta,}$, which either are outside of the domain or cross the bubble, will be equal to zero. In this condition, net hydrostatic pressure is not equal to zero and is transferred to the right hand side of Equation 5-8 as a solution matrix. It is convenient to separate the absolute pressure terms $P_{i,j}$ into their corresponding gauge, $P_{i,j} = Pg_{i,j}$, and ambient pressure P_0. This way ambient pressure terms must be considered in the solution matrix as well.

5.4 Results and Discussions

In order to fulfill the objectives of the numerical simulation part of this study, a Matlab® code originally developed by Smith (2005) was modified. In the new code, each node was given a specific number in order to be recognized for further boundary treatment and power loss calculations. This way, the complexity and errors of recognizing a node using its position were circumvented and the essential symmetric pressure field with regard to the central node column (where bubble nodes are located) was obtained. The half-division method was adopted to effectively choose the value of bubble velocity for next step, while it is close to its steady-state value. According to the half-division method, when a change in the sign of ($Power_{loss}$-$Power_{in}$) occurs, a new guess for the bubble velocity will be the average of the bubble velocity values of last two steps. This improved the convergence of the simulation process and gave us the ability to obtain velocity results for the cases in which the diameter of the vertical and horizontal tubes are different. In addition, a visualization part was added to illustrate the flow directions inside tubes by vectors with appropriate length according to the intensity of the flow.

To improve the accuracy of the method, it was first noted that it is more realistic to consider a tube diameter with which the actual volume of the bubble can be modeled, instead of just considering throat diameters. This requires to have a larger diameter than the throat diameter. Furthermore, this diameter should account for the pressure drop of the liquid flow in the tube, which prevents an arbitrary choice. Therefore, in this study, the hydraulic diameter of the pore throat is set equal to the diameter of interconnecting tubes. Then, the buoyancy pressure is modified by a ratio of the real pore volumes to the tube volumes in the model. The hydraulic diameter is obtained from:

$$D_h = \frac{4A}{P_{wet}} \tag{5-9}$$

where A is the cross sectional area and P_{wet} is the wetted perimeter of the tube. The rest of the assumptions of the original code were not changed.

The bubble velocity was calculated for different bubble lengths in different network sizes. Figure 5-3 and 5-4 show the calculated values of the bubble velocity from experiments and MATLAB® simulation as a function of bubble length for three grid sizes and dip angles. As seen, the simulation results show a linear relationship between the terminal bubble velocity (bubble velocity at steady-state condition) and the bubble length. The agreement between the experimental data and simulation values is good for bubbles of longer length and higher velocity (Excellent agreement is seen for α_{dip}=20º). However, the calculated values for the bubble velocity are underestimated. The reason for underestimation of bubble velocities is due to the fact that in the simulation, bubble is always assumed to be inside the tubes, while in the reality, bubble is moving through the pores and tubes within the pore network. Thus, the calculated surface tension force resisting the bubble motion is higher and the calculated bubble velocity is smaller than experimental data.

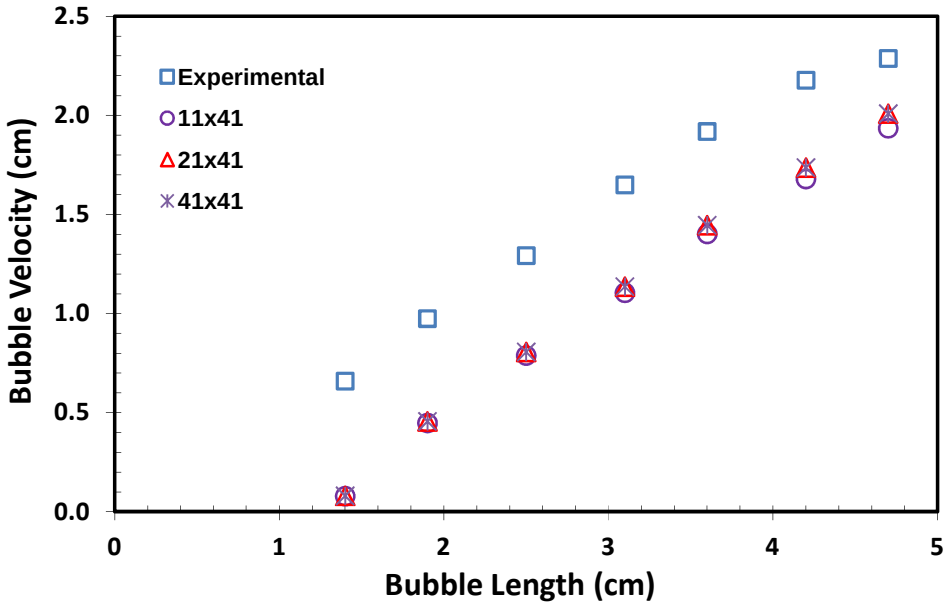

Figure 5-3: Calculated Values of Bubble Velocity in Kerosene (α_{dip}=10°) from Experiment and Simulation for Various Grid Sizes

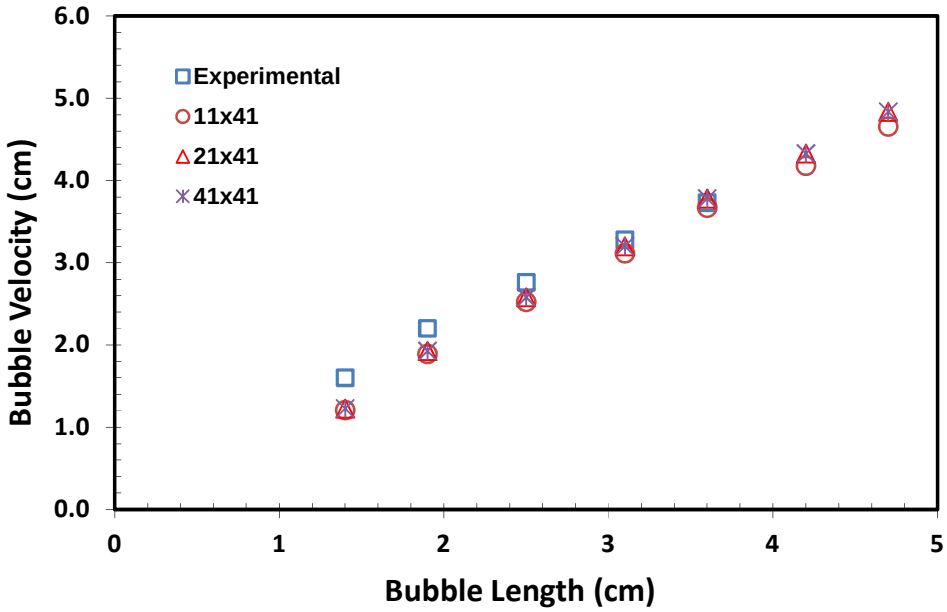

5-4: Calculated Values of Bubble Velocity in Kerosene (α_{dip}=20°) from Experiment and Simulation for Various Grid Sizes

Figure 5-5 shows a bubble of length 1.4 cm (N_b = 5), rising in pore networks of different grid sizes saturated with Soltrol 170 for α_{dip} = 10º. The physical properties of the Soltrol 170 are taken from Table 4-2. The gas density is set as 0.0001 g/ml. As seen, the bubble velocity is different for a smaller domain due to interactions with sidewalls. As is expected, if the domain size is bigger than a specific amount, effects of these interactions become smaller and the bubble velocity will not change significantly with further increase in the grid size.

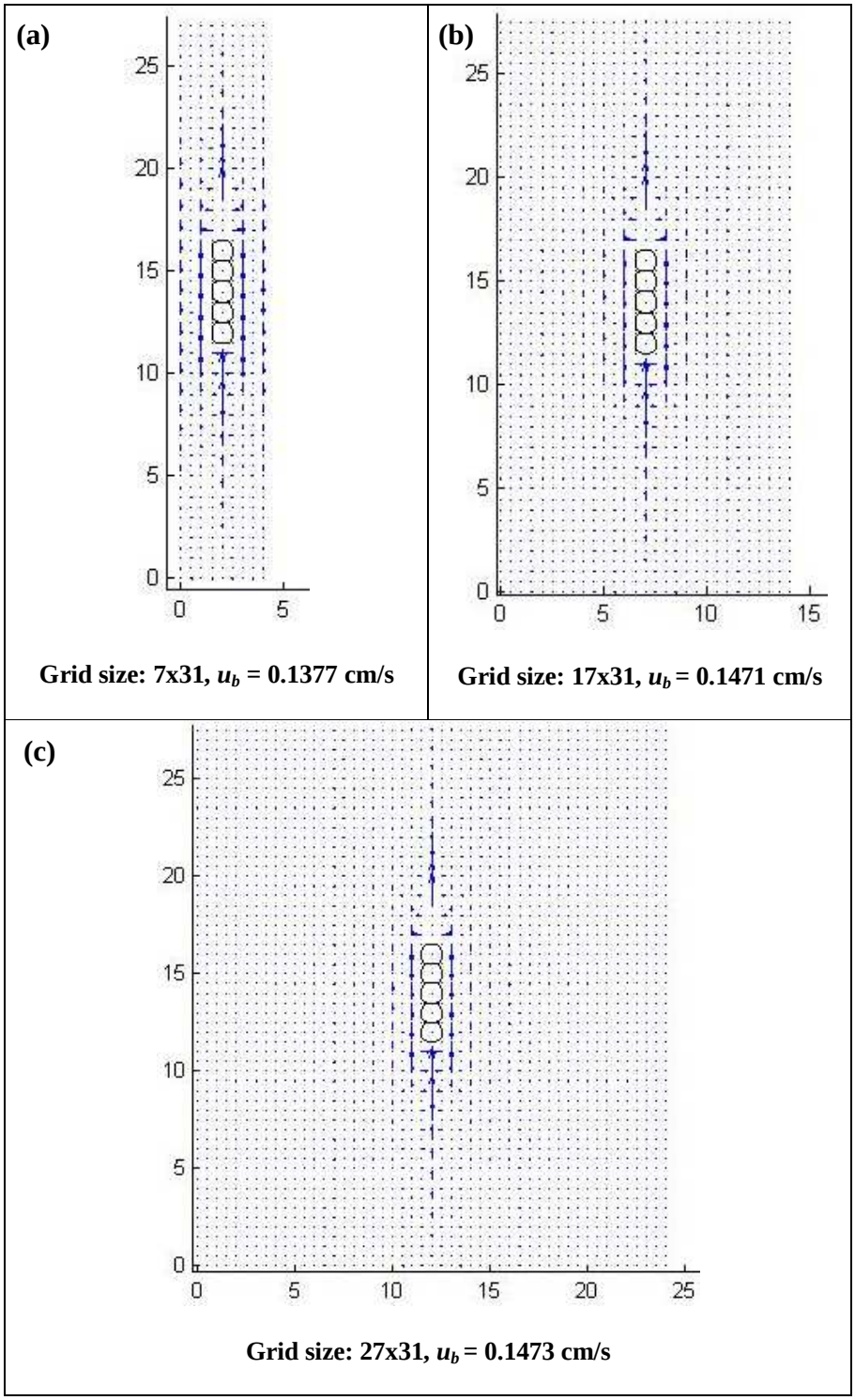

Figure 5-5: Rise Velocity of a Bubble with a Length of 1.4 cm (N_b = 5) in Porous Media with Three Different Domain Sizes and α_{dip} = 10° (Soltrol 170)

In Figure 5-6, two different tube arrangements are compared. For case (a), the diameters of horizontal tubes are 0.025 cm and those of vertical tubes are 0.055 cm; but, for case (b), the horizontal tube diameters are increased to 0.035 cm, while the vertical tube diameters remains constant. As seen, the bubble velocity increased for case (b) and the flow field is stretched in horizontal direction. The reason for the increase in bubble velocity is that for larger horizontal tube diameters, the resistance to the liquid flow in the tubes due to the surface tension force is smaller and, consequently, the fraction of the flow that travels from top of the bubble to the side channels and then to the tail of the rising bubble is larger, thus, the bubble velocity is increased.

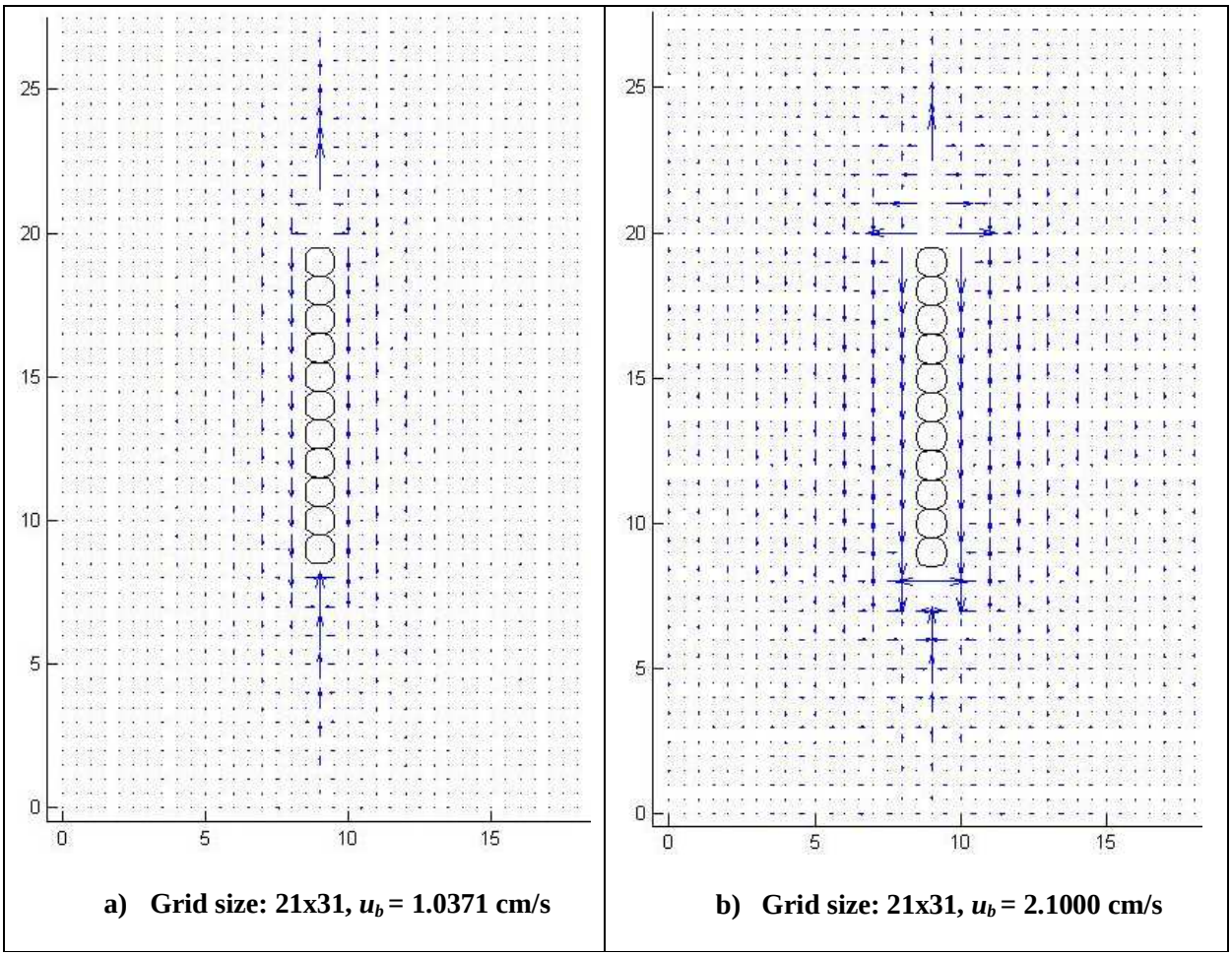

a) Grid size: 21x31, u_b = 1.0371 cm/s **b) Grid size: 21x31, u_b = 2.1000 cm/s**

Figure 5-6: Calculated Velocity for a Bubble of 2.5 cm Length (N_b = 11) for Vertical and Horizontal Tube Diameters of (a) $D_{Horizontal}$ = 0.025 cm and $D_{Vertical}$ = 0.055 cm, and (b) $D_{Horizontal}$ = 0.035 cm and $D_{Vertical}$ = 0.055 cm (Soltrol 170)

5-1 gives the calculated velocity for a bubble of 2.5 cm length (N_b = 11) for different tube arrangements when the vertical tube diameter remains constant and the horizontal tube diameter varies. As shown, the bubble rise velocity increases with increasing the horizontal tube diameter.

5-1: Calculated Velocity for a Bubble of 2.5 cm Length (N_b = 11) for Various Vertical and Horizontal Tube Diameters for α_{dip}=10° and Grid Size: 21x31 (Soltrol 170)

Vertical Tube Diameter (cm)	**0.055**	**0.055**	**0.055**	**0.055**
Horizontal Tube Diameter (cm)	**0.015**	**0.025**	**0.035**	**0.045**
Bubble Velocity (cm/s)	**0.3023**	**1.0371**	**2.1000**	**3.4688**

Chapter 6
Conclusions

The following conclusions can be drawn from the findings of this work:

- The bubble migration velocity in a liquid-saturated porous medium is a function of the bubble length, inclination angle, the permeability and the physical properties of the wetting liquid. The bubble velocity increased with increasing bubble length and inclination angle.
- It was observed that rising bubbles stretched in length and the tail end of bubbles deformed in shape and became very narrow during the upward migration through a porous medium. This behavior was more significant for longer bubbles moving at high speeds, and nearly nonexistent for bubbles moving at low speeds. The reason could be explained by the fact that some of the liquid displaced from the front of the bubble returns back to the rear of the bubble through the side passageways and accumulates in between the bubble and the pore walls, resulting in a deformation in the shape of the tail end to a narrower shape to minimize the pressure difference within the gas phase.
- The calculated permeability of the porous medium increased with increasing the bubble length. This finding suggested that an effective bubble length, L_{eff}, is responsible for the flow around the bubble during its upward motion. L_{eff} is a function of permeability, fluid properties, pore geometry and connectivity.
- The value of L_{eff} is much smaller than the bubble length, particularly for long bubbles.
- The results of numerical simulation of a rising bubble in a saturated porous medium showed that the velocity of a bubble is affected by the presence of boundaries around the pore network, similarly, by the presence of other bubbles in the porous medium. It was found that the velocity of bubbles rising in pore networks increases with enlarging the domain of the bubble flow (i.e. the number of the pores in the vertical and horizontal dimensions) until it reaches a critical value at a particular domain size above which the velocity does not change with increasing the dimensions of the network.

Chapter 7

Recommendations for Future Work

The following recommendations are made based on the results of this work for future works:

- This work could be expanded by using different micromodels of varying network pattern and pore sizes in order to determine the effects of pore structure and variable geometry on the bubble rise velocity.
- Although the values of effective length, L_{eff}, was calculated in this work and a linear relationship between the (L_{bo}/L_{eff}) ratio and bubble length was found, predicting L_{eff} and determining the effects of permeability and pore geometry on it requires extensive study with a number of micromodels of different geometry and numerical simulations.
- Additional experimental studies using micromodels with various horizontal grid sizes (as simulated in Chapter 5) could be conducted to investigate the effects of walls near a rising bubble, so-called "wall effects", on the bubble migration in detail. Determining the wall effect will help in finding a correlation that accounts for the effects of other bubbles present around a rising bubble on the bubble rise velocity.

References

Adamson, A.W., Physical Chemistry of Surfaces, 5th ed.; Wiley & Sons Inc.: New York; pp 379, **1990**.

Ajaev, V. S., and Homsy, G. M., "Modeling shapes and dynamics of confined bubbles", *Annual Review of Fluid Mechanics*, 38, 277-307, **2006**.

Amos, R. T., Mayer, K. U., Bekins, B. A., Delin, G. N., and Williams, R. L., "Use of dissolved and vapor- phase gases to investigate methanogenic degradation of petroleum hydrocarbon contamination in the subsurface", *Water Resources Research*, 41 (2), **2005**.

Amos, R. T., and Mayer, K. U., "Investigating ebullition in a sand column using dissolved gas analysis and reactive transport modeling", *Environmental Science & Technology*, 40, 5361-5367, **2006**.

Anderson, W.G., "Wettability literature survet- Part 2: Wettability measurement", *Journal of Petroleum Technology*, 38, 1246-1262, **1986**.

Bear, J., "Dynamics of Fluids in Porous Media", American Elsevier Publishing Co., New York, 763 pp, **1972**.

Bendiksen, k. H., "An experimental investigation of the motion of long bubbles in inclined tubes", *International Journal of Multiphase Flow*, 10 (4), 467-483, **1984**.

Bendiksen, k. H., "On the motion of long bubbles in vertical tubes", *International Journal of Multiphase Flow*, 11 (6), 797-812, **1985**

Bico, J., and Quéré, D., "Rise of liquids and bubbles in angular capillary tubes", *Journal of Colloid and Interface Science*, 247 (1), 162-166, **2002**.

Bretherton, F. P., "The motion of long bubbles in tubes", *Journal of Fluid Mechanics*, 10, 166-188, **1961**.

Brooks, M. C., Wise, W. R., and Annable, M. D., "Fundamental changes in in-situ air sparging flow patterns", *Ground Water Monitoring & Remediation*, 19, 105-113, **1999**.

Chambers, J. E., Loke, M. H., Ogilvy, R. D., Meldrum, P. I., "Noninvasive monitoring of DNAPL migration through a saturated porous medium using electrical impedance tomography", *Journal of Contaminant Hydrology*, 68 (1-2), 1-22, **2004**.

Chatzis, I., and Dullien, F. A. L., "Modeling pore structure by 2-D and 3-D networks with application to sandstones", *Journal of Canadian Petroleum Technology*, 16 (1), 97-108, **1977**.

Chatzis, I., “Photofabrication technique of two-dimensional glass micromodels”, PRRC Rep. 82-12, N. M. Inst. Of Min. and Technol., Socorro, **1982**.

Chatzis, I., Morrow, N. R., and Lim, H. T., “Magnitude and detailed structure of residual oil saturation”, *Society of Petroleum Engineers Journal*, 23 (2), 311-326, **1983**.

Chatzis, I., and Morrow, N. R., “Correlation of capillary number relationships for sandstone”, , *Society of Petroleum Engineers Journal*, 24 (5), 555-562, **1984**.

Chatzis, I., Kantzas, A., and Dullien, F. A. L., “On the investigation of gravity-assisted inert gas injection using micromodels, Long Berea sandstone cores, and computer-assisted tomography”, paper SPE 18284 presented at the **1988** SPE Annual Technical Conference and Exhibition, Houston, October 2-5.

Chatzis, I., “Mobilization of residual oil mechanisms seen in micromodels”, International Symposium of Core Analysis, Austin, USA, **2011**.

Cihan, A., and Corapcioglu, M. Y., “Effect of compressibility on the rise velocity of an air bubble in porous media”, *Water Resources Research*, 44 (4), W04409, **2008**.

Cohen, R.M., and Mercer, J.W., “DNAPL Site Evaluation”, 1st Ed., C. K. Smoley, Boca Raton, Florida, USA, 384 pp, **1993**.

Corapcioglu, M. Y., Cihan, A., and Drazenovic, M., “Rise velocity of an air bubble in porous media: Theoretical Studies”, *Water Resources Research*, 40 (4), **2004**.

Craig, F.F., Jr., “The reservoir engineering aspects of water-flooding”, Society of Petroleum Engineers of AIME, Monograph, Vol. 3, Dallas, Texas, **1971**.

Crowe, C. T., Schwarzkopf, J. D., Sommerfeld, M., and Tsuji, Y., “Multiphase flows with droplets and particles”, CRC Press, **1988**.

Dong, M., and Chatzis, I., “The imbibitions and flow of a wetting liquid along the corners of a square capillary tube”, *Journal of Colloid and Interface Science*, 172 (2), 278-288, **1995**.

Dullien, F. A. L., “Porous Media: Fluid Transport and Pore Structure”, Academic Press, Toronto, **1992**.

Haley, J.L., Hanson, B., Enfield, C., Glass, J., “Evaluating the effectiveness of ground water extraction systems. *Ground Water Monitoring & Remediation*, 12 119–124, **1991**.

Hirasaki, G. J., “Structural Interactions in the Wetting and Spreading of Vanderwaals Fluids”, *Journal of Adhesion Science and Technology*, 7 (3), 285-322, **1993**.

Holm, L. W., “Mobilization of waterflood residual oil by miscible fluids”, 1 (4), *SPE Reservoir Engineering Journal*, 354-362, **1986**.

Hui, M.H., and Blunt, M.J., “Effects of Wettability on Three-Phase Flow in Porous Media”, *The Journal of Physical Chemistry B*, 104, 3833-3845, **2000**.

Iliuta, I., Larachi, F., and Grandjean BPA, “Residence time, mass transfer, and back-mixing of the liquid in trickle flow reactors containing porous particles”, *Chemical Engineering Science*, 54 (18), 4099-4109, **1999**.

Ioannidis, M. A., Chatzis, I., Payatakes, A. C., “A mercury porosimeter for investigating capillary phenomena and microdisplacement mechanisms in capillary networks”, *Journal of Colloid and Interface Science*, 143 (1), 22-36, **1991**.

Ji, W., Dahmani, A., Ahlfeld, D. P., Lin, J. D., and Hill III, E., “Laboratory study of air sparging: Air flow visualization”, *Ground Water Monitoring & Remediation.*, 13 (4), 115-126, **1993**.

Johnson, R.J., Pankow, J.F., “Dissolution of dense chlorinated solvents into groundwater: 2. Source functions for pools of solvents”, *Environmental Science and Technology*, 26 (5), 896–901, **1992**.

Johnson, R.L., Johnson, P.C., McWhorter, D.B., Hinchee, R.E., and Goodman, I., “An overview of in situ air sparging”. *Ground Water Monitoring & Remediation*, 13, No. 4, 127-135, **1993**.

Johnson, P.C., “Assessment of the contributions of volatilization and biodegradation to in situ air sparging performance”, *Environmental Science and Technology*, 32 (2), 276–281, **1998**.

Jones, S. C., “Some surprises in the transport of miscible fluids in the presence of a second immiscible phase”, *Society of Petroleum engineering Journal*, 25 (1), 101-112, **1985**.

Jones, S. F., Evans, G. M., and Galvin, K. P., “Bubble nucleation from gas cavities-a review”, *Advances in Colloid and Interface science*, 80, 27-50, **1999**.

Kantzas, A., Chatzis, I., and Dullien, F. A. L., “Enhanced oil recovery by inert gas injection”, paper SPE 17379 presented at the **1988** SPE Enhanced Oil Recovery Symposium, Tulsa 17-20.

Kantzas, A., Chatzis, I., and Dullien, F. A. L., “Mechanisms of capillary displacement of residual oil by gravity-assisted inert-gas injection”, paper SPE 17506 presented at the **1988** SPE Rocky Mountain Regional Meeting, Casper 11-13.

Lenormand, R., Zarcone, C., and Sarr, A., “Mechanisms of the displacement of one fluid by another in a network of capillary ducts”, *Journal of Fluid Mechanics*, 135, 337-353, **1983**.

Li, M., “Recovery of non-aqueous phase liquids from contaminated soil by CO2-supersaturated water injection”, M.A.Sc.Thesis, University of Waterloo, Canada, **2009**.

Li, T. M. W., Ioannidis, M., and Chatzis, I., “Recovery of non-aqueous phase liquids from ground sources”, United State Patent 7300227, **2007**.

Li, T., “Recovery of source non-aqueous phase liquids from groundwater using supersaturated water injection”, M.A.Sc.Thesis, University of Waterloo, Canada, **2004**.

Li, T., Ioannidis, M. A., and Chatzis, I., "Recovery of non-aqueous phase liquids from ground sources", USA patent 20070014633, Issued on Nov. 27, **2007**.

Lubetkin, S.D., and Blackwell, M., “The nucleation of bubbles in supersaturated solutions”. *Journal of Colloid and Interface Science*, 26 (2), 610-615, **1988**.

Mackay, D. M., and Cherry, J. A., “Groundwater contamination: pump-and-trat remediation”, *Environmental Science and Technology*, 23 (6), 630-636, **1989**.

McCray, J. E., and Falta, R. W., “Numerical simulation of air sparging for remediation of NAPL contamination”, *Ground Water*, 35 (1), 99-110, **1997**.

McKellar, M., and Wardlaw, N. C., “A method of making two-dimensional glass micromodels of pore systems”, *Journal of Canadian Petroleum Technology*, 21 (4), 39-41, **1982**.

National Research Council, “Alternatives for Groundwater Cleanup”; National Academy Press: Washington DC, **1994**.

Nelson, L., Barker, J., Li, T., Thomson, N., Ioannidis, M. A., and Chatzis, I., “A field trial to assess the performance of CO2-supersaturated water injection for residual volatile LNAPL recovery”, *Journal of Contaminant Hydrology*, 109, 82-90, **2009**.

Nickens, H. V., and Yannitell, D. W., “The effects of surface tension and viscosity on the rise velocity of a large gas bubble in a closed, vertical, liquid-filled tube”, *International Journal of Multiphase Flow*, 13 (1), 57-69, **1987**.

Nicklin, D. J., Wilkes, J. O., and Davidson, J. F., “Two-phase flow in vertical tubes”, *Transactions of the Institution of Chemical Engineers*, 40, 61-68, **1962**.

O'Carrol, D. M., Abriola, L. M., Polytica, C. A., Bradford, S. A., and Demond, A. H., "Prediction of two-phase capillary pressure–saturation relationships in fractional wettability systems", *Journal of Contaminant Hydrology*, 77, 247-270, **2005**.

Olbricht, W. L., "Pore-scale prototypes of multiphase flow in porous media", *Annual Review of Fluid Mechanic*, 28, 187-213, **1996**.

Oldenburg, C. M., and Lewicki, J. L., "On leakage and seepage of CO2 from geologic storage sites into surface water", *Environmental Geology*, 50, 691-705, **2006**.

Oren, P. E., Billiotte, J., and Pinczewski, W. V., "Mobilization of waterflood residual oil by gas injection for water-wet conditions", *Society of Petroleum Engineers Journal*, 7 (1), 70-78, **1992.**

Pankow, J. F., Johnson, R. L., and Cherry, J. A., "Air sparging in gate wells in cutoff walls and trenches for control of plumes of volatile organic compounds (VOCs)", *Ground Water*, 31, 654-663, **1993**.

Pankow J. F., Cherry, J. A., "Dense chlorinated solvents and other DNAPLs in groundwater", Waterloo Press, **1996**.

Ratulowski, J., and Chang, H.-C., "Transport of gas bubbles in capillaries", *Physics of Fluids A*, 1, 1642-1655, **1989**.

Roosevelt, S. E., and Corapcioglu, M. Y., "Air bubble migration in a granular porous medium: Experimental studies", *Water Resources Research*, 34 (5), 1131-1142, **1998**.

Ryan, M. C., MacQuarrie, K. T. B., Harman, J., and McLellan, J., "Field and modeling evidence for a "stagnant flow" zone in the upper meter of sandy phreatic aquifers", *Journal of Hydrology*, 233 (1-4), 223-240, **2000**.

Sahloul, N. A., Ioannidis, M. A., and Chatzis, I., "Dissolution of residual non-aqueous phase liquids in porous media: pore-scale mechanisms and mass transfer rates", *Advances in Water Resources*, 25, 33-49, **2002**.

Semer, R., and Reddy, K. R., "Mechanisms controlling toluene removal from saturated soils during in situ air sparging", *Journal of Hazardous Materials*, 57 (1-3), 209-230, **1998**.

Smith, J. D., "Mobility of bubbles in porous media with application to non-aqueous phase liquid removal via saturated water injection", M.A.Sc. Thesis, University of Waterloo, Waterloo, Canada, **2005**.

Smith, J. D., Chatzis, I., and Ioannidis, M. A., “A new technique to measure the breakthrough capillary pressure”, *Journal of Canadian Petroleum Technology*, 44 (11), **2005**.

Stark, J., and Manga, M., “The Motion of Long Bubbles in a Network of Tubes”, *Transport in Porous Media*, 40, 201-218, **2000**.

Wan, J., and Wilson, J. L., “Visualization of the role of the gas-water interface on the fate and transport of colloids in porous media”, *Water Resources Research*, 30 (1), 11-23, **199**4.

Wehrle, K., “In-situ cleaning of CHC contaminated sites: Model-scale experiments using the air injection (in-situ stripping) method in granular soils”, in *Contaminated Soil '90*, edited by F. Arendt, M. Hinsenveld, and W. J. van den Brink, pp. 1061-1062, Kluwer Acad., Norwell, Mass., **1990**.

Whalen, S. C., “Biochemistry of methane exchange between natural wetlands and the atmosphere”, *Environmental Engineering Science*, 22, 73-94, **2005**.

Wilson, J.L., Conrad, S.H., Mason, W.R., Peplinski, W., and Hogan, E., “Laboratory investigations of residual liquid organics from spill, leaks, and disposal of hazardous wastes in groundwater”, EPA/600/S6-90/004, Ada, Okla, **1990**.

Young, F. R., “Cavitation”, McGraw-Hill, London, **1989**.

Zhou, D., and Blunt, M., “Effect of spreading coefficient on the distribution of light non-aqueous phase liquid in the subsurface”, *Journal of Contaminant Hydrology*, 25, 1-19, **1997**.

Appendix A

MATLAB ® Code for the Simulation of Bubble Migration

```
clc;
clear;

% Bubble Rise Velocity Simulator
%
% This simulator attempts to calculate the pressure field around a bubble
% moving upwards at steady-state through a porous material, or in this
% case, a network of tubes of uniform diameter

% Define dimension of tube grid
% IMPORTANT: Grid sizses must always be ODD integer numbers

GridSizeX=41;   %Grid szse in X (horizontal) direction
GridSizeY=41;   %Grid size in Y (vertical) direction

% Define important system parameters (CGS Units)

Mu=0.0095;  % Liquid viscosity (poise)
RhoL=0.783; % Liquid density (g/ml)
RhoG=0.001; % Gas density (g/ml)
Sigma=24.6; % Gas-Liquid surface tension (dyne/cm)
g=981;      % Gravitational acceleration constant (cm/s2)
Theta=20;       % Inclination angle (degree)

G=g*sin(Theta/90*pi/2); % Acceleration due to gravity (cm/s2)

p=101325;   % Boundary pressure (dyne/cm2)

TDiameterH=0.025;       % Horizontal tube diameter (cm)
TDiameterV=0.055;       % Vertical tube diameter (cm)
TDiameterHS=0.025;  % Special horizontal tube diameter
TDiameterVS=0.055;  % Special vertical tube diameter
TDiameterEXT=0.075; % Exterior nodes tube diameter (cm)
TLength=0.28;       % Tube length (cm)

% Define Hagen-Poiseoille equation constant [pi*D^4/(128*Mu*L)]
% Q=C*(pressure drop)

CH=pi*TDiameterH^4/(128*Mu*TLength);
CV=pi*TDiameterV^4/(128*Mu*TLength);
CHS=pi*TDiameterHS^4/(128*Mu*TLength);
CVS=pi*TDiameterVS^4/(128*Mu*TLength);
CEXT=pi*TDiameterEXT^4/(128*Mu*TLength);
```

```
% Define bubble size
% IMPORTANT: bubble size must always be an odd integer number
% Size implies how many nodes the bubble encompasses. Actual length is set
% to be arbitrarily larger than the length of what the size (in nodes)
% would be

BubbleSize=7;

% Calculate bubble length (cm)

BubbleLength=(BubbleSize+1)*TLength*1.15;

% Calculate buoyancy and surface tension forces/pressures

BuoyancyPressure=(RhoL-RhoG)*G*BubbleLength;

SurfaceTensionPressure=4*Sigma/TDiameterV*(cos(0)-cos(pi/6));

% Define array to hold equation set
% ConstantMatrix*UnknownMatrix=AnswerMatrix

NX=GridSizeX-2; % Effective grid size (X-direction)
NY=GridSizeY-2; % Effective gri size (Y-direction)

% Note: an effective grid size Must be calculated because all the exterior
% nodes for the system are considered known

EquationNumber=NX*NY;

ConstantMatrix=zeros(EquationNumber,EquationNumber);    %Array to hold
constants initialized to zero
AnswerMatrix=zeros(EquationNumber,1);   %Array to hold answer terms
initialized to zero
Solution=zeros(EquationNumber,1);       %Array to hold solved values of nodal
pressures initialized to zero

PressureField=zeros(NY,NX);
PressureField2=zeros(NY,NX);
PressureField3=zeros(NY,NX);
PotentialField=zeros(NY,NX);
prop=zeros(NX,NY);
vctrx=zeros(2*NY-1,2*NX-1);
vctry=zeros(2*NY-1,2*NX-1);
xc=zeros(2*NY-1,2*NX-1);
yc=zeros(2*NY-1,2*NX-1);

% Guess a velocity for bubble

Ububble=5;  % Initial guess for velocity (cm/s)
Q=Ububble*pi*TDiameterV^2/4;        % Calculate water flow rate based on the
velocity (ml/s)
```

```
% Main program loop
% -----------------------
%
% 1. Calculate the pressure field using the assumed bubble velocity
% 2. Check to see that friction losses based on the pressure field equal
%     the energy input to the system based on the assumed velocity
% 3. If the check fails, choose a new velocity and repeat

CheckVar=0; %Boolean variable used to terminate the simulation upon
convergence of the solution
first=0;        % Boolean variable that tracks whether the program has
alreadyu run through matrix value assignment
Counter=1;  %Used to keep track of vertical position in the coefficient
matrix
HorizontalCounter=1;    % Used to keep track of the horizontal position in
the matrix
VerticalCounter=1;  % Used to keep track of the vertical position in the
matrix
StepCounter=1;      % Used to keep track of the number o simulation
steps/loops

% Variables for solution convergence

Tolerance=0.001;        % Numerical tolerance for solution convergence
Fraction=0.8;
ConvergenceCounter=0;
LowerCheck=0;
Upperlimit=Ububble;
Upperdiff=1e16;
UpperFraction=Fraction;
LastUb=Ububble;
LastDiff=0;
PowerInput=pi*TDiameterVS^2/4*(BuoyancyPressure-
SurfaceTensionPressure)*Ububble; % Net driving force x velocity

Change1=0;
Change2=0;

TrendMatrix=zeros(1000,2);
TrendCounter=1;

if (BuoyancyPressure<SurfaceTensionPressure)

  CheckVar=1;   % Do not run the simulation if the driving force is not a
positive value
  fprintf('BuoyancyPressure is less than SurfaceTensionPressure!!!\n')

end

while (CheckVar==0)
```

```
% If this is the first time through the loop, assign the appropriate
% values inside the coefficient and answer matrices. If it isn't,
% change only the entries affected by the new guess for velocity. This
% speeds up the simulation

if (first==0)

    first=1;

    % Equation calculation loop
    % Assign the appropriate values from the mass balance equations into
    % the appropriate places in the constant and answer matrix

    for X=1:NX
        prop(1,X)=1;
        prop(NY,X)=2;
    end

    for Y=1:NY
        prop(Y,1)=prop(Y,1)*10+3;
        prop(Y,NX)=prop(Y,NX)*10+4;
    end

    for Y=((NY+1)/2-(BubbleSize-1)/2):((NY+1)/2+(BubbleSize-1)/2)
        prop(Y,(NX+1)/2)=30;
    end

    for Y=((NY+1)/2-(BubbleSize-1)/2):((NY+1)/2+(BubbleSize-1)/2)
        prop(Y,(NX+1)/2+1)=31;
    end

    for Y=((NY+1)/2-(BubbleSize-1)/2):((NY+1)/2+(BubbleSize-1)/2)
        prop(Y,(NX+1)/2-1)=29;
    end
    prop((NY+1)/2+(BubbleSize+1)/2,(NX+1)/2)=33;
    prop((NY-1)/2-(BubbleSize-1)/2,(NX+1)/2)=32;
    prop((NY+1)/2+(BubbleSize-1)/2,(NX+1)/2)=34;
    prop((NY+1)/2-(BubbleSize-1)/2,(NX+1)/2)=35;

    n=1;
    for Y=1:NY
        for X=1:NX

        % If the current node is part of the bubble, ignore it, else,
        % analyze it and assign the node it's appropriate value

        if(prop(Y,X)==30||prop(Y,X)==34||prop(Y,X)==35)

            ConstantMatrix(Counter,Counter)=1;
            HorizontalCounter=HorizontalCounter+1;
```

```
                Counter=Counter+1;

            else

                %If the node is special (i.e. if it's an exterior node or
                %next to the bubble), treat it specially. Otherwise, it is
                %a normal node (with 4 inputs/outputs) and can be
                %treated with the standard procedure

                if (prop(Y,X)==13) %Top left corner node

                    ConstantMatrix(Counter,Counter)=CV+CH; %+2*CEXT;
                    ConstantMatrix(Counter,Counter+1)=-1*CH;
                    ConstantMatrix(Counter,Counter+NX)=-1*CV;
                    AnswerMatrix(Counter,1)=CV*(TLength*G*RhoL);
%CEXT*p+CEXT*(p+VerticalCounter*TLength*G*RhoL);
                    HorizontalCounter=HorizontalCounter+1;
                    Counter=Counter+1;

                elseif (prop(Y,X)==14) %Top right corner node

                    ConstantMatrix(Counter,Counter)=CV+CH; %+2*CEXT;
                    ConstantMatrix(Counter,Counter-1)=-1*CH;
                    ConstantMatrix(Counter,Counter+NX)=-1*CV;
                    AnswerMatrix(Counter,1)=CV*(TLength*G*RhoL);
%CEXT*p+CEXT*(p+VerticalCounter*TLength*G*RhoL);
                    HorizontalCounter=1;
                    VerticalCounter=VerticalCounter+1;
                    Counter=Counter+1;

                elseif (prop(Y,X)==23) %Bottom left corner node

                    ConstantMatrix(Counter,Counter)=CV+CH; %+2*CEXT;
                    ConstantMatrix(Counter,Counter+1)=-1*CH;
                    ConstantMatrix(Counter,Counter-NX)=-1*CV;
                    AnswerMatrix(Counter,1)=-CV*(TLength*G*RhoL);
%CEXT*(p+VerticalCounter*TLength*G*RhoL)+CEXT*(p+(VerticalCounter+1)*TLength*
G*RhoL);
                    HorizontalCounter=HorizontalCounter+1;
                    Counter=Counter+1;

                elseif (prop(Y,X)==24) %Bottom right corner node

                    ConstantMatrix(Counter,Counter)=CV+CH; %+2*CEXT;
                    ConstantMatrix(Counter,Counter-1)=-1*CH;
                    ConstantMatrix(Counter,Counter-NX)=-1*CV;
                    AnswerMatrix(Counter,1)=-CV*(TLength*G*RhoL);
%CEXT*(p+VerticalCounter*TLength*G*RhoL)+CEXT*(p+(VerticalCounter+1)*TLength*
G*RhoL);
                    HorizontalCounter=1;
                    VerticalCounter=1;
```

```
                    Counter=1;

                elseif (prop(Y,X)==1) %Top non-corner node

                      ConstantMatrix(Counter,Counter)=2*CH+CV; %+CEXT;
                      ConstantMatrix(Counter,Counter-1)=-1*CH;
                      ConstantMatrix(Counter,Counter+1)=-1*CH;
                      ConstantMatrix(Counter,Counter+NX)=-1*CV;
                      AnswerMatrix(Counter,1)=CV*(TLength*G*RhoL); %CEXT*p;
                      HorizontalCounter=HorizontalCounter+1;
                      Counter=Counter+1;

                elseif (prop(Y,X)==2) %Bottom non-corner node

                      ConstantMatrix(Counter,Counter)=2*CH+CV; %+CEXT;
                      ConstantMatrix(Counter,Counter-1)=-1*CH;
                      ConstantMatrix(Counter,Counter+1)=-1*CH;
                      ConstantMatrix(Counter,Counter-NX)=-1*CV;
                      AnswerMatrix(Counter,1)=-CV*(TLength*G*RhoL);
%CEXT*(p+(VerticalCounter+1)*TLength*G*RhoL);
                      HorizontalCounter=HorizontalCounter+1;
                      Counter=Counter+1;

                elseif (prop(Y,X)==4) %Right non-corner node

                    ConstantMatrix(Counter,Counter)=2*CV+CH; %+CEXT;
                    ConstantMatrix(Counter,Counter-1)=-1*CH;
                    ConstantMatrix(Counter,Counter+NX)=-1*CV;
                    ConstantMatrix(Counter,Counter-NX)=-1*CV;
                    AnswerMatrix(Counter,1)=0;
%CEXT*(p+VerticalCounter*TLength*G*RhoL);
                    HorizontalCounter=1;
                    VerticalCounter=VerticalCounter+1;
                    Counter=Counter+1;

                elseif (prop(Y,X)==3) %Left non-corner node

                    ConstantMatrix(Counter,Counter)=2*CV+CH; %+CEXT;
                    ConstantMatrix(Counter,Counter+1)=-1*CH;
                    ConstantMatrix(Counter,Counter-NX)=-1*CV;
                    ConstantMatrix(Counter,Counter+NX)=-1*CV;
                    AnswerMatrix(Counter,1)=0;
%CEXT*(p+VerticalCounter*TLength*G*RhoL);
                    HorizontalCounter=HorizontalCounter+1;
                    Counter=Counter+1;

                elseif (prop(Y,X)==32) %Above bubble node

                    ConstantMatrix(Counter,Counter)=2*CH+CV;
                    ConstantMatrix(Counter,Counter-1)=-1*CH;
                    ConstantMatrix(Counter,Counter+1)=-1*CH;
```

```
                ConstantMatrix(Counter,Counter-NX)=-1*CV;
                AnswerMatrix(Counter,1)=Q-RhoL*G*TLength*CV;
                Change1=Counter;
                HorizontalCounter=HorizontalCounter+1;
                Counter=Counter+1;

            elseif (prop(Y,X)==33) %Below bubble nodes

                ConstantMatrix(Counter,Counter)=2*CH+CV;
                ConstantMatrix(Counter,Counter-1)=-1*CH;
                ConstantMatrix(Counter,Counter+1)=-1*CH;
                ConstantMatrix(Counter,Counter+NX)=-1*CV;
                AnswerMatrix(Counter,1)=-Q+CV*TLength*G*RhoL;
                Change2=Counter;
                HorizontalCounter=HorizontalCounter+1;
                Counter=Counter+1;

            elseif (prop(Y,X)==29) %Left bubble edge nodes

                ConstantMatrix(Counter,Counter)=2*CV+CH;
                ConstantMatrix(Counter,Counter-1)=-1*CH;
                ConstantMatrix(Counter,Counter-NX)=-1*CV;
                ConstantMatrix(Counter,Counter+NX)=-1*CV;
                HorizontalCounter=HorizontalCounter+1;
                Counter=Counter+1;

            elseif (prop(Y,X)==31) %Right bubble edge nodes

                ConstantMatrix(Counter,Counter)=2*CV+CH;
                ConstantMatrix(Counter,Counter+1)=-1*CH;
                ConstantMatrix(Counter,Counter-NX)=-1*CV;
                ConstantMatrix(Counter,Counter+NX)=-1*CV;
                HorizontalCounter=HorizontalCounter+1;
                Counter=Counter+1;

            else

                ConstantMatrix(Counter,Counter)=2*CH+2*CV;
                ConstantMatrix(Counter,Counter-1)=-1*CH;
                ConstantMatrix(Counter,Counter+1)=-1*CH;
                ConstantMatrix(Counter,Counter-NX)=-1*CV;
                ConstantMatrix(Counter,Counter+NX)=-1*CV;
                HorizontalCounter=HorizontalCounter+1;
                Counter=Counter+1;

            end
        end
        end
        fff=1;
    end
else
```

```
        % Changes the two values of Q (flow rate of water caused by bubble
        % motion) to the new values with respect to the new guess for bubble
velcity

        AnswerMatrix(Change1,1)=Ububble*pi*TDiameterVS^2/4-RhoL*G*TLength*CV;
        AnswerMatrix(Change2,1)=-
1*Ububble*pi*TDiameterVS^2/4+RhoL*G*TLength*CV;

    end

    % Solve the matrix of simultaneous equations
    % Method: Calculate the answer via Gaussian elimination using the Matlab
"\" function

    Solution=ConstantMatrix\AnswerMatrix;
    % Solution=inv(ConstantMatrix)*AnswerMatrix;

    Counter=1;
    HorizontalCounter=1;
    VerticalCounter=1;

    % Create the pressure field matrix by assigning the values of the
    % solution matrix to their appropriate place

    for Y=1:NY
      for X=1:NX

            PressureField(Y,X)=Solution(Counter,1);
            PressureField2(Y,X)=Solution(Counter,1)/p;
            PressureField3(Y,X)=(Solution(Counter,1)-p)/(RhoL*G)+
TLength*(NY-Y+1);
            PotentialField(Y,X)=(Solution(Counter,1))/(RhoL*G)+ TLength*(Y-
1);
            Counter=Counter+1;

      end
    end

    % Calculate the power input of the bubble; compare this with the power
    % dissipation due to friction ... If they are close to within a given
    % tolerance, terminate the simulation. Otherwise, take a new guess at
    % bubble velocity and repeat previous steps

    %Power input due to bubble motion

    PowerInput=pi*TDiameterVS^2/4*(BuoyancyPressure-
SurfaceTensionPressure)*Ububble; % Net driving force x velocity

    PowerDissipation=0;
```

```
    HorizontalCounter=1;
    VerticalCounter=1;
    stat=0;

    while (stat==0)

        if (prop(VerticalCounter,HorizontalCounter)==24) % Bottom right
corner node

            %PowerDissipation =
PowerDissipation+CEXT*((PotentialField(VerticalCounter,HorizontalCounter)-
TLength*(NY+1))*RhoL*G)^2;
            %PowerDissipation =
PowerDissipation+CEXT*((PotentialField(VerticalCounter,HorizontalCounter)-
TLength*(NY+1))*RhoL*G)^2;
            stat=1;
            if (stat==1)
                continue
            end

        elseif (prop(VerticalCounter,HorizontalCounter)==13) %Top left corner
node

            %PowerDissipation =
PowerDissipation+CEXT*((PotentialField(VerticalCounter,HorizontalCounter)-
TLength*(NY+1))*RhoL*G)^2;
            %PowerDissipation =
PowerDissipation+CEXT*((PotentialField(VerticalCounter,HorizontalCounter)-
TLength*(NY+1))*RhoL*G)^2;
            PowerDissipation =
PowerDissipation+CH*((PotentialField(VerticalCounter,HorizontalCounter)-
PotentialField(VerticalCounter,HorizontalCounter+1))*RhoL*G)^2;
            PowerDissipation =
PowerDissipation+CV*((PotentialField(VerticalCounter,HorizontalCounter)-
PotentialField(VerticalCounter+1,HorizontalCounter))*RhoL*G)^2;
            HorizontalCounter=HorizontalCounter+1;
            if ((HorizontalCounter>NX)||(VerticalCounter>NY))
                continue
            end

        elseif(prop(VerticalCounter,HorizontalCounter)==23) %Bottom left
corner node

            %PowerDissipation =
PowerDissipation+CEXT*((PotentialField(VerticalCounter,HorizontalCounter)-
TLength*(NY+1))*RhoL*G)^2;
            %PowerDissipation =
PowerDissipation+CEXT*((PotentialField(VerticalCounter,HorizontalCounter)-
TLength*(NY+1))*RhoL*G)^2;
```

```
            PowerDissipation =
PowerDissipation+CH*((PotentialField(VerticalCounter,HorizontalCounter)-
PotentialField(VerticalCounter,HorizontalCounter+1))*RhoL*G)^2;
            HorizontalCounter=HorizontalCounter+1;
            if ((HorizontalCounter>NX)||(VerticalCounter>NY))
                continue
            end

        elseif(prop(VerticalCounter,HorizontalCounter)==14) %Top right corner
node

            %PowerDissipation =
PowerDissipation+CEXT*((PotentialField(VerticalCounter,HorizontalCounter)-
TLength*(NY+1))*RhoL*G)^2;
            %PowerDissipation =
PowerDissipation+CEXT*((PotentialField(VerticalCounter,HorizontalCounter)-
TLength*(NY+1))*RhoL*G)^2;
            PowerDissipation =
PowerDissipation+CV*((PotentialField(VerticalCounter,HorizontalCounter)-
PotentialField(VerticalCounter+1,HorizontalCounter))*RhoL*G)^2;
            HorizontalCounter=1;
            VerticalCounter=VerticalCounter+1;
            if ((HorizontalCounter>NX)||(VerticalCounter>NY))
                continue
            end

        elseif(prop(VerticalCounter,HorizontalCounter)==4) %Right edge node

            PowerDissipation =
PowerDissipation+CV*((PotentialField(VerticalCounter,HorizontalCounter)-
PotentialField(VerticalCounter+1,HorizontalCounter))*RhoL*G)^2;
            %PowerDissipation =
PowerDissipation+CEXT*((PotentialField(VerticalCounter,HorizontalCounter)-
TLength*(NY+1))*RhoL*G)^2;
            HorizontalCounter=1;
            VerticalCounter=VerticalCounter+1;
            if ((HorizontalCounter>NX)||(VerticalCounter>NY))
                continue
            end

        elseif(prop(VerticalCounter,HorizontalCounter)==2) %Bottom edge node

            PowerDissipation =
PowerDissipation+CH*((PotentialField(VerticalCounter,HorizontalCounter)-
PotentialField(VerticalCounter,HorizontalCounter+1))*RhoL*G)^2;
            %PowerDissipation =
PowerDissipation+CEXT*((PotentialField(VerticalCounter,HorizontalCounter)-
TLength*(NY+1))*RhoL*G)^2;
            HorizontalCounter=HorizontalCounter+1;
            if ((HorizontalCounter>NX)||(VerticalCounter>NY))
                continue
            end
```

```
        elseif (prop(VerticalCounter,HorizontalCounter)==1) %Top edge node

            PowerDissipation =
PowerDissipation+CV*((PotentialField(VerticalCounter,HorizontalCounter)-
PotentialField(VerticalCounter+1,HorizontalCounter))*RhoL*G)^2;
            PowerDissipation =
PowerDissipation+CH*((PotentialField(VerticalCounter,HorizontalCounter)-
PotentialField(VerticalCounter,HorizontalCounter+1))*RhoL*G)^2;
            %PowerDissipation =
PowerDissipation+CEXT*((PotentialField(VerticalCounter,HorizontalCounter)-
TLength*(NY+1))*RhoL*G)^2;
            HorizontalCounter=HorizontalCounter+1;
            if ((HorizontalCounter>NX)||(VerticalCounter>NY))
                continue
            end

        elseif (prop(VerticalCounter,HorizontalCounter)==3) %Left edge node

            PowerDissipation =
PowerDissipation+CV*((PotentialField(VerticalCounter,HorizontalCounter)-
PotentialField(VerticalCounter+1,HorizontalCounter))*RhoL*G)^2;
            PowerDissipation =
PowerDissipation+CH*((PotentialField(VerticalCounter,HorizontalCounter)-
PotentialField(VerticalCounter,HorizontalCounter+1))*RhoL*G)^2;
            %PowerDissipation =
PowerDissipation+CEXT*((PotentialField(VerticalCounter,HorizontalCounter)-
TLength*(NY+1))*RhoL*G)^2;
            HorizontalCounter=HorizontalCounter+1;
            if ((HorizontalCounter>NX)||(VerticalCounter>NY))
                continue
            end

        elseif (prop(VerticalCounter,HorizontalCounter)==29) %Left bubble
edge node

            PowerDissipation =
PowerDissipation+CV*((PotentialField(VerticalCounter,HorizontalCounter)-
PotentialField(VerticalCounter+1,HorizontalCounter))*RhoL*G)^2;
            HorizontalCounter=HorizontalCounter+1;
            if ((HorizontalCounter>NX)||(VerticalCounter>NY))
                continue
            end

        elseif (prop(VerticalCounter,HorizontalCounter)==32) %Above bubble
node

            PowerDissipation =
PowerDissipation+CH*((PotentialField(VerticalCounter,HorizontalCounter)-
PotentialField(VerticalCounter,HorizontalCounter+1))*RhoL*G)^2;
            HorizontalCounter=HorizontalCounter+1;
            if ((HorizontalCounter>NX)||(VerticalCounter>NY))
```

```
                continue
            end

        elseif (prop(VerticalCounter,HorizontalCounter)==35) %Top bubble node

            %PowerDissipation = PowerDissipation-
2*(Ububble*pi*TDiameterVS^2/4)^2/CV;
            HorizontalCounter=HorizontalCounter+1;
            if ((HorizontalCounter>NX)||(VerticalCounter>NY))
                continue
            end

        elseif
(prop(VerticalCounter,HorizontalCounter)==30||prop(VerticalCounter,Horizontal
Counter)==34) % Bubble node

            HorizontalCounter=HorizontalCounter+1;

        else

            PowerDissipation =
PowerDissipation+CV*((PotentialField(VerticalCounter,HorizontalCounter)-
PotentialField(VerticalCounter+1,HorizontalCounter))*RhoL*G)^2;
            PowerDissipation =
PowerDissipation+CH*((PotentialField(VerticalCounter,HorizontalCounter)-
PotentialField(VerticalCounter,HorizontalCounter+1))*RhoL*G)^2;
            HorizontalCounter=HorizontalCounter+1;
            if ((HorizontalCounter>NX)||(VerticalCounter>NY))
                continue
            end

        end

    end

    PowerDissipation=PowerDissipation*1.0;

    % Compare power input and power dissipation

    TrendMatrix(TrendCounter,1)=Ububble;
    TrendMatrix(TrendCounter,2)=abs(PowerInput-PowerDissipation);
    TrendCounter=TrendCounter+1;

    if(Tolerance>=abs((PowerInput-
PowerDissipation)/PowerInput)||StepCounter>100)

        CheckVar=1; % Terminate the simulation

    else
```

```
    % Output section: used to track simulation progress

    fprintf('StepCounter=  %d, ',StepCounter)
    fprintf('Bubble velocity =  %0.4f, ',Ububble)
    fprintf('Pin= %0.4f, ',(PowerInput))
    fprintf('Pdis=  %0.4f, ',(PowerDissipation))
    fprintf('Pin-Pdis= %0.4f \n',((PowerInput-PowerDissipation)/PowerInput))
    %fprintf('\n')

       if (LastDiff*(PowerInput-PowerDissipation)<0)
            LowerCheck=1;
            Upre=LastUb;
            UU=Ububble;
            Ububble=(Ububble+LastUb)/2;
            LastUb=UU;
       else
        if (LowerCheck==1)
            LastUb=Ububble;
            Ububble=(Ububble+Upre)/2;
            if(Ububble==LastUb)
               CheckVar=1; % Terminate the simulation
            end
            ConvergenceCounter=ConvergenceCounter+1;
        else
            LastUb=Ububble;
            Ububble=Fraction*LastUb;
        end
      end
      LastDiff=(PowerInput-PowerDissipation);
    end

    StepCounter=StepCounter+1;

end
 % Output section: used to track simulation progress

    fprintf('StepCounter=  %d, ',StepCounter)
    fprintf('Bubble velocity = %0.4f, ',Ububble)
    fprintf('Pin=  %0.4f, ',(PowerInput))
    fprintf('Pdis= %0.4f, ',(PowerDissipation))
    fprintf('Pin-Pdis= %0.4f \n',((PowerInput-PowerDissipation)/PowerInput))
    %fprintf('\n')
nn=0;
mm=0;
ff=0;
for n=1:2*NY-1
    if (mod(n,2)~=0) nn=nn+1; end;
    mm=0;
    for m=1:2*NX-1
        if (mod(m,2)~=0) mm=mm+1; end
        yc(n,m)=(n-1)*0.5;
        xc(n,m)=(m-1)*0.5;
```

```
        if (mod(n,2)==0)
            if (mod(m,2)~=0)
                pp=-PotentialField(nn,mm)+PotentialField(nn+1,mm);
                if (abs(pp)>0.0001)
                    if
((abs(pp)<0.6)&&(prop(nn,mm)~=30)&&(prop(nn,mm)~=35)&&(prop(nn,mm)~=34)&&(pro
p(nn,mm)~=33))
                        vctry(n,m)=pp;
                    end
                end
            end
        else
            if (mod(m,2)==0)
                pp=-PotentialField(nn,mm)+PotentialField(nn,mm+1);
                if (abs(pp)>0.0001)
                    if
((abs(pp)<0.6)&&(prop(nn,mm)~=30)&&(prop(nn,mm)~=35)&&(prop(nn,mm)~=34)&&(pro
p(nn,mm)~=33))
                        vctrx(n,m)=pp;
                    end
                end
            end
        end
        if ((prop(nn,mm)==30)||(prop(nn,mm)==35)||(prop(nn,mm)==34))
            if (ff==0)
              if (mod(n,2)~=0)
                  rectangle('position',[xc(n,m)-0.5,yc(n,m)-
0.5,1,1],'curvature',[.8,.8])
              end
              ff=1;
            else
                ff=0;
            end
        end
    end
end
hold on
quiver(xc,yc,vctrx,vctry,2.5) %xc,yc,
axis equal
hold off
```